



MINISTÉRIO DA
CIÊNCIA, TECNOLOGIA
E INOVAÇÕES



sid.inpe.br/mtc-m21c/2020/10.27.18.43-TDI

ATOMIZATION OF LIQUID AND GELLED SIMULANT PROPELLANTS BY IMPINGING JETS

Gabriel Silva Dias

Master's Dissertation of
the Graduate Course in
Engineering and Space
Technologies/Combustion and
Propulsion, guided by Dr.
Fernando de Souza Costa,
approved in October 26, 2020.

URL of the original document:

<<http://urlib.net/8JMKD3MGP3W34R/43FSSKH>>

INPE
São José dos Campos
2020

PUBLISHED BY:

Instituto Nacional de Pesquisas Espaciais - INPE
Gabinete do Diretor (GBDIR)
Serviço de Informação e Documentação (SESID)
CEP 12.227-010
São José dos Campos - SP - Brasil
Tel.:(012) 3208-6923/7348
E-mail: pubtc@inpe.br

**BOARD OF PUBLISHING AND PRESERVATION OF INPE
INTELLECTUAL PRODUCTION - CEPPII (PORTARIA Nº
176/2018/SEI-INPE):****Chairperson:**

Dra. Marley Cavalcante de Lima Moscati - Centro de Previsão de Tempo e Estudos
Climáticos (CGCPT)

Members:

Dra. Carina Barros Mello - Coordenação de Laboratórios Associados (COCTE)
Dr. Alisson Dal Lago - Coordenação-Geral de Ciências Espaciais e Atmosféricas
(CGCEA)
Dr. Evandro Albiach Branco - Centro de Ciência do Sistema Terrestre (COCST)
Dr. Evandro Marconi Rocco - Coordenação-Geral de Engenharia e Tecnologia
Espacial (CGETE)
Dr. Hermann Johann Heinrich Kux - Coordenação-Geral de Observação da Terra
(CGOBT)
Dra. Ieda Del Arco Sanches - Conselho de Pós-Graduação - (CPG)
Sílvia Castro Marcelino - Serviço de Informação e Documentação (SESID)

DIGITAL LIBRARY:

Dr. Gerald Jean Francis Banon
Clayton Martins Pereira - Serviço de Informação e Documentação (SESID)

DOCUMENT REVIEW:

Simone Angélica Del Ducca Barbedo - Serviço de Informação e Documentação
(SESID)
André Luis Dias Fernandes - Serviço de Informação e Documentação (SESID)

ELECTRONIC EDITING:

Ivone Martins - Serviço de Informação e Documentação (SESID)
Cauê Silva Fróes - Serviço de Informação e Documentação (SESID)



MINISTÉRIO DA
CIÊNCIA, TECNOLOGIA
E INOVAÇÕES



sid.inpe.br/mtc-m21c/2020/10.27.18.43-TDI

ATOMIZATION OF LIQUID AND GELLED SIMULANT PROPELLANTS BY IMPINGING JETS

Gabriel Silva Dias

Master's Dissertation of
the Graduate Course in
Engineering and Space
Technologies/Combustion and
Propulsion, guided by Dr.
Fernando de Souza Costa,
approved in October 26, 2020.

URL of the original document:

<<http://urlib.net/8JMKD3MGP3W34R/43FSSKH>>

INPE
São José dos Campos
2020

Cataloging in Publication Data

Dias, Gabriel Silva.

D543a Atomization of liquid and gelled simulant propellants by impinging jets / Gabriel Silva Dias. – São José dos Campos : INPE, 2020.

xviii + 128 p. ; (sid.inpe.br/mtc-m21c/2020/10.27.18.43-TDI)

Dissertation (Master in Engineering and Space Technologies/Combustion and Propulsion) – Instituto Nacional de Pesquisas Espaciais, São José dos Campos, 2020.

Guiding : Dr. Fernando de Souza Costa.

1. Atomization. 2. Jet impingement. 3. Liquid propellants. 4. Gelled propellants. 5. Spray. I.Title.

CDU 629.78:621.56



Esta obra foi licenciada sob uma Licença [Creative Commons Atribuição-NãoComercial 3.0 Não Adaptada](https://creativecommons.org/licenses/by-nc/3.0/).

This work is licensed under a [Creative Commons Attribution-NonCommercial 3.0 Unported License](https://creativecommons.org/licenses/by-nc/3.0/).



INSTITUTO NACIONAL DE PESQUISAS ESPACIAIS

[Pós Graduação]

[Engenharia e Tecnologia Espaciais - Combustão e Propulsão]

DEFESA FINAL DE DISSERTAÇÃO DE GABRIEL SILVA DIAS

No dia 26 de outubro de 2020, as 14h, por videoconferência, o aluno mencionado acima defendeu seu trabalho final (apresentação oral seguida de arguição) perante uma Banca Examinadora, cujos membros estão listados abaixo. O aluno foi APROVADO pela Banca Examinadora, por unanimidade, em cumprimento ao requisito exigido para obtenção do Título de Mestre em Engenharia e Tecnologia Espaciais/Combustão e Propulsão. O trabalho precisa da incorporação das correções sugeridas pela Banca Examinadora e revisão final pelo orientador.

Título: ATOMIZATION OF LIQUID AND GELLED SIMULANT PROPELLANTS BY IMPINGING JETS

Eu, Dr. Fernando de Souza Costa, como Presidente da Banca Examinadora, assino esta ATA em nome de todos os membros.

Membros da Banca

- Dr. Fernando de Souza Costa - Orientador/Presidente e Docente do PCP/ETE/INPE
- Dra. Adriana Maria da Silva - Colaboradora do PCP/ETE/INPE
- Dr. Márcio Teixeira de Mendonça - Colaborador do PCP/ETE/INPE
- Dr. João Andrade de Carvalho Júnior- Membro Externo do INPE e ao Corpo Docente do ETE



Documento assinado eletronicamente por **Fernando de Souza Costa, Pesquisador**, em 31/10/2020, às 12:26 (horário oficial de Brasília), com fundamento no art. 6º, § 1º, do [Decreto nº 8.539, de 8 de outubro de 2015](#).



A autenticidade deste documento pode ser conferida no site <http://sei.mctic.gov.br/verifica.html>, informando o código verificador **6033929** e o código CRC **1BD15CBD**.

ACKNOWLEDGEMENTS

I would like to thank CAPES for the scholarship granted, Fernando for advising, Andrade, Chico, Danilo and Pedro for helping with experiments in INPE/LCP and UNESP/FEG Laboratories. I also thank Jorge and Matheus for productive discussions and Renata for all the support and incentive.

ABSTRACT

This work presents an experimental study of the atomization process by jet impingement of liquid and gelled simulant propellants. Like and unlike jets of liquid water, gelled water, liquid hydrous ethanol and gelled hydrous ethanol were tested for different injection pressures, collision distances and collision angles. Experimental data were given in terms of jet momenta and conventional or generalized non-dimensional numbers, Re , Re_{gen} , We and We_{gen} , for liquids and gels. A power law model was adopted to represent the gelled fluids and to define the generalized parameters. Shadow images of the collision sheets were obtained with help of a high speed camera and droplet velocities were calculated by an open PIV software. A patternator was used to estimate mass flux distributions of the sprays formed. Droplet size distributions and representative droplet diameters (SMD and Dv_{10}) were determined by a laser diffraction system. Collision sheet geometries were compared to theoretical model predictions, showing good agreement for liquids. Experimental spray mass flux distributions presented a good agreement with literature data. Images from a high speed camera showed that gel sprays can form complex structures with presence of holes, rails and/or fishbone geometries. Disturbances and impact waves in the collision sheet produce ligaments from which droplets are detached. Transient behavior was observed in some cases with presence of different geometrical configurations. Long ligaments require larger distances to fragment into drops and even with high injection pressures some ligaments do not break up. Such delay or no ligament disintegration of the gel film probably occurs as consequence of the absence or low intensity of impact waves introduced by the colliding jets. The atomization of gelled fluids was improved by using a colliding liquid jet, which acts as an atomization assistant which generates disturbances to the gel/liquid film. Unlike jet impingement of gels, even with same jet momentum, creates a shear layer in the collision sheet due to the different jet velocities, improving the atomization process.

Keywords: atomization. jet impingement. liquid propellants. gelled propellants. spray.

ATOMIZAÇÃO POR JATOS COLIDENTES DE SIMULANTES DE PROPELENTES LÍQUIDOS E GELIFICADOS

RESUMO

Este trabalho apresenta um estudo experimental do processo de atomização por jatos colidentes de simulantes de propelentes líquidos e gelificados. Jatos de fluidos iguais ou diferentes de água líquida, água gelificada, etanol líquido e etanol gelificado foram testados com diferentes pressões de injeção, distâncias de colisão e ângulos de colisão. Os dados experimentais foram apresentados em termos da quantidade de movimento dos jatos e de números adimensionais convencionais ou generalizados, Re , Re_{gen} , We and We_{gen} , para líquidos e géis. Um modelo de lei de potência foi adotado para representar os fluidos gelificados e definir os parâmetros generalizados. Imagens shadowgraph das folhas de colisão foram obtidas com a ajuda de uma câmera de alta velocidade e um software PIV aberto foi adotado para cálculo das velocidades das gotas. Um paternador foi usado para estimar as distribuições de fluxo de massa dos sprays formados. Distribuições de tamanho de gota e diâmetros de gota representativos (SMD e Dv_{10}) foram determinados por um sistema de difração a laser. As geometrias das folhas de colisão foram comparadas às previsões de um modelo teórico, mostrando boa concordância para líquidos. As distribuições de fluxo de massa dos sprays medidas experimentalmente apresentaram boa concordância com dados da literatura. As imagens shadow obtidas pela câmera de alta velocidade mostraram que os sprays de gel podem formar estruturas complexas com presença de furos, trilhos e/ou geometrias em espinha de peixe. Perturbações e ondas de impacto na folha de colisão produzem ligamentos dos quais as gotas são destacadas. Um comportamento transiente foi observado em alguns casos com presença de diferentes configurações geométricas. Os ligamentos longos requerem distâncias maiores para se fragmentarem em gotas e, mesmo com altas pressões de injeção, alguns ligamentos não se rompem. Esse retardo ou não desintegração ligamentar do filme de gel provavelmente ocorre em decorrência da ausência ou baixa intensidade das ondas de impacto introduzidas pelos jatos em colisão. A atomização dos fluidos gelificados foi melhorada com o uso de um jato colidente de líquido, que atua como um assistente de atomização que gera distúrbios no gel/filme líquido. No caso de colisão de jatos de géis diferentes, mesmo com uma mesma quantidade de movimento dos jatos, forma-se uma camada de cisalhamento na folha de colisão devido às diferentes velocidades dos jatos, facilitando o processo de atomização.

Keywords: atomização. colisão de jato. propelentes líquidos. propelentes gelificados. spray.

LIST OF FIGURES

	<u>Page</u>
1.1 Simplified scheme of a propulsive system using impinging jets.	1
2.1 Scheme of unidirectional laminar shearing flow.	5
2.2 Newtonian and categories of non-Newtonian Fluids.	7
2.3 Shear thinning material under flow.	9
2.4 Carbopol 0.30 wt% (water) obtained with a cryogenic field emission scanning electron microscopy	10
2.5 Liquid drop on a solid surface	11
2.6 Thixotropy behavior	14
2.7 Two jet impinging scheme	15
2.8 Apollo LMAE injection plate	17
2.9 Interest on subject based on Scopus	17
2.10 Scheme of Like and Unlike impingement	18
2.11 Light scattering patterns of different particle sizes	21
2.12 Diagram of parallel-light direct shadowgraph observation of a schlieren object	23
2.13 PIV system in a wind tunnel	24
2.14 PIVlab workflow	25
2.15 Important variables in a liquid sheet	28
2.16 Dilational and sinuous wave breakup	32
2.17 Schematic of secondary droplet breakup modes	34
2.18 Binary collision scheme	36
3.1 Gelled water and gelled ethanol	39
3.2 Rheology - Power law fluid	40
3.3 Rheology - Shear stress	40
3.4 Constant shear rate analysis at 25°C	41
3.5 FTIR-ATR spectrometer	44
3.6 FTIR spectra of <i>Carbopol</i> [®] and dried gelled ethanol.	45
3.7 FTIR spectra of <i>Carbopol</i> [®] and dried gelled water.	45
3.8 FTIR spectra of triethanolamine and dried gelled water.	46
3.9 Contact angle goniometer	47
3.10 Surface tension and contact angles using two test fluids.	49
3.11 Straight lines obtained using the OWRK model.	50
3.12 Workbenches	51
3.13 Inlet-chamfered injectors used for tests.	52

3.14	Spray patternator.	53
3.15	Velocity and mass flow rate versus pressure of working fluids	54
3.16	Shadowgraph apparatus set-up with overhead projector lenses, LED flashlight and a high speed camera.	55
3.17	Spraytec workbench	56
3.18	Refractive index qualitative test	57
3.19	Horizontal distances between scattered laser points	57
3.20	PIVlab ensemble correlation setup	59
3.21	Velocity comparison - measured by hand vs PIVlab.	60
4.1	Free jets in ambient air for increasing injection pressures.	66
4.2	Theoretical and experimental collision sheets.	67
4.3	Aspect ratio and breakup length of collision sheets versus Re.	68
4.4	Sheet shapes increasing Reynolds	69
4.5	Liquid water x liquid water, like impingement – experimental and theo- retical representative diameters.	70
4.6	Ethanol x Ethanol, like impingement - SMD	71
4.7	Ethanol x Ethanol, like impingement - D_{10}	72
4.8	Liquid water and liquid ethanol droplet size distribution by volume and number frequency, $2\theta = 75^\circ$ and Injection pressure = 1 bar	73
4.9	Volume frequency and cumulative volume data for liquid water.	74
4.10	Droplet size volume distribution with increasing jet velocity - Ethanol	77
4.11	Liquid water x liquid hydrous ethanol unlike jets impingement and liquid ethanol/liquid water 50% w/w like jets impingement – SMD	78
4.12	Droplet size distributions of unlike colliding jets of liquid hydrous ethanol x liquid water and like colliding jets of liquid hydrous ethanol/liquid water mixtures 50% w/w, for a collision angle of $2\theta=90^\circ$	79
4.13	Liquid hydrous ethanol and liquid water - like and unlike impingement, $2\theta = 75^\circ$	80
4.14	Mass flux distribution estimate for like jet impingement of liquid water. $\dot{m}_{tot}=17.58$ g/s, $F=154.31$ N, $u_j = 17.14$ m/s	82
4.15	Mass flux distribution estimate for like jet impingement of liquid hydrous ethanol. $\dot{m}_{tot}=13.92$ g/s, $F=119.36$ N, $u_j = 17.55$ m/s	82
4.16	Mass flux distribution for unlike impingement of liquid hydrous ethanol and liquid water jets.	84
4.17	Mixing along the vertical centerline of Figure 4.16 for unlike impingement of liquid hydrous ethanol and liquid water jets.	84
4.18	Mixing - Ethanol	85
4.19	Mixing - Water	85

4.20	Mixing regimes	86
4.21	Gelled water and gelled ethanol - like and unlike impingement, $2\theta = 75^\circ$.	88
4.22	Gelled Ethanol x Gelled Ethanol - Like impingement - $2\theta = 75^\circ$	89
4.23	Impact wave starting from impingement point and propagation for like impingement of gelled hydrous ethanol jets, with jet momentum 63 N and $2\theta = 75^\circ$	89
4.24	angle=180	92
4.25	SMD and Dv_{10} – <i>Gelledethanollikeimpingement</i>	93
4.26	Drop size distribution of a spray formed by like impingement of jets of gelled ethanol, $P_{inj} = 7$ bar, $2\theta = 75^\circ$	94
4.27	Transient disintegration of the collision sheet for unlike impingement of gelled water/gelled ethanol jets with collision angle $2\theta = 75^\circ$	95
4.28	Gelled hydrous ethanol and gelled water unlike impinging with liquid water and liquid hydrous ethanol, $2\theta = 75^\circ$	96
4.29	SMD for Gelled ethanol impinging with liquid water and liquid ethanol, unlike impingement	99
4.30	SMD for gelled water impinging with liquid water and liquid hydrous ethanol - unlike impingement.	100
4.31	Droplet size distribution by number volume for unlike impingement of gelled water with liquid water and liquid hydrous ethanol, $2\theta = 75^\circ$. . .	101
4.32	Sheet breakup visualization - Gelled Ethanol x Liquid Water Unlike Im- pingement	102
4.33	Evolution of holes on sheet - Gelled Ethanol x Water Unlike Impingement - $2\theta=90^\circ$, $\dot{m}v=11$	102
4.34	SMD for unlike impingement of Gelled Hydrous Ethanol x Liquid Water versus Re_{water} and jet momentum.	104
4.35	Weber number - newtonian and non-Newtonian (generalized) comparison	106
4.36	Linear stability model predictions with We and We_{gen}	107
4.37	Particle velocities of ligaments and droplets for Unlike Impingement of Gelled Ethanol x Liquid Water, Jet momentum 11 N, $2\theta = 90^\circ$	109
4.38	Particle velocities of ligaments and droplets for Unlike Impingement of Gelled Hydrous Ethanol impinging with Liquid Water and Liquid Hy- drous Ethanol.	110
4.39	Particle size distribution by number frequency, Gelled ethanol impinging with liquid water and ethanol, unlike impingement	110
4.40	Ligament velocities varying jet velocity, for $2\theta = 80^\circ$	111
4.41	Particle velocities of ligaments and droplets for unlike impingement of gelled hydrous ethanol with liquid water and liquid hydrous ethanol. . .	112

4.42	Droplet velocities for Unlike Impingement of Gelled Ethanol x Liquid Water, Jet momentum 11 N, $2\theta = 75^\circ$ - Scatter and histogram of particles in Z direction (side view of Figure 4.32)	112
4.43	.stl file for numerical simulation of like impingement - $2\theta = 90^\circ$	114
4.44	Preliminary numerical results for Like impingement of liquid ethanol, $\alpha=0.5$, write interval=0.4 ms - $2\theta = 90^\circ$	115

LIST OF TABLES

	<u>Page</u>
1.1 Characteristics of propellants used in chemical propulsion.	3
2.1 Rocket engines using injector plates with impinging jets	16
3.1 Water properties at 20°C.	37
3.2 Liquid hydrous ethanol properties.	38
3.3 Gelled ethanol according to manufacturer FISPQ.	42
3.4 Gelled water composition according to the manufacturer FISPQ.	42
3.5 Drying 1 - Residual masses of gelled ethanol and gelled water.	43
3.6 Drying 2 - Residual masses of gelled ethanol and gelled water.	47
3.7 Some test fluids and their polar/dispersive components	48
3.8 Result by manufacture software	49
3.9 Result by OWRK method	50
3.10 Refractive index, literature and measured	58
3.11 Working fluids properties - Overview	61
3.12 Adopted uncertainty	62
3.13 Calculated experimental uncertainty.	64
4.1 Coalescence analysis for liquid water and liquid hydrous ethanol.	75
4.2 Secondary atomization analysis for liquid water and liquid hydrous ethanol.	76
4.3 Jet parameters for collision of jets shown in Figs. 4.13, 4.21, 4.22, 4.24, 4.27, 4.28, 4.32 and 4.33.	90
4.4 Maximum and minimum values of SMD for unlike impingement of gelled hydrous ethanol with liquid water and liquid hydrous ethanol, and their respective jet momentum values.	98
4.5 Maximum and minimum values of SMD for unlike impingement of gelled water with liquid water and liquid hydrous ethanol, and their respective jet momentum values.	98
4.6 Jet velocities.	108

CONTENTS

	<u>Page</u>
1 INTRODUCTION	1
1.1 Main objective	3
1.2 Specific objectives	4
2 LITERATURE REVIEW	5
2.1 Newtonian and non-Newtonian fluids	5
2.2 Important aspects of gels	7
2.2.1 Shear thinning behavior	8
2.2.2 Surface free energy and surface tension	10
2.2.3 Thixotropy	13
2.3 Atomization process by the impingement of jets	14
2.3.1 Like and Unlike impingement	17
2.3.2 Gelled propellants and use of impinging jets	18
2.3.3 Dimensionless numbers in fluid mechanics and usage in atomization processes	19
2.3.4 Droplet size	20
2.3.4.1 Droplet size measurement by laser diffraction	20
2.4 Shadowgraph imaging technique	22
2.5 Particle Image Velocimetry	23
2.5.1 Opensource PIV, low price alternative technique	24
2.6 Infrared (IF) spectroscopy	25
2.7 Theoretical models for impingement of jets	26
2.7.1 Liquid sheet shape	26
2.7.2 Breakup - Droplet mean diameter	28
2.7.2.1 Breakup - Droplet mean diameter with linear instability model	30
2.7.2.2 Breakup - Droplet mean diameter with impact wave model	33
2.8 Secondary atomization	33
2.9 Droplet collision and coalescence	34
3 METHODOLOGY	37
3.1 Working fluids	37
3.1.1 Newtonian working fluids	37
3.1.2 Non-Newtonian working fluids	38

3.1.2.1	Drying 1	43
3.1.2.1.1	- Fourier-Transform Infrared Spectroscopy (FTIR) spectra of dry samples	43
3.1.2.2	Drying 2	46
3.1.2.3	Surface tension measurement by contact angle	47
3.2	Workbench and injectors	50
3.2.1	Shadowgraph apparatus	54
3.2.2	Spraytec laser diffraction system - particle size measurement	55
3.2.2.1	Refractive index - qualitative measurement	56
3.3	PIVlab set-up and results verification	58
3.4	Working fluids properties - overview	61
3.5	Experimental uncertainty	61
4	RESULTS	65
4.1	Pre-impingement jet conditions	65
4.2	Collision sheet shapes	66
4.3	Atomization of liquid water and liquid hydrous ethanol, like and unlike impingement	69
4.3.1	Liquid water - like impingement	69
4.3.2	Liquid hydrous ethanol - like impingement	71
4.3.3	Droplet size distributions	72
4.3.3.1	Coalescence and secondary breakup - brief analysis	75
4.3.4	Liquid water x liquid hydrous ethanol - unlike impingement	77
4.3.4.1	Spray pattern and mixing	81
4.4	Atomization of gels with like and unlike impingement of jets	86
4.5	Atomization of Gels x Liquids, unlike impingement	95
4.5.1	Weber or generalized Weber number	105
4.6	Droplet velocity in particular cases	107
4.7	Impinging jets simulation, preliminary results	113
5	CONCLUSIONS	117
5.1	Future work suggestions	118
	REFERENCES	119

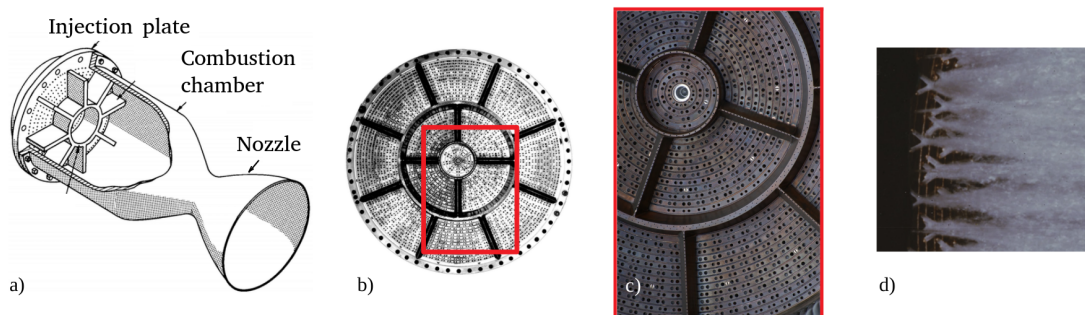
1 INTRODUCTION

Rocket propulsion systems can be classified in several ways, for example according to energy source (chemical, electric, nuclear or solar) or by their basic function (booster, upper stage, attitude control, among others), or by the type of vehicle they propel (missile, spacecraft, etc.) or by its size, propellant type, construction type and/or the number of propulsion units of rockets used in a particular vehicle. Another useful way to classify rockets is by the method of producing thrust. Thermodynamic expansion of a gas through a supersonic nozzle is the concept most commonly used in rocket propulsion, where the enthalpies of the propellants are converted into kinetic exhaust energy, and thrust is produced by pressure forces on the surfaces exposed to the exhaust gases (SUTTON; BIBLARZ, 2017).

The source of energy in rocket propulsion is almost always the chemical energy released by combustion of a fuel with an oxidizer. For a class of small thrusters, chemical energy is released by the decomposition of a single propellant, known as a monopropellant, most often hydrazine (MEYER, 1999).

A simplified scheme of a chemical liquid bipropellant is illustrated in Figure 1.1a. The fuel and oxidant, after passing through pressurization systems and control valves, reach the injector plate (Figure 1.1b, c) where they are atomized, and then are vaporized, mixed (Figure 1.1d) and ignited in the combustion chamber. The flue gas resulting from propellant burning is accelerated through the nozzle containing a convergent section, where the flow is subsonic, and a divergent section where the flow is supersonic. At the nozzle throat (minimum nozzle section) the gas velocity is equal to its local sonic velocity (MEYER, 1999).

Figure 1.1 - Simplified scheme of a propulsive system using impinging jets.



SOURCE: Adapted from Bennewitz e Frederick (2013)

Figure 1.1d shows a water test of the F1 rocket engine injector plate used on the American Saturn V launch vehicle. It is possible to see the impingement of jets in the turbulent flow regime.

The development of propulsive systems is affected by different and partially contradictory demands such as more complex mission requirements, increased reliability, environmental and safety aspects and also cost savings (CIEZKI et al., 2015).

Recent research has been done to develop propellants that present low-toxicity and are environmental friendly, called clean or green propellants, to reduce air pollution from rocket launching and the risks of storage and handling. Propulsive systems using such propellants are generally easier and safer to use than traditional ones, and are likely to reduce the costs associated with propellant transportation and storage (AGGARWAL et al., 2015; CIEZKI; NE, 2017).

Gelled propellants combine the main advantages of liquid and solid propulsion systems. Rocket engines that use gelled propellants can be throttled and reignited, similar to engines with liquid propellants. On the other hand, gelled propellants tend not to leak through small tank slits, move less inside reservoirs and have reduced vapor pressure compared to their base fluid (CIEZKI et al., 2017).

Gels are non-Newtonian fluids, i.e. they are semi-liquid materials that have a complex micro-structure and can be described by constitutive models where the stress tensor is a nonlinear function of the strain ratio tensor (FISCHER,).

Although atomization of Newtonian fluids, such as water and common liquid fuels, is well understood and relatively mature in technology, the physics of atomization of non-Newtonian and thixotropic fluids is poorly understood at this time, and the literature on this subject is still in its early stages (BERTOLA, 2017).

Thixotropy is the phenomenon of decreased apparent viscosity with shear time, under a constant shear rate applied to a previously resting sample, and the subsequent recovery of viscosity when flow is suspended. The definition refers to a time-dependent reversible change in viscosity-induced flow (BRETAS; D'ÁVILA, 2005).

Table 1.1 provides a comparison of propellants used in rocket propulsion systems.

Injectors are components responsible for the atomization of liquid or gelled propellants into the rocket combustion chamber. Efficient atomization significantly increases propellant surface area, ensuring high rates of evaporation, mixing and

burning.

Table 1.1 - Characteristics of propellants used in chemical propulsion.

Feature	Solid	Liquid	Hybrid	Slurry	Gel
Controllable thrust	-	✓	✓	✓	✓
Engine shutdown	-	✓	✓	✓	✓
Reignition	+/-	✓	✓	✓	✓
Simple handling/storage	✓	-	-	-	✓
Increase energy by particle add	✓	-	✓	✓	✓
Insensitive to accidental ignition	✓	-	✓	✓	✓
Insensitive to leaks	✓	-	✓	-	✓
Impact insensitive/friction/electric discharge	-	✓	✓	✓	✓
Insensitive to cracking	-	✓	-	✓	✓
Insensitive to sedimentation of additives	✓	-	-	-	✓
Insensitive to boiling	✓	-	✓	-	✓
Insensitive to propellant movement	✓	-	✓	-	✓

SOURCE: Adapted from Ciezki et al. (2014).

Small drops are required to achieve rapid evaporation, mixing and ignition and to establish a flame front adjacent to the injection head. Large droplets take longer to burn and therefore define the length of the combustion chamber (KHAVKIN, 2004).

Impinging jet systems are used to produce mixing and atomization for efficient propellant burning. After the impingement jet impingement, a sheet is formed. Waves form on the leaf's surface and grow until the leaf is fragmented into ligaments, which eventually break into drops (Figure 2.7) (FAKHRI et al., 2010).

In recent decades, efforts have been made to make the use of gelled propellants feasible, due to the advantages presented in Table 1.1. An example is the German Project for Gelled Propulsive Technology (GGPT) started in 2001, composed of researchers from the German Aerospace Center (DLR) and other German institutions, which in 2009 launched a monopropellant missile (NAUMANN et al., 2011).

1.1 Main objective

The objective of this work is to investigate experimentally the atomization process of Newtonian and non-Newtonian fluids by impinging jets.

1.2 Specific objectives

- Perform tests with water, hydrous ethanol, gelled hydrous ethanol and gelled water to simulate atomization of propellants;
- Compare the atomization processes of the different test fluids using a high speed camera, shadowgraph and laser diffraction;
- Compare collision geometries and atomization characteristics by impinging jets in like and unlike configurations.

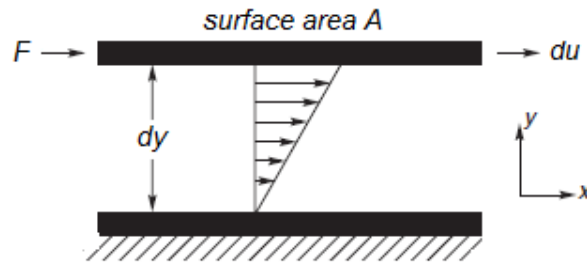
2 LITERATURE REVIEW

2.1 Newtonian and non-Newtonian fluids

Newtonian fluids present a linear relation between shear stress and shear rate, and with zero shear rate at zero shear stress. The proportionality constant is the coefficient of viscosity μ which can vary with temperature and pressure (CARREAU, 1972). As examples, water, alcohol and air can be assumed as Newtonian fluids.

Consider a layer of fluid between two parallel planes separated by a distance dy , as shown in Figure 2.1. In steady conditions, the application of a force F will be balanced by an equal and opposite frictional force inside the liquid.

Figure 2.1 - Scheme of unidirectional laminar shearing flow.



SOURCE: Adapted from Chhabra e Richardson (2008).

Assuming laminar flow of an incompressible fluid between the parallel planes, the shear rate $\dot{\gamma}$ may be expressed as the velocity gradient in the direction perpendicular to the shear force direction, i.e.,

$$\frac{F}{A} = \tau = \mu \left(-\frac{du}{dy} \right) = \mu \dot{\gamma} \quad (2.1)$$

where τ is the shear stress.

Non-Newtonian fluids differ in many ways from Newtonian fluids. In a non-Newtonian fluid, the relationship between the shear stress and the shear rate is nonlinear and sometimes can also be time-dependent. Therefore a constant coefficient of viscosity cannot be defined (NGUYEN; NGUYEN, 2012).

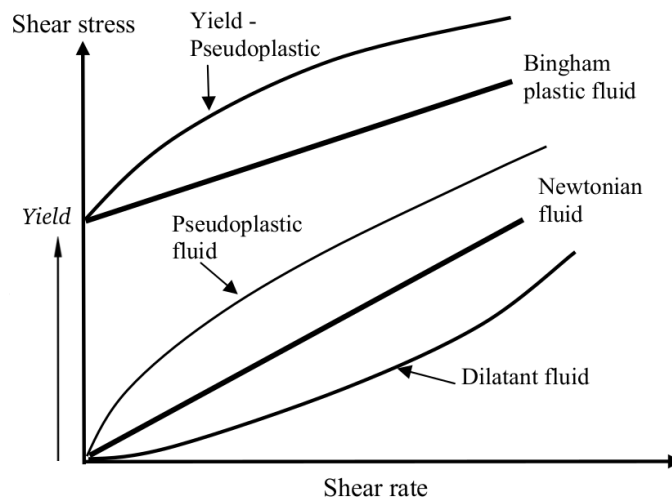
According to Nguyen (2012), non-Newtonian fluids can be divided in:

- Fluids for which their shear rate at any point can be determined by the shear stress only, known as time independent, purely viscous, inelastic or generalized Newtonian fluids;
- Complex fluids, relation between shear stress and shear rate depends, in addition, upon the duration of shearing and their kinematic history, known as time-dependent fluids;
- Materials that have characteristics of both ideal fluids and elastic solids, showing partial elastic recovery after deformation, categorized as viscoplastic fluids.

This work is focused on time-independent fluids, which in turn can be divided into (Figure 2.2):

- Shear thinning or pseudoplastic fluids: characterized by an apparent viscosity which decreases with increasing shear rate. Printing inks, ketchup and blood are examples;
- Viscoplastic fluids: characterized by the existence of a yield stress which must be exceeded before the fluid deforms or flows. Mutually, such a material will deform elastically (or deform like a rigid body) when the externally applied stress is smaller than the yield stress. Bingham plastic fluids fit that classification, examples are mayonnaise and toothpaste. Even more complex materials such as slurries and some suspensions present both yield and pseudoplastic behavior;
- Shear thickening or dilatant fluids, whose apparent viscosity increases with increasing shear rate. Usually, dilatant fluids are thick suspensions of particles in a liquid, like cornstarch in water.

Figure 2.2 - Newtonian and categories of non-Newtonian Fluids.



SOURCE: Adapted from Nguyen e Nguyen (2012).

2.2 Important aspects of gels

Phenomenological characteristics of gels can be specified as (ALMDAL et al., 1993):

- A gel is a mixture containing mostly a liquid;
- A gel is a soft, solid or solid-like material at rest.

According to Almdal et al. (1993), an effort was made during the 20th century to explain gel properties and gelation processes in terms of structure and its changes. Gel definitions based on structural characteristics converged in some aspects and diverged in others.

Nowadays, a wide definition of gel is provided by IUPAC, according to Jones et al. (2007):

Non-fluid colloidal network or polymer network that is expanded throughout its whole volume by a fluid.

Notes: 1 - A gel has a finite, usually rather small, yield stress.

2 - A gel can contain:

2.1 - a covalent polymer network, e.g., a network formed by crosslinking polymer chains or by non-linear polymerization;

2.2 - a polymer network formed through the physical aggregation of polymer chains, caused by hydrogen bonds, crystallization, helix formation,

complexation, etc, that results in regions of local order acting as the network junction points. The resulting swollen network may be termed a thermoreversible gel if the regions of local order are thermally reversible;

2.3 - a polymer network formed through glassy junction points, e.g., one based on block copolymers. If the junction points are thermally reversible glassy domains, the resulting swollen network may also be termed a thermoreversible gel;

2.4 - lamellar structures including mesophases, e.g., soap gels, phospholipids and clays;

2.5 - particulate disordered structures, e.g., a flocculent precipitate usually consisting of particles with large geometrical anisotropy, such as in V_2O_5 gels and globular or fibrillar protein gels.

This work studies the atomization process of liquids and gels, so it is essential to know, up to a certain level, the properties of a gelled material. What is done here, in a basic way, is to consider that the complicated physicochemical properties of the gels can be translated into measurable physical quantities, which have an influence on the atomization process. Certainly, in order to gain an in-depth knowledge on the subject, sometimes it is necessary to turn back to properties at the molecular level. With this in mind, the following sections attempt to describe the fundamental physical quantities used in this work to describe gels.

2.2.1 Shear thinning behavior

As mentioned in section 2.1, shear thinning is characterized by a decreasing apparent viscosity with increasing shear rate. Most gels present this behavior. Gels can be classified according to their rheological properties. As mentioned previously, a constitutive equation can be used to characterize a fluid, through a relation between tension (stress) and deformation (shear rate) (MACOSKO, 1994).

A widely used model, especially for the shear thinning region (Figure 2.3), is the Ostwald de Waele model, or Power-Law (PL) model, given by:

$$\tau = K \left(\frac{\partial u}{\partial y} \right)^n \quad (2.2)$$

$$\mu = K \left(\frac{\partial u}{\partial y} \right)^{n-1} \quad (2.3)$$

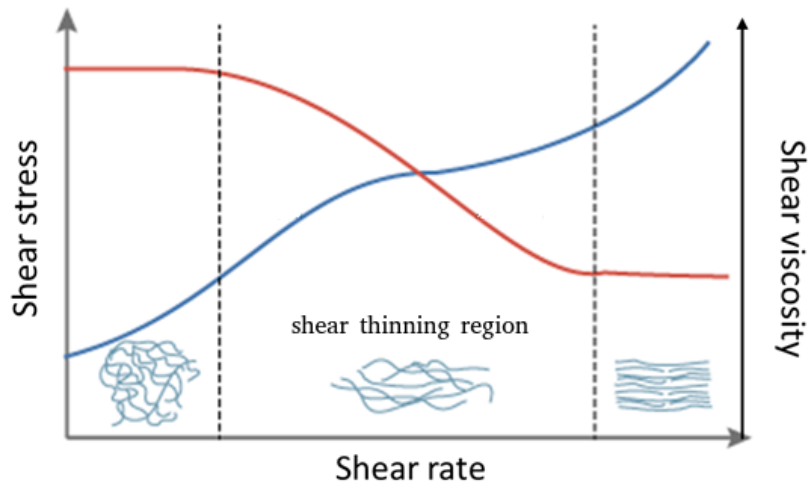
where K , n and $\partial u/\partial y$ are known, respectively, as a flow consistency index, flow behavior index and shear rate or velocity gradient.

The value of n is a measure of the “pseudoplasticity” of the fluid. When $n = 1$,

equations above lead to a Newtonian fluid, since the viscosity becomes constant. When $n < 1$, the viscosity decreases with the increase in shear rate; the closer to 0, the more "pseudoplasticity" a fluid presents. On the other hand, if $n > 1$ the material has a dilating behavior. The value of n can be calculated from the slope of the $\log \mu$ versus $\log \partial u / \partial y$ curve (BRETAS; D'ÁVILA, 2005).

Other models, such as the Carreau model, are able to cover areas from zero to infinity shear viscosity, instead only the shear thinning part, covered by the Power-Law model.

Figure 2.3 - Shear thinning material under flow.



SOURCE: Adapted from [moldex3d \(2020\)](#).

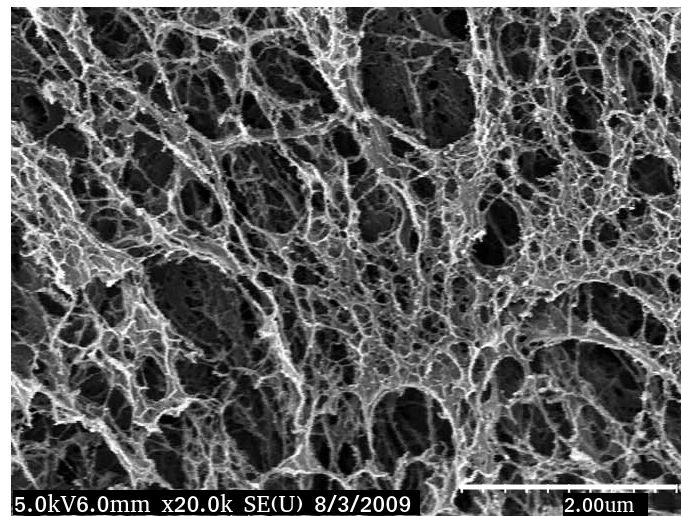
The physical behavior of a shear thinning material depends on the shear rate. Figure 2.3 indicates three viscosity regions, from left to right, called zero-shear viscosity, shear thinning and infinite-shear viscosity regions. At the bottom of Figure 2.3 there is a schematic diagram showing the fluid micro-structures in these three regions. The schematic at zero-shear viscosity region is shown in Figure 2.4, where the presence of polymeric networks is notable. When the fluid is under static or quasi static conditions, the long-chain polymer molecules intertwine and entangle each other. However, as a result of their incessant Brownian motion, the molecules continuously slide over each other, forming and disengaging from individual entanglements as they move. Since entanglements resist flow and viscosity represents the resistance to

flow, under near static conditions, the viscosity at this region is highest, the upper Newtonian plateau (BARNES, 2000).

Increasing shear rate, the number of entanglements reduces as the chains orient along the direction of flow. The fluid therefore shows a gradual reduction in viscosity over the shear-thinning region(LAM et al., 2015).

In a fluid with very high shear rates, the entanglements are combed out by the flow, so the viscosity is at its lowest, the lower Newtonian plateau. At this stage, is expected that the viscosity of the polymer fluid depends only on the underlying viscosity of the solvent (e.g. water, ethanol), the concentration of the non-entangled polymers, temperature, and the chemistry of the solvent used to prepare the solution (LAM et al., 2015).

Figure 2.4 - Carbopol 0.30 wt% (water) obtained with a cryogenic field emission scanning electron microscopy



SOURCE: Adapted from Baek e Kim (2011).

2.2.2 Surface free energy and surface tension

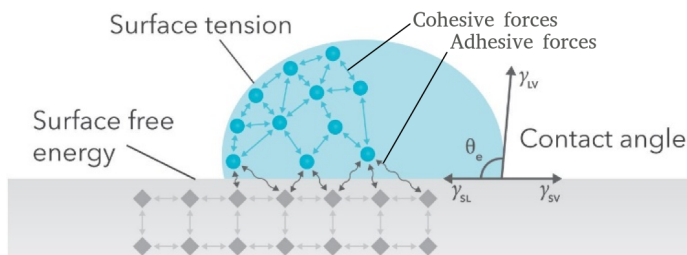
Considering one molecule in a droplet that experience cohesive forces from all the surrounding molecules in a homogeneous environment, this molecule so tend to stay in the drop (Figure2.5). Analyzing molecules on the interface between two phases (for example liquid-solid interface), it is noticeable that in this region, molecules

experience cohesive forces toward the droplet but also some weaker adhesive forces toward the adjacent phase. As a result, a net attraction into the droplet tends to decrease the number of molecules at the surface, leading to an increase in distance between molecules, which requires energy. The excess energy is the reason for the existence of surface free energy and surface tension.

The term free surface energy is commonly used when talking about solid surfaces. When referring to liquids, the term surface tension is more usual. Surface free energy and surface tension differ in concept and unit, but are equivalent (RAPP, 2077):

- Surface free energy: the amount of energy required in order to create a certain surface area, by an isothermal and reversible process, $[J/m^2]$;
- Surface tension: tension force per length acting in all directions along the surface, $[N/m]$, equivalent to $[J/m^2]$.

Figure 2.5 - Liquid drop on a solid surface



SOURCE: Adapted from nanoScience (2020).

There are several methods to measure surface tension and surface free energy, for example, Du Noüy-Padday, bubble pressure, tensiometer, Wilhelmy plate tensiometer, static/dynamic contact angle.

This work uses the static contact angle method, which consists of measuring the contact angle between the solid surface and the liquid droplet in air atmosphere, under controlled temperature. The contact angle (θ_c) is defined by the tangent to the droplet at the contact point with the surface and the tangent to the surface (MOREIRA-JÚNIOR, 2019), and the two tangents belong to a symmetry plane of the drop (Figure 2.5).

Surface free energy is closely linked to the contact angle. The forces that are often present in solid/vapor, solid/liquid and liquid/vapor interfaces are the Van der Waals forces, induced dipoles and dipoles. In these interactions, Pauli Exclusion Principle is also involved (MOREIRA-JÚNIOR, 2019).

Considering the droplet at rest (geometric equilibrium), a balance of tensions yields the Young equation:

$$\sigma_{SV} = \sigma_{SL} + \sigma_{LV}\cos(\theta_c) \quad (2.4)$$

or, alternatively,

$$\sigma_S = \sigma_{SL} + \sigma_L\cos(\theta_c) \quad (2.5)$$

where σ_{SV} (σ_S) is the interfacial tension between solid and vapour, σ_{SL} the interfacial tension between solid and liquid and σ_{LV} (σ_L) the interfacial tension between liquid and vapour (Figure 2.5).

Considering the solid-like behavior of gels at rest, measurement of the contact angle can be done.

Several authors have studied the surface tension of gels.

Nakamura et al. (1996) found that the surface tension of gels suddenly decreases as the gel undergoes the discontinuous volume phase transition (a discontinuous volume change caused by, for example, change in temperature or pH, light irradiation, electric field) and that the surface tension of the poly (n-isopropylacrylamide) gel is mainly governed by the concentration of the polymer chain on the surface of the gel.

Andrade et al. (1979) studied analytically the polymer-water interfaces by contact angle methods using two water-immiscible liquids or a liquid and vapor. The results show that the hydrophilic component dominates the polymer-water interfacial properties, even at relatively low hydrophilic component compositions.

The surface tension of gels in general varies while they are flowing, as a consequence of changes in shear stress rates. However, in all works reviewed (for instance: CONNELL et al. (2018), MALLORY (2012) and BAEK et al. (2011)), the surface tension

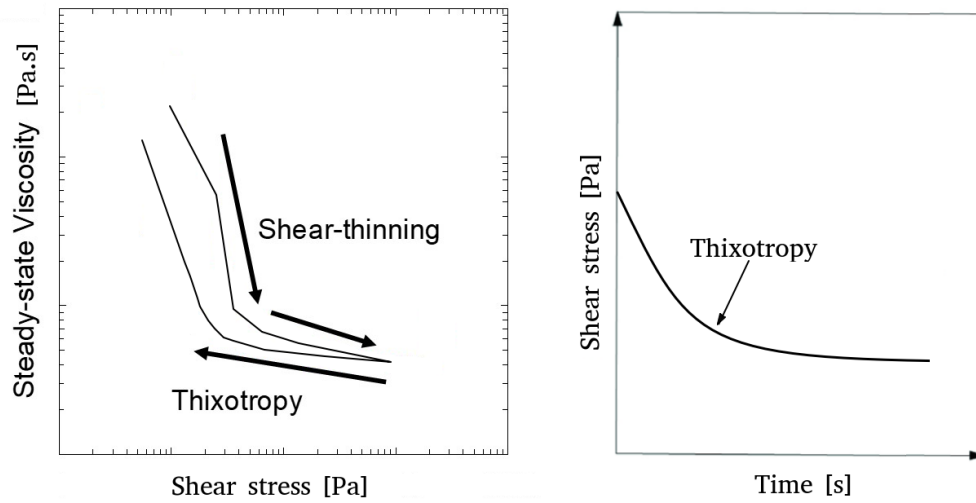
is assumed as constant during the atomization process.

2.2.3 Thixotropy

Thixotropy is the continuous decrease of viscosity with time when flow is applied to a material that has been previously at rest and the subsequent recovery of viscosity in time when the flow is discontinued (Figure 2.6) (BRETAS; D'ÁVILA, 2005).

The complex rheological behavior of thixotropic materials can be understood on the basis of a microstructure that also depends on the shear history. Thixotropic is most often the result of relatively weak attractive forces between the particles. They will cause the formation of flocs, which normally evolve into a space-filling particulate network. The interparticle bonds are, however, weak enough to be broken by the mechanical stresses that occur during flow. The result is that under flow the network breaks down in separated flocs, which decrease further in size when the strain rate is increased. Reducing the shear rate can cause a growth of the flocs; arresting the flow will allow the particulate network to rebuild. Orthokinetic and perikinetic coagulation are the driving mechanisms in this case. The former is related to collisions or contacts of colloids resulting from bulk fluid motion (gradient velocity), the later has similar definition, except for exchanging bulk fluid motion by Brownian motion. The stresses in the suspension depend on the micro-structure and will vary accordingly during or after flow. When the structural changes require a finite amount of time, the same will apply to the stresses, resulting in thixotropic behavior. (MEWIS; WAGNER, 2009).

Figure 2.6 - Thixotropy behavior



SOURCE: Author.

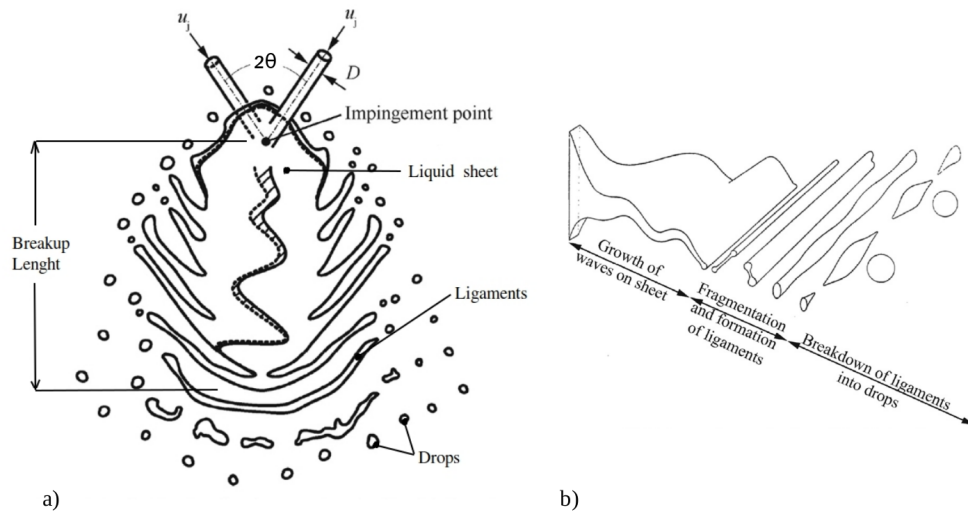
Thixotropy phenomenon is very common in industrial and natural systems. Rheological time effects can be encountered in many industrial activities, including the processing of minerals, metals, food products, pharmaceuticals and ceramics, or when using products such as coatings and paints, gels, inks, drilling muds and concrete (MEWIS; WAGNER, 2009).

2.3 Atomization process by the impingement of jets

Impinging jet injectors are applied to liquid rocket engines, as well as in many chemical processes. Generally, such injectors are used when a rapid mixing between fluids is required, for example, in rapid processes such as certain organic reactions or precipitations at high supersaturation which require the rapid mixing provided by impinging jets mixers (JOHNSON; PRUD'HOMME, 2004), or in rocket engines where a liquid fuel is mixed with the liquid oxidant to be subsequently burned. In order to improve mixing between the two liquids, a fuel jet collides with an oxidizer jet, resulting in rapid atomization and mixing. Experimental and theoretical studies on impinging jet atomization mechanisms (CIEZKI; NE, 2017) (DENG et al., 2018) (CHEN; YANG, 2019) (ASHGRIZ, 2011) show that when two jets with relatively low velocities (low u_j) collide at a certain impingement angle θ , they form initially a sheet in a perpendicular direction to the plane of the jets, then instabilities generate ligaments which are detached from the sheet at a certain breakup length, and eventually form

drops (Figure 2.7a).

Figure 2.7 - Two jet impinging scheme



SOURCE: Adapted from Chen e Yang (2019).

Under typical flow conditions of liquid-propelled rocket engines (as in Figure 1.1d), the sheet of liquid formed by impinging jets suffers a violent rupture caused by rapidly growing instability waves, commonly referred to as impact waves. Impact waves dominate the rupture and atomization processes by impinging jets (CHEN; YANG, 2019).

The film, or sheet, (Figure 2.7b) is produced by a wide variety of injectors, including swirl and impinging jets injectors. When disintegration occurs through the movement of aerodynamic waves, a network of ligaments forms. Figure 2.7b indicates that waves grow on the leaf until they reach a critical amplitude. Ruptures at half the wavelength range occur in the ridges and valleys. The fragments contract into unstable ligaments due to surface tension, which later break into drops (DOMBROWSKI; JOHNS, 1963)(FAKHRI et al., 2010).

Table 2.1 lists some rocket engines that adopt injector plates with impinging jets.

In Table 2.1, P_c is the combustion chamber pressure, d_o is the injector exit orifice diameter, and O and F designate oxydizer and fuel, respectively. The acronyms mentioned are:

Table 2.1 - Rocket engines using injector plates with impinging jets

Rocket Engine	Propellants	O/F	P_c [MPa]	Thrust [MN]	Quantity O/F	Type	$d_o(O/F)$ [mm]
Gemini 1st stage	NTO/A-50	2.00	5.41	0.956	568/516	like	3.05/2.03
Apollo LMDE	NTO/A-50	1.60	1.03	0.047	165	pintle	1.96/1.24
Apollo LMAE	NTO/A-50	1.60	0.203	0.016	177	unlike	0.50/0.40
Long March 3 FY-20	NTO/UDMH	2.21	7.38	0.697	607/605	like	2.70/2.30
Ariane Viking V	NTO/UH25	1.85	5.35	0.680	216/216	like	4.30/2.90
Space Shuttle OME	NTO/MMH	1.65	0.86	0.027	272/272	like	0.81/0.71
Titan I Booster	LOX/RP-1	2.25	4.39	0.801	560/610	like	3.02/2.08
Saturn 1B H-1	LOX/RP-1	2.23	4.86	0.910	365/612	like	3.05/2.08
Saturn 1C F-1	LOX/RP-1	2.27	7.87	6.730	714/702	like	6.15/7.14
Atlas MA-5 Booster	LOX/RP-1	2.28	4.03	1.469	335/582	like	2.87/1.63
Atlas MA-5 Sustainer	LOX/RP-1	2.27	4.87	0.356	144/144	like	3.05/2.39

SOURCE: Adapted from [Bailardi \(2010\)](#).

LMDE – Lunar Module Descent Engine

LMAE – Lunar Module Ascent Engine

NTO – Dinitrogen tetroxide

A-50 – Aerozine 50, fuel mixture for rockets (50% hydrazine/50% UDMH)

UDMH – Unsymmetrical dimethylhydrazine

UH25 – Fuel mixture for rockets (75% UDMH/25% hydrazine)

MMH – Monomethylhydrazine

LOX – Liquid Oxygen

RP-1 – Rocket Propellant-1 or Refined Petroleum-1

Figure 2.8 shows the injection plate (probably first version) of the LMAE developed initially by Bell Aircraft Corporation where engineers struggled with combustion instability problems, later on Rocketdyne Division of North American Aviation developed the replacement injector, which Bell incorporated into the engine ([RR AUCTION, 2017](#)).

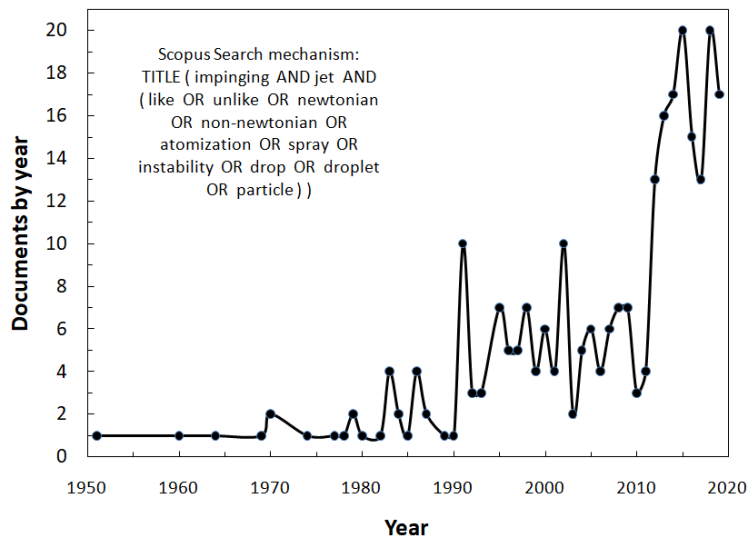
Studies on like and unlike jet impingement have increased significantly in the last ten years, as seen in Figure 2.9 which depicts a Scopus search plot. A total of 267 documents were identified until 2019, approximately 71% of articles, 27% conference papers and 2% others ([SCOPUS, 2020](#)).

Figure 2.8 - Apollo LMAE injection plate



SOURCE: Adapted from RR Auction (2017).

Figure 2.9 - Interest on subject based on Scopus



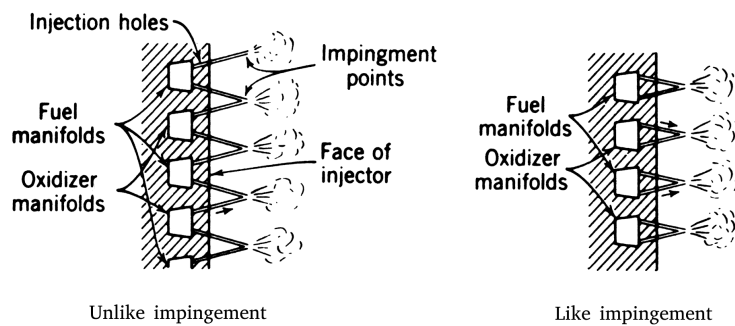
SOURCE: Author.

2.3.1 Like and Unlike impingement

The simplest and most commonly found configuration in real applications is the impingement of two identical liquid jets at an acute angle (2θ), called "like-on-like" or "like-impingement". Figure 2.7a shows a impingement scheme where the center line of the liquid jets intersect at a impinging point (CHEN; YANG, 2019). This configuration has been widely used in liquid propulsion engines. In the case of unlike impingement, two different liquids are collided. A main difference between

like and unlike impingement is the process of mixing. They both have nearly the same atomization mechanism, but in unlike impingement, the mixing starts right from the impingement point. Each pair (like or unlike) generates a spray or fan. The spray of two pairs may have certain inclination with respect to each other, referred to as cant angle. The mass and mixture distribution depend on the orifice sizes, spacing between the two liquids, and cant angle(ASHGRIZ, 2011).

Figure 2.10 - Scheme of Like and Unlike impingement



SOURCE: Adapted from Lefebvre (1988).

2.3.2 Gelled propellants and use of impinging jets

Gelled propellants can provide high propulsive performance, present reduced sloshing and safer handling than conventional liquid propellants. Consequently, research on this subject has increased in recent decades (CIEZKI; NEGRI, 2010). Gelled propellants come from liquids whose rheological properties have been altered by the addition of gelling agents. As a result, the behavior of resting gels resembles that of solid propellants. When flowing, some gels behave like non-Newtonian fluids, simultaneously exhibiting pseudoplastic behavior, as apparent viscosity decreases with increasing stress and thixotropic behavior, i.e. apparent viscosity decreases with time, for the same shear stress.

Research involving gel atomization by impinging jets, as for liquids, has different approaches, for instance, understanding breakup mechanism and instabilities (DENG et al., 2018)(YANG et al., 2013)(RAMASUBRAMANIAN et al., 2015), effects of pseudoplasticity and elasticity (CIEZKI; NE, 2017) (KAMPEN et al., 2006), the influence of temperature (FU et al., 2014), performance for different configurations in terms of

quantity of injectors (CONNELL et al., 2018), effect of adding metallized particles (BAEK et al., 2011) and review articles (AGGARWAL et al., 2015).

2.3.3 Dimensionless numbers in fluid mechanics and usage in atomization processes

Dimensionless numbers are commonly used to analyze fluid flow behavior.

Reynolds number is the ratio of inertial and viscous forces, used to determine whether the fluid flow is turbulent or laminar. For a Power Law fluid, a generalized Reynolds number is defined:

$$Re_{gen} = \frac{\rho u_{gel}^{2-n} D^n}{K[0.75 + (\frac{0.25}{n})]^n 8^{n-1}} \quad (2.6)$$

where ρ is the fluid density, D is the orifice diameter, u_{gel} is the gelled jet velocity, K the flow consistency index, and n the flow behavior index.

For Newtonian fluids, the generalized Reynolds number reduces to:

$$Re = \frac{\rho u_j D}{\mu} \quad (2.7)$$

where u_j is the liquid jet velocity.

Weber number (We) is the ratio between inertia and surface tension forces, widely used in multi-phase flows. For a Newtonian fluid We is given by:

$$We = \frac{\rho u_j^2 D}{\sigma} \quad (2.8)$$

where σ is the surface tension.

Analogously to Reynolds number, Weber number can also be written for a power-law fluid (MALLORY, 2012):

$$We_{gen} = Oh_{gen}^{\frac{2}{2-n}} Re_{gen}^{\frac{2}{2-n}} \quad (2.9)$$

where Oh is the Ohnesorge number ($Oh = \mu/(\rho\sigma D)^{1/2}$), another dimensionless number that relates viscous forces to inertial and surface tension forces. The Ohnesorge number for a power-law fluid is given by (MALLORY, 2012):

$$Oh_{gen} = \frac{K}{(\sigma^{(2-n)}\rho^n D^{(3n-2)})^{1/2}} \quad (2.10)$$

2.3.4 Droplet size

A spray may be considered to be a multi-phase system where droplets are immersed in a gas phase. Injectors are not able to produce a single droplet size, instead, the spray contains a droplet size spectrum (LEFEBVRE, 1988).

Commonly in real problems is convenient to work with mean diameters. A generalized mean diameter can be defined as (LEFEBVRE, 1988):

$$D_{ab} = \left(\frac{\sum N_i D_i^a}{\sum N_i D_i^b} \right)^{1/(a-b)} \quad (2.11)$$

where a and b can have any values corresponding to the effect investigated and $a+b$ is the average diameter order, i denotes the range of droplet size considered, N_i is the number of droplets in the droplet size range i and D_i is the average diameter of the droplet size range of drops i . The droplet size distribution can be represented with two parameters, a representative mean diameter and droplet size range (LEFEBVRE, 1988).

The Sauter Mean diameter is widely used for combustion applications, represented by SMD or D_{32} (when in Equation 2.12 $a=3$ and $b=2$). Some others representative diameters are Dv_{10} , Dv_{50} and Dv_{90} , where 10%, 50% or 90% of the total atomized volume consists of droplets with diameters less than or equal to the indicated value.

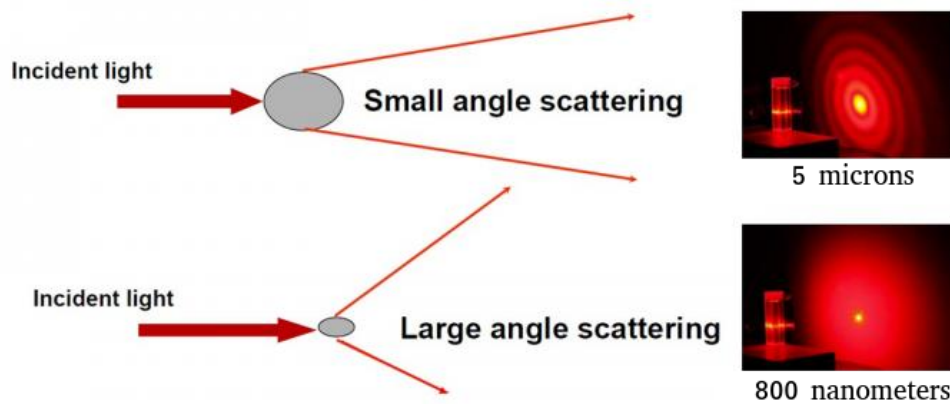
Another important parameter is the Relative Span Factor that indicates the uniformity of the drop size distribution, defined as $\Delta v = (Dv_{90} - Dv_{10})/(Dv_{50})$.

2.3.4.1 Droplet size measurement by laser diffraction

Droplet diameter determination can be done experimentally through the application of laser diffraction methods. Particles that pass through a laser beam produce a deviation or scattering of light at a certain angle, which is directly related to the

size of the droplet. When the droplet size decreases, a logarithmic increase in the spreading angle is observed. The intensity of the spread also depends on the droplet size, which can decrease when the droplet volume increases. Larger particles generally generate light diffraction with narrow angles and high intensity, while small particles are dispersed to wider angles, but with low intensity as shown in Figure 2.11 (VASQUEZ, 2011).

Figure 2.11 - Light scattering patterns of different particle sizes



SOURCE: Adapted from Vasquez (2011).

The particle size distributions obtained by laser diffraction techniques are calculated by comparing the dispersion patterns collected from a given sample to a suitable optical model. Traditionally, two different models of laser diffraction are used: Fraunhofer approximation and the Mie theory. The Fraunhofer approximation considers that the particles being measured are opaque and have light scattering at narrow angles and is applicable only to large particles (generally larger than $90^\circ \mu\text{m}$) resulting an incorrect assessment for the finer particles. Mie's theory offers a more rigorous solution for calculating the particle size distribution related to the scattering of light generated by the same particles. This theory predicts the scattering intensities of all particles, whether small or large, transparent or opaque.

Mie's theory allows the analysis of the primary scattering from the particle surface, with the intensity predicted by the difference in the refractive index between the particle and the dispersion medium. It also provides for secondary scattering caused by the refraction of light inside the particle, which is especially important for parti-

cles with sizes less than 50 microns in diameter, as established by the international standard for laser diffraction measurements (INTERNATIONAL ORGANIZATION FOR STANDARDIZATION. ISO 13320-1.; 1999).

2.4 Shadowgraph imaging technique

Schlieren and shadowgraph techniques are related optical methods since they are made of the same optical stuff. These techniques allow us to see the invisible: the optical inhomogeneities in transparent media like air, water, and glass that otherwise cause only ghostly distortions of our normal vision (SETTLES, 2001).

In this knowledge field, "*schlieren*" is (besides being the common name of the technique) a succinct name for gradient disturbance of inhomogeneous transparent media and "*schliere*" or "*schlieren object*" is the given name for an object generating the phenomenon under study, like a candle plume.

The basic differences between these two techniques are:

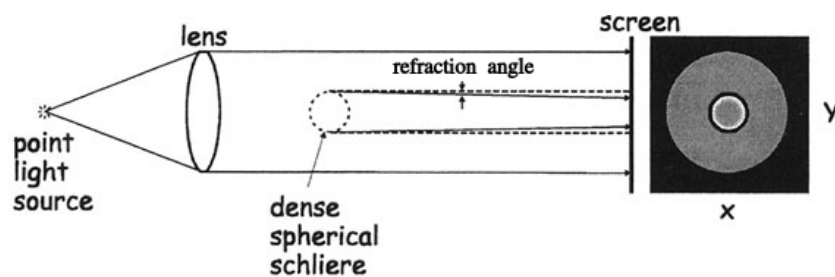
- shadowgram is not a focused optical image; it is a mere shadow. The schlieren image, however, is what it purports to be: an optical image formed by a lens, and thus bearing a conjugate optical relationship to the schlieren object;
- schlieren methods require a knife-edge or some other cutoff of the refracted light, where no such cutoff is needed or allowed in shadowgraphy;
- the illuminance level in a schlieren image responds to the first spatial derivative of the refractive index in the schliere. The shadowgram, however, responds to the second spatial derivative or Laplacian. Equivalently, the schlieren image displays the deflection angle while shadowgraphy displays the ray displacement resulting from the deflection.

Despite distinctions, both schlieren and shadowgraphy are optical systems that project line-of-sight information onto a viewing screen or camera focal plane.

Figure 2.12 shows a scheme with a light source and a lens collimating the light beam. Considering in the beam a spherical schliere of higher refractive index than the surroundings (for example a soap bubble with heavier gas inside). Without the schliere sphere, the light source illuminates the viewing screen uniformly. With the schliere sphere present, some rays are refracted, curved, deflected from their original

paths. Having suffered a refraction through an angle, it reaches the screen displaced from its original position by distance, contributing with extra illuminance to its point, while its previous position suffers an illuminance deficit. That way, considering the entire schlieren object, is verified that optical inhomogeneities redistribute the screen illuminance, causing a shadow, which does not have the same nature as the shadow of a solid object, once shadowgraph technique reveals a wraith (SETTLES, 2001).

Figure 2.12 - Diagram of parallel-light direct shadowgraph observation of a schlieren object



SOURCE: Adapted from Settles (2001).

2.5 Particle Image Velocimetry

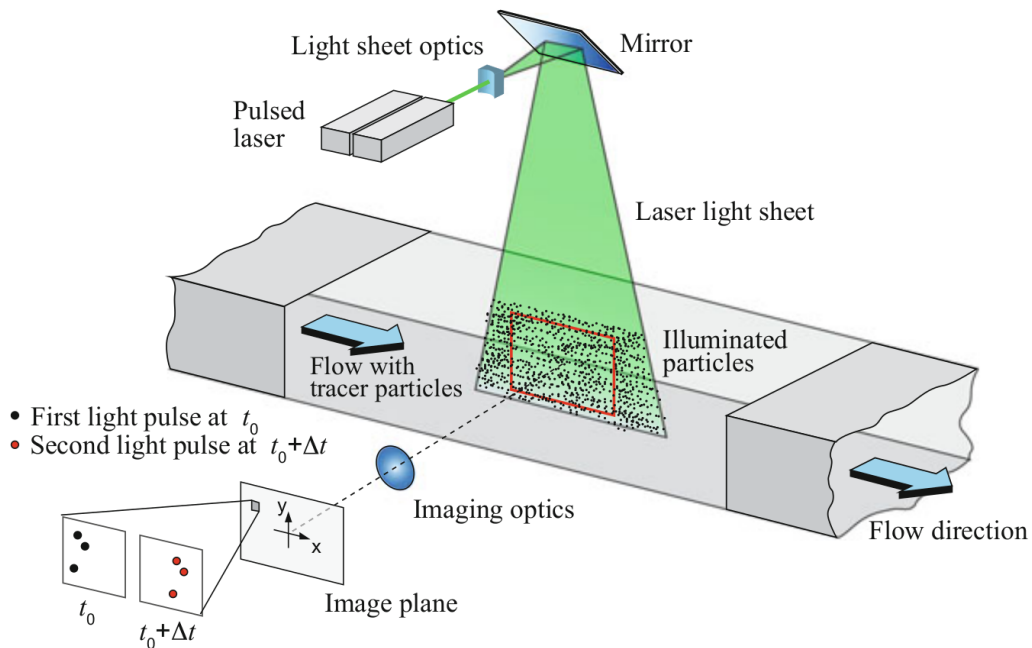
In order to determine a object velocity, distance and time are required. Determining the velocity of a gaseous or liquid flow is not that easy, since they do not contain, in general, moving objects that reveal the velocity of the fluid. During the years, many measurement techniques have been developed to determine indirectly the flow velocity by measuring other quantities and then relate these quantities with velocity by physics relations, some examples are pressure (pressure probes), rotational speed (wind anemometer) and heat transfer (hot film, hot wire). Indirect measurement techniques are easy to use and cheap, their disadvantage is that they may disturb the flow or fluid properties, leading to measurement errors, and that they provide results for a single location. If information about the velocity field is needed, the probe needs to pass through the flow field. As the process of traversing requires some time, only averaged data can be obtained, so an unsteady flow field cannot be obtained using this methods(RAFFEL et al., 2018).

Digital Particle Velocimetry or simply Particle Image Velocimetry (PIV) is an optical qualitative and quantitative flow visualization technique, that allows placing sensors

outside the flow region and to capture images of the whole flow field, overcoming the difficulties of the previously cited methods. One disadvantage is the high cost of the components required for a PIV system.

Figure 2.13 shows a PIV set up in a wind tunnel.

Figure 2.13 - PIV system in a wind tunnel



SOURCE: Adapted from Raffel et al. (2018).

PIV subsystems are typically: seeding, illumination, recording, calibration, evaluation and post-processing. In most applications tracer particle are added to the flow in order to scatter light emitted by the laser. For simplicity it is assumed that the tracer particles move with local flow velocity between the two illuminations.

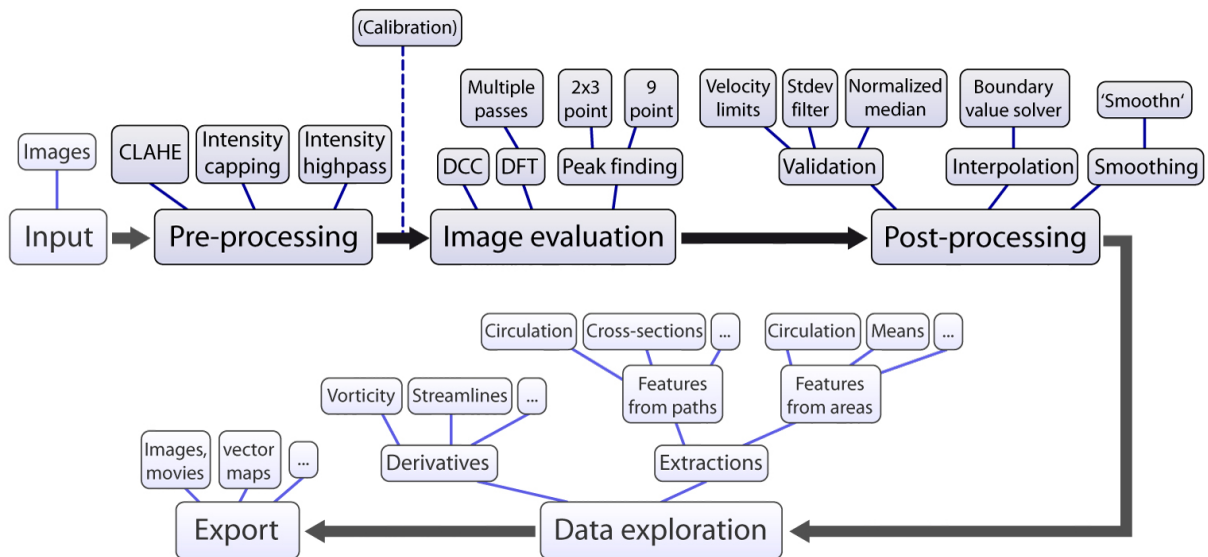
2.5.1 Opensource PIV, low price alternative technique

As mentioned previously, a complete PIV arrangement can be expensive. An attractive alternative is the adoption of individual subsystems, instead of an entire PIV system. For that is needed basically a couple of images with a well know time step between then, and a software to compute data.

About software, there are some options, most of then opensouce, such as DigiFlow,

OpenPIV, JPIV, MatPIV and PIVlab. As an example, in Fig 2.14 is shown a workflow of the PIVlab source, programmed in MATLAB.

Figure 2.14 - PIVlab workflow



SOURCE: Adapted from Stamhuis e Thielicke (2014).

2.6 Infrared (IF) spectroscopy

Spectroscopy is a technique that deals with the the interaction of radiation with matter by emitting, measuring and interpreting spectrum data. There are many different spectroscopic methods for solving a wide range of problems. There are some different types of spectroscopy that are widely used to obtain qualitative and quantitative information based on the absorption, emission or diffraction of radiation in the visible, ultraviolet, infrared and radio-frequency bands. The main objective is to analyse different types of molecular or atomic transitions (PENNER, 2007).

In Infrared (IR) spectroscopy, absorbed IR radiation causes the excitation of molecular vibrations and/or rotations. When an infrared beam is directed towards a sample and it is are excited, the beam is then absorbed at the specific energy of the vibration and loses in intensity at the corresponding wave-number. To get information about the chemical composition of a compound or the structure of an adsorbed species on

a sample, a spectrum is recorded from about 4000 to 400 cm^{-1} and the intensity of the absorbed or transmitted light is plotted against the wave-number. However, not all molecules and functional groups can be detected in an IR spectrum, since the excitation requires a change in the molecules dynamic dipole moment. In general, polar molecules like CO, CO₂ and N₂O are IR-active but non-polar molecules like NO₂ are IR-inactive (RUHR-UNIVERSITÄT BOCHUM, 2020).

2.7 Theoretical models for impingement of jets

During years, researchers have developed theoretical models for impingement jets according their areas of interest, such as:

- Shape of the liquid sheet;
- Thickness and velocity of the liquid sheet;
- Primary atomization process;
- Secondary atomization process;
- Spray angles and distribution;
- Mixing (for unlike impingement).

For atomization processes, instability analysis can be approached with linear or non-linear theories. Some other authors have worked with model coupling, for example primary and secondary atomization coupling under operation conditions, mainly for numerical studies (WEI; G., 2017).

2.7.1 Liquid sheet shape

In order to determine the geometry of liquid sheets, (IBRAHIM; PRZEKVAS, 1991) have conducted an analysis in polar coordinates of force balance on the edges of the sheet (Figure 2.15) and have found a solution as function of Weber number, as follows:

$$r = We \frac{D}{2} \frac{\beta e^{(1-\phi/\pi)} \sin^2 \psi}{4(e^\beta - 1)} \quad (2.12)$$

where r is the radius (edge) of the sheet, We is the Weber number, D is the jet diameter, ϕ the azimuthal angle, ψ is the angle between the velocity vector and

the local tangent of the sheet edge and β is a decay factor determined from mass and momentum conservation, determined by the impinging angle, which can be numerically calculated from:

$$\cos(\theta) = \left(\frac{e^\beta + 1}{e^\beta - 1} \right) \frac{1}{1 + (\pi/\beta)^2} \quad (2.13)$$

where θ is the half-impingement angle.

Considering the angle between the velocity vector and the local tangent of the sheet edge, ψ , as function of ϕ and θ , (IBRAHIM; PRZEKWAS, 1991) proposed:

$$\psi = \frac{\pi}{2} e^{\ln(2\theta/\pi)(1-\phi/\pi)} \quad (2.14)$$

The above equations show good agreement with low viscosity fluids. The authors assumed that the sheet velocity from the impingement point is equal to the jet velocity and neglected viscosity effects, once viscous terms in the model is missing.

Better agreement for high viscosity fluids can be obtained considering viscous effects, by adopting two dimensionless terms, U^{*2} and K^{*2} (HAN, 2016), leading to:

$$r = We \frac{D}{2} U^{*2} K^{*2} \sin^2 \psi \quad (2.15)$$

where U^* is the velocity sheet/jet ratio, $U^* = u_{sheet}/u_{jet}$ and K^* the product of the liquid sheet local thickness by the radial distance divided by the square jet diameter, $K^* = (hr)/D^2$.

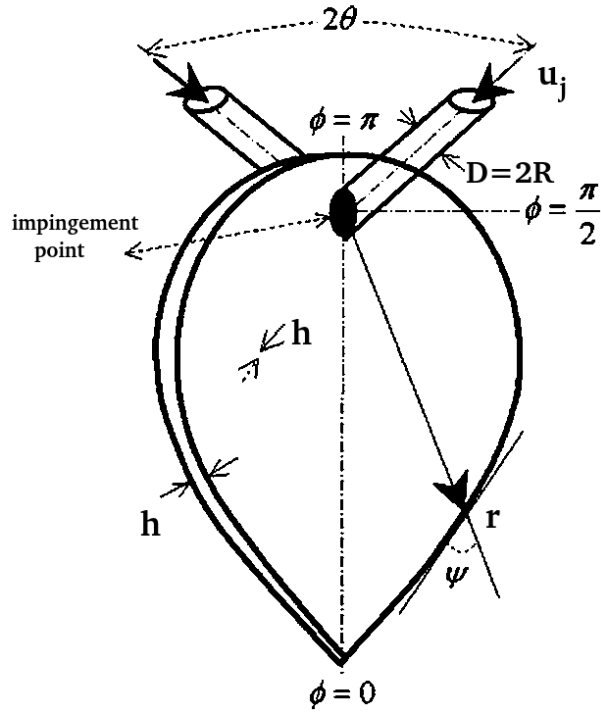
A relation between the local thickness and the radial distance can be used (PECK, 1964):

$$\frac{hr}{R^2} = F(\phi, \theta) = \frac{\sin^3 \theta}{(1 - \cos \phi \cos \theta)^2} \quad (2.16)$$

where R is the jet radius, assumed approximately equal the exit orifice radius.

According to momentum conservation, the angle between the bisector plane of the two jets and the liquid sheet plane is given by (ZHAO et al., 2017):

Figure 2.15 - Important variables in a liquid sheet



SOURCE: Adapted from Ashgriz (2011).

$$\xi = \tan^{-1} \left(\frac{\dot{m}_1 u_{jet1} - \dot{m}_2 u_{jet2}}{\dot{m}_1 u_{jet1} + \dot{m}_2 u_{jet2}} \tan \frac{\theta_1 + \theta_2}{2} \right) \quad (2.17)$$

where \dot{m} represent the mass flow rates of the jets designated by subscripts 1 and 2.

2.7.2 Breakup - Droplet mean diameter

The breakup behavior of impinging jet sprays is function of the fluid properties, impingement angle and free jet conditions, which can be summarized into these parameters: 2θ , Re , We (or Oh , depending on the analyse). For many applications the mean diameter is an important parameter. For combustion processes, the Sauter mean diameter is especially important. So, the prediction of the mean diameter as function of the cited parameters is very important when design injectors.

Five different breakup regimes could be obtained in the operating range, each one with their corresponding instability mechanism, as follows:

- dripping flow;
- rim breakup, Plateau-Rayleigh instability;
- rim-sheet breakup, Plateau-Rayleigh and Kelvin-Helmholtz instability;
- sheet breakup, Kelvin-Helmholtz instability;
- fully developed spray, impact wave and linear stability.

The regimes above fit different areas in a Re versus We or Oh diagram.

Dripping flow occurs at very low jet velocities without impingement, so it is not in this work's scope. Rim breakup occurs also with low jet velocities, it is a typical regime observed during sheet shapes studies (section 2.6.1). The Plateau-Rayleigh instability, sometimes called just Rayleigh instability, describes the phenomenon where a falling jet or cylinder of fluid (in this case, the bottom of the sheet in Figure 2.15) at one point ceases to be a jet and breaks into multiple droplets of smaller total surface area.

Small drops are generated when the sheet breaks up by Kelvin-Helmholtz (KH) and impact wave instabilities, at relatively high jet velocities. Kelvin-Helmholtz occur when there is velocity shear in a single continuous fluid, or where there is a velocity difference across the interface between two fluids, for example, a liquid sheet moving through a previously stationary air ambient.

Was verified that models based on aerodynamic amplification of small periodic disturbances (like KH model) on the sheet formed by the impinging jets be reasonably accurate for relatively low velocities and laminar jets, on the other hand, for high velocities and turbulent jets these models do not faithfully represents trends of breakup length or apparent wavelength (ANDERSON et al., 2006).

The laminar regime is clearly not encountered in rocket engine combustors. As an effort to overcome the difficulties found by the models so far, an empirical model was developed, called "impact wave". The model comprises the three serial processes that are most evident from the visualization studies: impact wave formation and propagation, ligament shedding, and ligament disintegration into drops (ANDERSON et al., 2006).

Still according to Anderson et al., there are three different operating regimes: a laminar sheet regime where the jets are laminar, jet velocities are less than about 5

m/s , and the breakup is predicted fairly well by linear models; the “impact wave” dominated regime, where the jets can be either laminar or turbulent and the ambient density is low to moderate; and an aerodynamic breakup and atomization regime, which is considered to exist at very high ambient densities.

The transition between impact wave and aerodynamically controlled breakup is not well defined, but authors speculate that transition seems to occur around an ambient density of about 20 kg/m^3 . In rocket engine main chambers, operating pressures range from about 1 MPa in pressure-fed engines to 20 MPa in gas generator or staged combustion cycles, these operating conditions correspond to an ambient gas density range of 1 to 20 kg/m^3 , giving an indication that most rocket combustors using impinging jets have the breakup and atomization processes dominated by impact waves (ANDERSON et al., 2006).

2.7.2.1 Breakup - Droplet mean diameter with linear instability model

The principle of linear theory is to solve the linearized governing equations (continuity and momentum) of the liquid sheet with the assumption of linear wave propagation to define boundary conditions. Since the time scale of atomization is often much smaller than heat transfer phenomenon, energy equations are rarely employed (DASGUPTA et al., 2018).

$$\frac{\partial u}{\partial x} + \frac{\partial v}{\partial x} = 0 \quad (2.18)$$

$$\frac{\partial u}{\partial t} + U_{sheet} \frac{\partial u}{\partial x} = -\frac{1}{\rho_{liq}} \frac{\partial p}{\partial x} + \nu_{liq} \left(\frac{\partial^2 u}{\partial x^2} + \frac{\partial^2 u}{\partial y^2} \right) \quad (2.19)$$

$$\frac{\partial v}{\partial t} + U_{sheet} \frac{\partial v}{\partial x} = -\frac{1}{\rho_{liq}} \frac{\partial p}{\partial y} + \nu_{liq} \left(\frac{\partial^2 v}{\partial x^2} + \frac{\partial^2 v}{\partial y^2} \right) \quad (2.20)$$

where u and v is the disturbing velocity in x and y direction, U_{sheet} the mean sheet velocity.

Linear instability considers infinite disturbances traveling on the sheet, the interface movement is usually modeled as a wave function:

$$D = D_o e^{(\beta it)} \quad (2.21)$$

where D is the disturbance amplitude, D_0 the initial disturbance amplitude and β the growth rate. The theory can not predict a critical disturbance for sheet disintegration, therefore an empirical relation is used for that (DOMBROWSKI; JOHNS, 1963):

$$\int_0^{t_b} \beta_{im} dt = \int_0^{x_b} \frac{\beta_{im}}{U_{sheet}} dx = 12 \quad (2.22)$$

In a liquid sheet there are both sinuous (antisymmetric, imaginary part) and dilational (or varicose, symmetric) waves, as in Figure 2.16. Once sinuous waves grow much faster than varicose waves, as a simplification, the later is not considered (CHEN; YANG, 2019)(DASGUPTA et al., 2018)(DOMBROWSKI; JOHNS, 1963).

The wavenumber k_m corresponding to the maximum grow rate β_{im} of the most unstable antisymmetric disturbances for constant thickness, inviscid liquid films is (SQUIRE, 1953):

$$k_m = \frac{\rho_{gas} U_{sheet}^2}{2\sigma} \quad (2.23)$$

$$\beta_{im} = \frac{\rho_g U_{sheet}^2}{(2\rho_{liq}\sigma h)^{(1/2)}} \quad (2.24)$$

where ρ_{gas} is the gas density, σ is the surface tension, and h the sheet thickness. The distance from the impingement point to the point where the sheet disintegrates, called breakup length, x_{bl} is given by (RYAN et al., 1995):

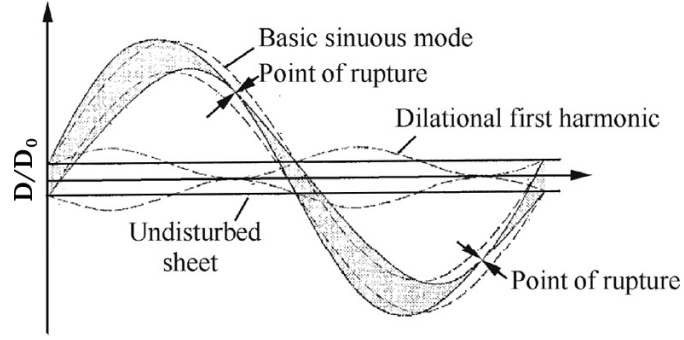
$$\frac{x_{bl}}{d_o} = 5.451 \left(\frac{\rho_{gas}}{\rho_{liq}} \right)^{(-2/3)} (We f(\theta))^{(-1/3)} \quad (2.25)$$

where d_o is the orifice diameter and $f(\theta)$ for $\phi = 0^\circ$ (azimutal angle = 0 is the center-line) is given by:

$$f(\theta) = \frac{\sin^3 \theta}{(1 - \cos \theta)^2} \quad (2.26)$$

Dombrowski and Johns (1963) made an analysis of the aerodynamic instability and disintegration of viscous sheets, and obtained the following:

Figure 2.16 - Dilational and sinuous wave breakup



SOURCE: Adapted from Chen e Yang (2019).

$$d_D = \left(\frac{3\pi}{\sqrt{2}} \right)^{1/3} d_L \left(1 + \frac{3\mu}{\sqrt{\rho_L \sigma d_L}} \right)^{1/6} \quad (2.27)$$

$$d_L = 0.9614 \left(\frac{K^2 \sigma^2}{\rho \rho_L U^4} \right)^{1/6} \left(1 + 2.60 \mu^3 \sqrt{\frac{K \rho^4 U^7}{72 \rho_L^2 \sigma^5}} \right)^{1/5} \quad (2.28)$$

where d_D is the droplet diameter, d_L the ligament diameter, ρ the gas density, ρ_L the liquid density, σ the surface tension, μ the liquid viscosity, K the product hx ; [(sheet thickness). (distance in x -direction)] and U the mean relative air-wave velocity.

Ibrahim and Przekwas (1991) related the drop size to k_m :

$$d_D = \frac{\pi}{k_m} \quad (2.29)$$

and the relation to orifice diameter as:

$$\frac{d_D}{d_o} = \frac{2\pi\sigma}{d_o \rho_g a_s U_{jet}^2} = \frac{2\pi}{We(\rho_{gas}/\rho_{liq})} \quad (2.30)$$

Another stability-based model to calculate d_D was derived by combining Dombrowski and Johns (1963) with Equations 2.23 and 2.25 (RYAN et al., 1995):

$$\frac{d_D}{d_o} = \left(\frac{2.62}{12^{(1/3)}} \right) \left(\frac{\rho_{gas}}{\rho_{liq}} \right)^{(-1/6)} (We_f(\theta))^{(-1/3)} \quad (2.31)$$

According to Ryan et al. (1995) the model described in Equation 2.32 presents good results comparing to D_{10} experimental data by adjusting the empirical breakup constant of 12 (Equation 2.23) to 64.

2.7.2.2 Breakup - Droplet mean diameter with impact wave model

Anderson et al., (2006) studied the stagnation region flow field to evaluate the effects of the pre-impingement jet flow conditions on impact wave formation. To gain insight a finite difference computational fluid dynamics volume-of-fluid (VOF) model was studied, RIPPLE (KOTHE; MJOLSNES, 1992).

A correlation between ligament diameter (d_L) and the orifice diameter (d_o) was found as follows:

$$\frac{d_L}{d_o} = 0.22 \left(\frac{f(\theta)}{\pi} \left[(We_{jet}(\rho_{gas}/\rho_{liq})^2)^{0.102} + 2 \right] \right)^{0.5} \quad (2.32)$$

where We_{jet} is the *Weber* number based on jet properties.

Another correlation was used to describe *SMD*:

$$\frac{SMD}{d_L} = 1.008 (We_{g,lig})^{-0.136} \quad (2.33)$$

where $We_{g,lig}$ was the *Weber* number based on ligament diameter (Equation 2.33) and gas properties, over a range of 1 to 10.5 [bar].

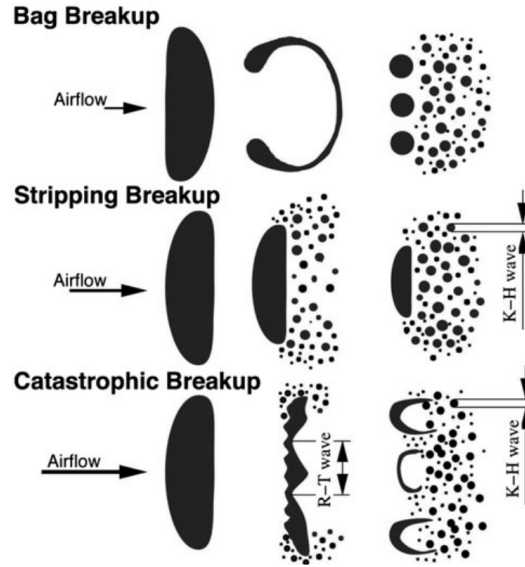
2.8 Secondary atomization

Droplets formed during primary atomization are subject to suffer secondary atomization. Experimental observations (Figure 2.17) was reported and secondary breakup seems to be dependent only on We of the droplet (FAETH et al., 1995).

According to Faeth et al. (1995), the We ranges are:

- $12 < We < 20$, Bag breakup;

Figure 2.17 - Schematic of secondary droplet breakup modes



SOURCE: Adapted from Ashgriz (2011).

- $20 < We < 80$, Multimode breakup;
- $80 < We < 800$, Shear/stripping breakup;
- $800 < We$, Catastrophic breakup.

$$We = \frac{\rho_g u^2 d_0}{\sigma} \quad (2.34)$$

where ρ_g is the ambient gas density, u the droplet velocity, d_0 the initial droplet diameter and σ the surface tension between the fluid and ambient gas.

Still according to Faeth et al. (1995) for high values of the liquid's viscosity the limits of breakup regimes are affected, as the viscosity increases, the value of Weber number required for the onset of breakup increases.

2.9 Droplet collision and coalescence

Droplet collision is a relevant physical process for fluid dynamics in many applications. Such phenomena may significantly modify the spray characteristic droplet sizes and velocities. Many authors consider binary droplet collisions in a spray as a simplification, instead of considers multiple interactions. Experimental results showed five different outcome regimes: coalescence with minor deformation, bounc-

ing, coalescence with large deformation, reflexive separation, and stretching separation (RABE et al., 2010).

Based in experimental results, a criteria for coalescence was proposed:

$$We_s \leq 0.45 \quad \text{and} \quad I < \frac{\sqrt{0.53^2 + 8(0.53We_s)} - 0.53}{4.We_s} \quad (2.35)$$

or

$$0.45 \leq We_s < 2.95 \quad \text{and} \quad 0.28\sqrt{1 - \frac{0.45}{We_s}} < I < \frac{\sqrt{0.53^2 + 8(0.53We_s)} - 0.53}{4.We_s} \quad (2.36)$$

where We_s , δ and I are respectively the symmetric Weber number, diameter ratio and impact parameter, given by:

$$We_s = We \frac{\delta^2}{12(1 + \delta^3)(1 + \delta^2)} \quad (2.37)$$

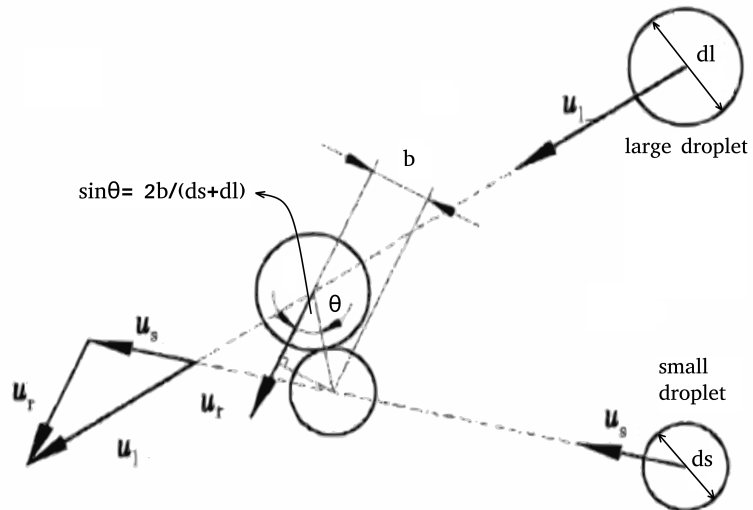
$$We = \rho_d d_s u_r^2 / \sigma \quad (2.38)$$

$$\delta = d_s / d_l \quad (2.39)$$

$$I = 2b / (d_s + d_l) \quad (2.40)$$

where We is the Weber number considering ρ_d as the particle density, d_s the diameter of the smallest droplet (between the two droplets), u_r the relative velocity between the particles and σ the surface tension; small and large droplet diameter d_s and d_l ; b is the distance in Figure 2.18.

Figure 2.18 - Binary collision scheme



SOURCE: Adapted from Huang e HanLiang (2013).

3 METHODOLOGY

3.1 Working fluids

The test fluids employed in this work were water, hydrous ethanol, gelled water and gelled hydrous ethanol. In order to obtain the mass fraction of gelling agent for both commercial gels, drying and spectroscopy were performed.

3.1.1 Newtonian working fluids

Given the large number of tests, tap water was used instead of purified water. Despite mineral salts concentrations (mg/L) may vary depending on water fountain and treatment, differences in surface tension and density of tap water and degassed and doubly distilled water are minimal (PREZIOSO et al., 2018).

Properties of the tap water used in the tests are shown in Table 3.1:

Table 3.1 - Water properties at 20°C.

Property	Value
Density	998.19 [kg/m^3]
Surface tension	72.86 [mN/m]
Viscosity	1.00 [cP] or [$mPa.s$]

SOURCE: Author.

Khattab et al. developed a model to predict viscosity, surface tension and density of binary water ethanol mixtures under temperatures from 293 to 323 K (Equations 3.1 to 3.3).

$$\begin{aligned} \mu_m = X_w \ln \mu_w + X_e \ln \mu_e + 724.652 \left(\frac{X_w X_e}{T} \right) + 729.357 \left(\frac{X_w X_e (X_w - X_e)}{T} \right) + \\ + 976.050 \left(\frac{X_w X_e (X_w X_e)^2}{T} \right) \quad (3.1) \end{aligned}$$

$$\sigma_m = X_w \ln \sigma_w + X_e \ln \sigma_e + 488.012 \left(\frac{X_w X_e}{T} \right) - 640.785 \left(\frac{X_w X_e (X_w - X_e)}{T} \right) + \\ - 1073.310 \left(\frac{X_w X_e (X_w X_e)^2}{T} \right) \quad (3.2)$$

$$\rho_m = X_w \ln \rho_w + X_e \ln \rho_e - 30.808 \left(\frac{X_w X_e}{T} \right) - 18.274 \left(\frac{X_w X_e (X_w - X_e)}{T} \right) + \\ + 13.890 \left(\frac{X_w X_e (X_w X_e)^2}{T} \right) \quad (3.3)$$

where subscripts w , e and m designate, respectively, water, ethanol and mixture and X is mole fraction ($X_w=0.1697$, $X_e=0.8303$, considering H_2O and C_2H_6O).

Liquid hydrous ethanol from Petrobras Company was used and its properties are presented in Table 3.2. Calculated values were based on Equations 3.1 to 3.3 and measured values based on literature.

Table 3.2 - Liquid hydrous ethanol properties.

Property	Value (Calculated ² / Measured ³)
Concentration	¹ 93.8 ~ 92.6 % (w/w)
Density at 20°C	816.48 / 809.3 [kg/m^3]
Surface tension at 20°C	21.10 / 23.00 [mN/m]
Viscosity at 20°C	1.59 / 1.64 [cP] or [$mPa.s$]

¹considering min. and max. % (w/w), (PETROBRAS, 2019)

²calculated for 92.6 % (w/w) and $T = 293.15$ K (KHATTAB et al., 2012)

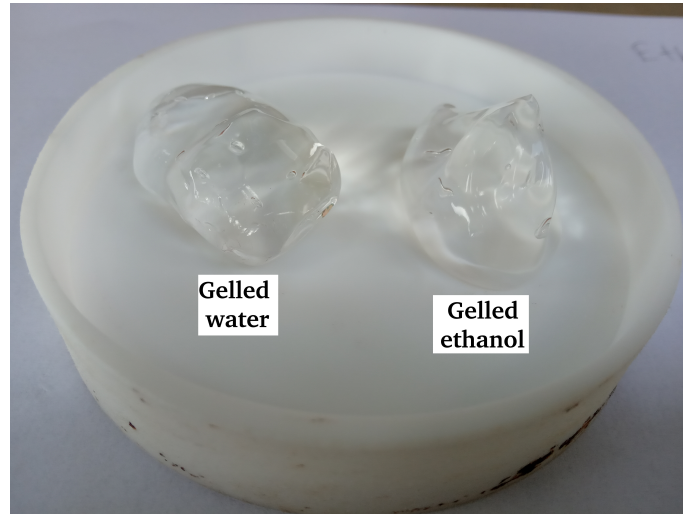
³(FAJGENBAUM; SANTOS, 2013)

SOURCE: Author.

3.1.2 Non-Newtonian working fluids

Commercial gelled water Carbogel Plurigel and commercial gelled hydrous ethanol Quimidrol were used, since a large amount of gelled fluids was required for tests. Figure 3.1 shows a picture of the gelled fluids.

Figure 3.1 - Gelled water and gelled ethanol



SOURCE: Author.

To characterize the gelled working fluid, an Anton Paar rheometer model MCR 72 with spindle parallel plates of 25 mm diameter and 1 mm space between plates was used. A Peltier system was used for temperature control at 25°C during shear rate scanning.

Figure 3.2 shows the viscosity curve of gelled ethanol versus shear rate, adjusted for a power-law fluid.

Figure 3.2 - Rheology - Power law fluid

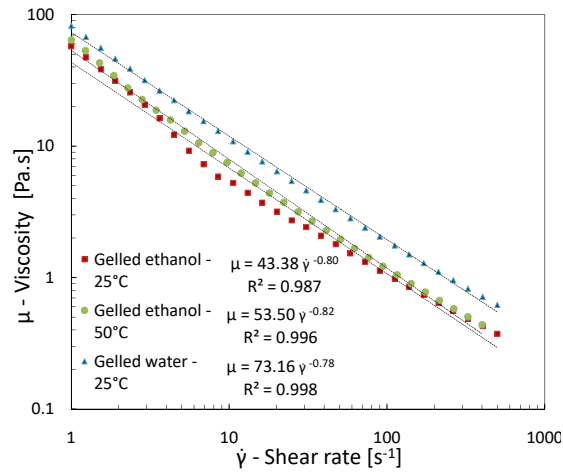
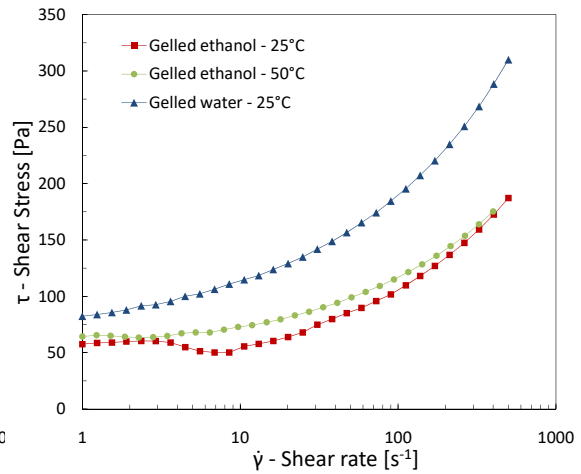


Figure 3.3 - Rheology - Shear stress

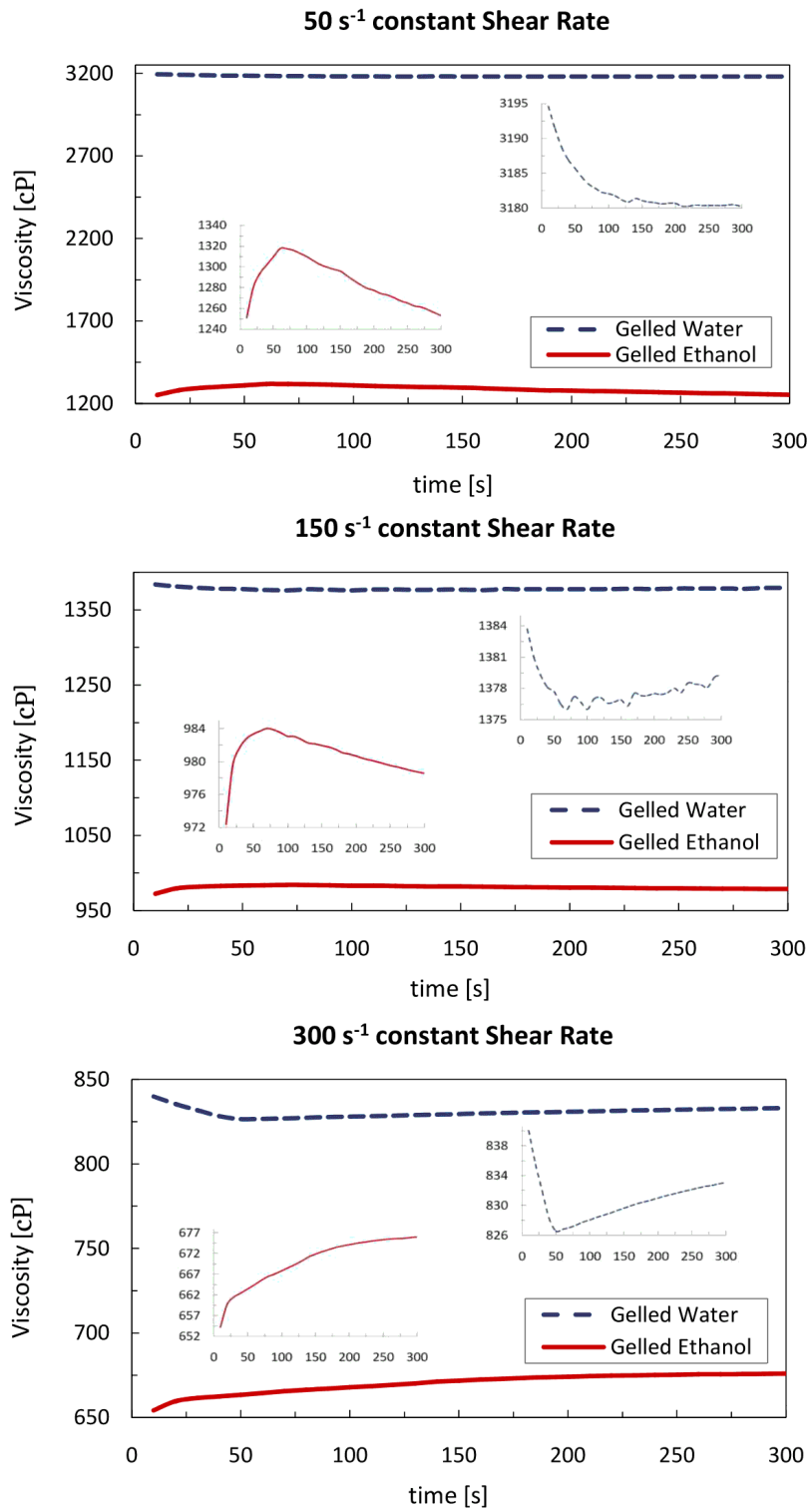


SOURCE: Author.

For a power law characterization at 25°C, the gelled ethanol viscosity is $\mu = 43.38\dot{\gamma}^{(0.20-1)}$ ($K=43.38$; $n=0.20$), whereas gelled water viscosity is $\mu = 73.16\dot{\gamma}^{(0.22-1)}$ ($K=73.16$; $n=0.22$). There is a small increase in viscosity when the sample temperature of gelled ethanol is raised from 25°C to 50°C. Such viscosity increase is expected for Carbopol^o gels (TODICA et al., 2010).

Constant shear rate tests (Figure 3.4) were done for 50, 150 and 300 s^{-1} during 300 seconds in order to verify thixotropic effects (time-dependent viscosity).

Figure 3.4 - Constant shear rate analysis at 25°C



SOURCE: Author.

Small viscosity fluctuations were observed for both fluids, considering the maximum and minimum reached value along 300 seconds, 5.07% and 1.60% were found for gelled ethanol under 50 s^{-1} and gelled water under 300 s^{-1} . Taking into account that the atomization tests in this work occurs in a few seconds (around 2 to 10), no thixotropic behavior was considered. However in real applications, for example, in propulsion systems burning propellants during several seconds, this behavior should be considered.

Gel compositions (Tables 3.3 and 3.4) were verified initially at the Safety Data Sheet for Chemicals (FISPQ) supplied by the chemical manufacturer.

Table 3.3 - Gelled ethanol according to manufacturer FISPQ.

Component	CAS N°	Concentration %(v/v)
Ethanol ¹	64-17-5	70 to 90
Poly(acrylic acid) ²	9003-01-4	0 to 1.5
Ethanolamine ³	141-43-5	0 to 1

¹hydrous ethanol, water content not informed by manufacturer

²gelling agent

³neutralizing agent

SOURCE: Author.

Table 3.4 - Gelled water composition according to the manufacturer FISPQ.

Component	CAS N°	Concentration %(v/v)
Water	7732-18-5	not informed
Glycerol ¹	56-81-5	not informed
Methylchloroisothiazolinone ²	26172-55-4	not informed
Methylisothiazolinone ³	2682-20-4	not informed
Poly(acrylic acid) ⁴	9003-01-4	not informed
Triethanolamine ⁵	102-71-6	not informed

¹thickening agent

²preservative with antibacterial and antifungal effects

³biocide and preservative

⁴gelling agent

⁵neutralizing agent

SOURCE: Author.

Carbopol[®] are high molecular weight, crosslinked polyacrylic acid polymers. A com-

ercial *Carbopol*[®] is a synthetic polymer made of carbomers. Carbomer polymers are cross linked together and form a microgel structure. As these polymers are anionic in nature so neutralization is necessary for microgel structure. Organic amines like ethanolamine and triethanolamine are used for such purpose (UBAID et al., 2016).

Ethanolamine has low toxicity and is noncarcinogenic and can be selected as a base fuel to gel propellants (BOTCHU; BAEK, 2016).

However FISPQ and the manufacturer only provided a list of components and composition ranges for gelled ethanol (Table 3.3) and gelled water (Table 3.4). Therefore, the composition of the gels was experimentally determined. In the next subsections the determination of the gelling additives is described.

3.1.2.1 Drying 1

Initially, samples of gelled ethanol and gelled water were dried in an oven at 80°C for about 400 minutes and in ambient air for 7 days to detect the non volatile components. Samples were weighed by a Shimadzu AUX 220 analytical balance with 0.1 mg scale and the data obtained are shown on Table 3.5.

Table 3.5 - Drying 1 - Residual masses of gelled ethanol and gelled water.

Material	Condition	Initial mass [g]	Residual mass [%]
G. ethanol - sample 1	80°C, 400 min.	30.8484	0.7971
G. ethanol - sample 2	80°C, 400 min.	16.0798	0.7954
G. ethanol - sample 3	ambient, 7 days	22.0548	0.8090
G. water - sample 1	80°C, 400 min.	38.2131	1.4678
G. water - sample 2	80°C, 400 min.	41.9618	1.4832
G. water - sample 3	ambient, 7 days	50.1364	2.6206

SOURCE: Author.

For the gelled ethanol, the oven and ambient dried samples resulted in about 99.2 % of mass loss, while the gelled water presented about 98.5% to 97.4% mass loss comparing oven to ambient dried samples.

3.1.2.1.1 Fourier-Transform Infrared Spectroscopy (FTIR) spectra of dry samples

FTIR tests on dried samples were done as an attempt to determine the remain- ing components by comparing the samples spectra with literature data. A Perkin

Elmer Model Spectrum 100 FT-IR (Figure 3.5), equipped with an Attenuated Total Reflectance (ATR) accessory was used.

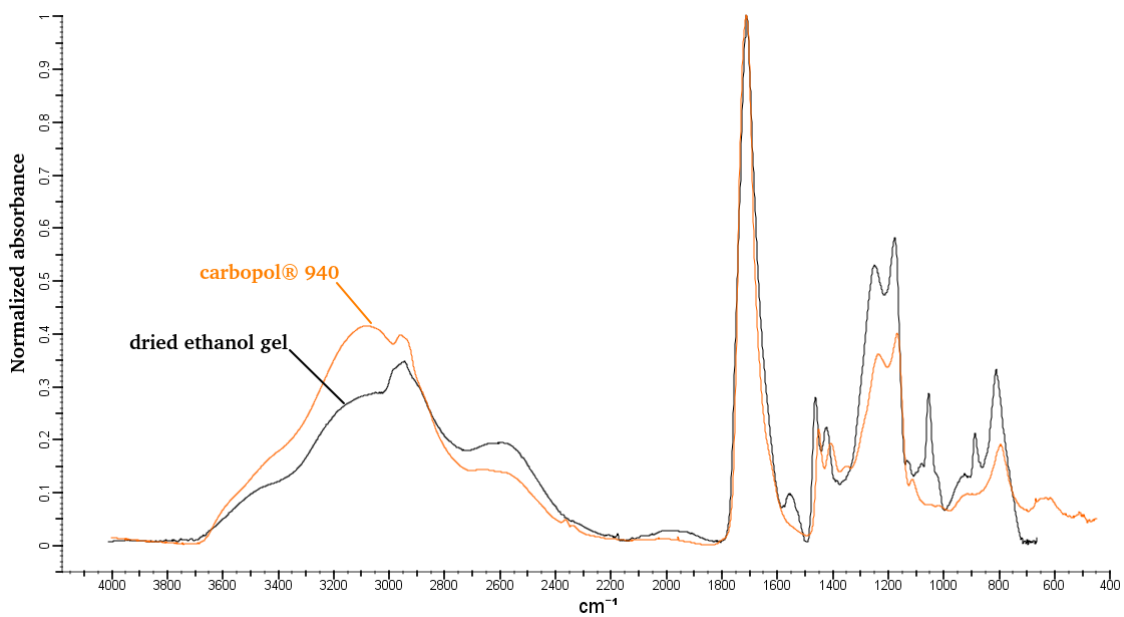
Figure 3.5 - FTIR-ATR spectrometer



SOURCE: Moreira Júnior (2019).

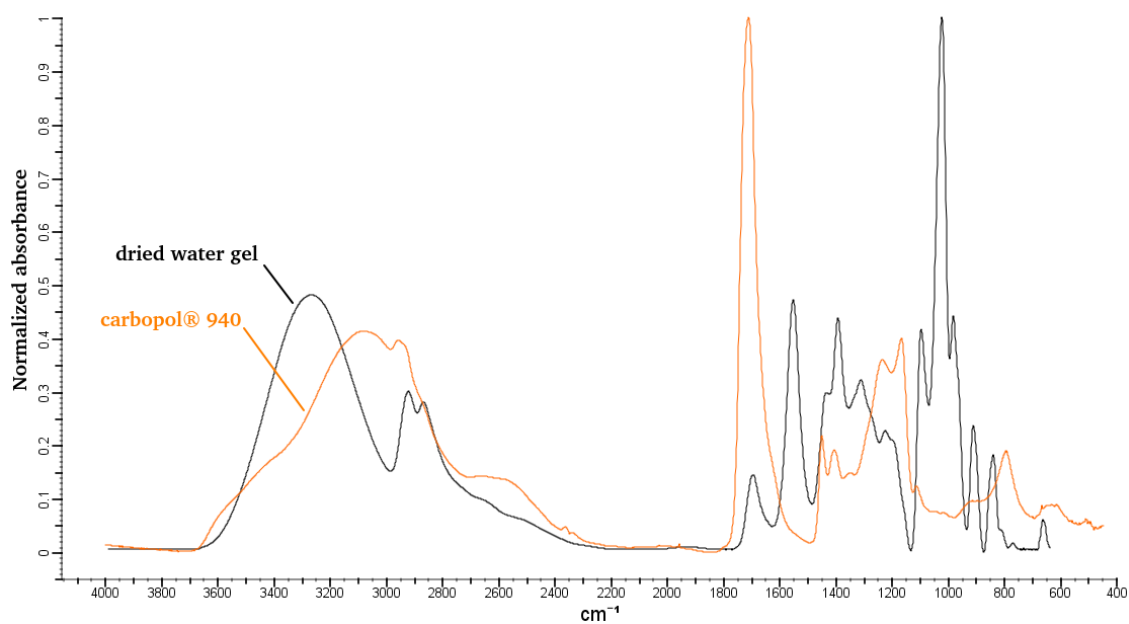
Figures 3.6 and 3.7 depict spectra of gelled ethanol and gelled water with *Carbopol*[®] data (BIO-RAD LABORATORIES, INC. SPECTRABASE, 2019). The graphs are normalized and overlaid in order to allow comparisons.

Figure 3.6 - FTIR spectra of *Carbopol*[®] and dried gelled ethanol.



SOURCE: Author.

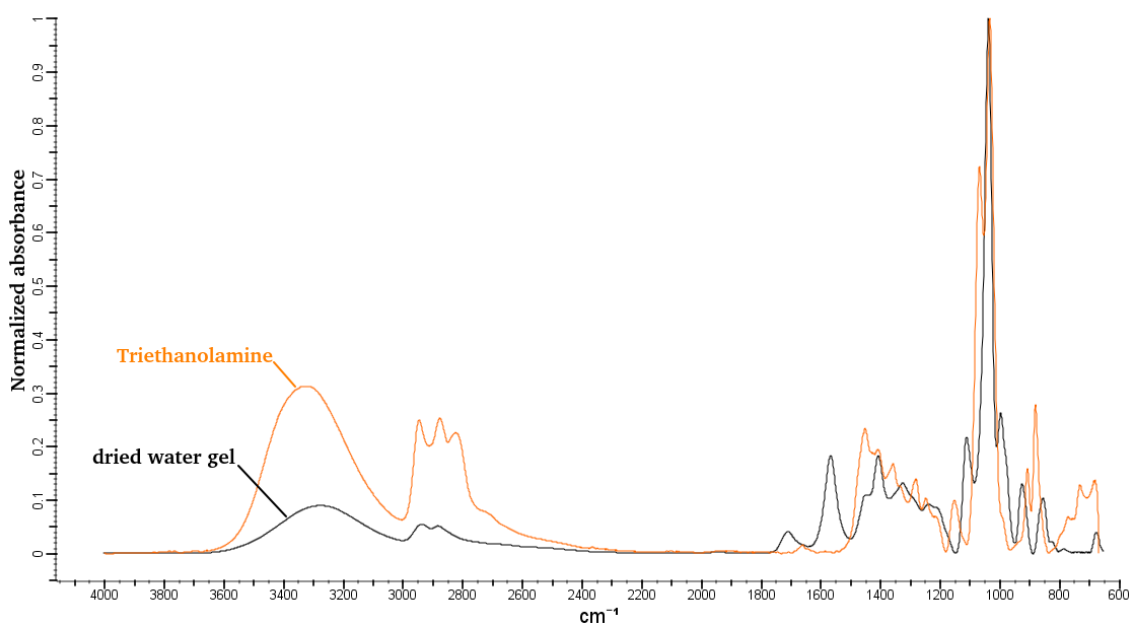
Figure 3.7 - FTIR spectra of *Carbopol*[®] and dried gelled water.



SOURCE: Author.

Comparison of the peaks in the curves (not going into details about absorption groups) indicates that the residual mass of gelled ethanol shows greater similarity to *Carbopol*⁶ than the residual mass of gelled water. Figure 3.8 compares the IR spectra of dried gelled water and triethanolamine, another gelled water component (Table 3.5). Some peaks of dried gelled water sample match the triethanolamine peaks, suggesting that still some triethanolamine remains in the sample. In fact, triethanolamine itself has a boiling point of 335°C.

Figure 3.8 - FTIR spectra of triethanolamine and dried gelled water.



SOURCE: Author.

3.1.2.2 Drying 2

A more severe drying procedure was performed to check the possibility of triethanolamine removal from gelled water and also to check possible changes in remaining mass of gelled ethanol.

In this procedure, samples were dried at 400°C for 300 minutes (heating ramp 10°C/min) and cooled down before removing from oven.

According to the gel manufacturer, decomposition is complete, for all practical purposes, in 30 minutes at 260°C.. The residual mass values in the drying procedure 2

Table 3.6 - Drying 2 - Residual masses of gelled ethanol and gelled water.

Material	Condition	Initial mass [g]	Residual mass [%]
G. ethanol - sample 1	400°C, 400 min.	26.5886	0.609
G. water - sample 1	400°C, 400 min.	19.5447	0.527

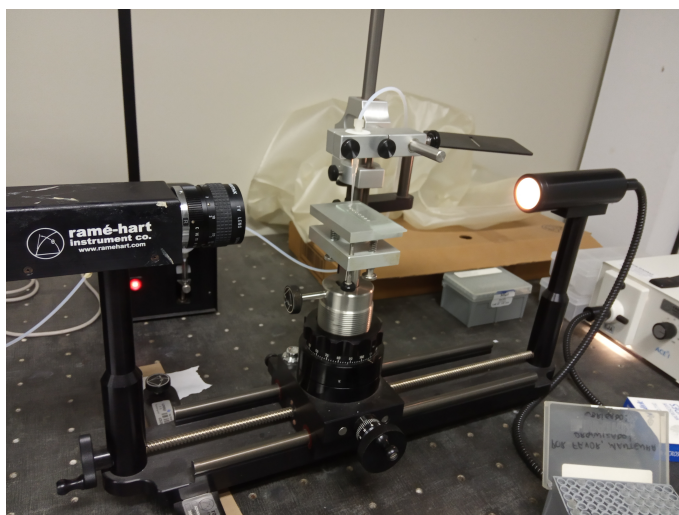
SOURCE: Author.

(Table 3.6) were used to determine the percentage of the gelling additive.

3.1.2.3 Surface tension measurement by contact angle

In order to determine the surface tension of gels in solid-like state, measurements of the contact angles between test fluids and gel surface were made using a Ramé-Hart 300-F1 goniometer (Figure 3.9) in a 20°C controlled temperature room in air atmosphere. Data from the goniometer manufacturer software and from the ORWK method were obtained and compared.

Figure 3.9 - Contact angle goniometer



SOURCE: Author.

Owens, Wendt, Rabel and Kaelble developed a two component model, known as OWRK model, to determine surface tension. The OWRK model considers the geometric mean of the dispersive and polar parts of the liquid surface tension and of

the solid surface energy (OWENS; WENDT, 1969)(RABEL, 1969)(KAELBLE, 1970).:

$$\sigma_{SL} = \sigma_S + \sigma_L - 2\sqrt{\sigma_S^d \sigma_L^d} - 2\sqrt{\sigma_S^p \sigma_L^p} \quad (3.4)$$

The total energy surface is the sum of the two parts. The polar interaction arises due to permanent dipole interactions, i.e., strong interactions that only exist in polar molecules. The dispersive component, also known as London force, is weak and arises from random fluctuations in electron density in an electron cloud, and hence lead to temporary or induced dipoles interactions.

Combining Equation 3.4 with Young equation (Equation 2.6), yields:

$$\frac{\sigma_L(1 + \cos\theta_c)}{2\sqrt{\sigma_L^d}} = \sqrt{\sigma_S^p} \sqrt{\frac{\sigma_L^p}{\sigma_L^d}} + \sqrt{\sigma_S^d} \quad (3.5)$$

where the superscripts in p and d represent, respectively, the polar and dispersive parts of the surface tension.

At least two test fluids are required. Table 3.7 shows data of some usual test fluids:

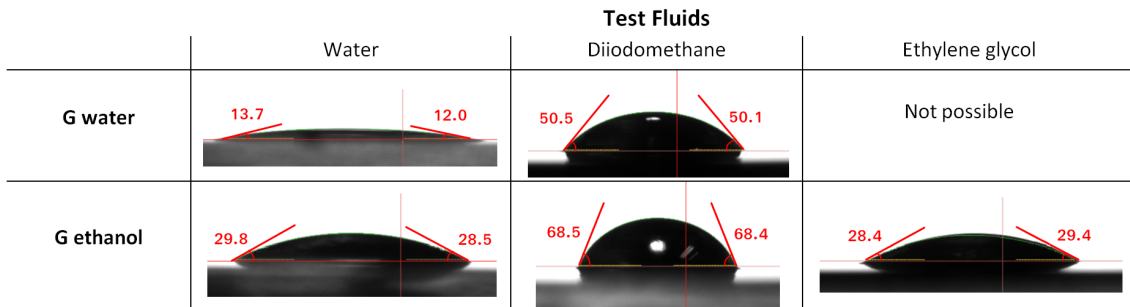
Table 3.7 - Some test fluids and their polar/dispersive components

Fluid	σ_L [mN/m]	σ_L^p [mN/m]	σ_L^d [mN/m]
water	72.8	50.7	22.1
diiodomethane	50.8	2.3	48.5
Ethylene glycol	48.8	16.0	32.8
Formamide	59.0	39.4	19.6

SOURCE: Wu (1982), Oss (2006).

Figure 3.10 shows the contact angles with three test fluids, using the Ramé-Hart 300-F1 goniometer and the DROPimage software supplied by the manufacturer. Table 3.8 presents the surface tension data and contact angles obtained for two test fluids, since the DROPimage software requires only two test fluids to determine the surface tension values.

Figure 3.10 - Surface tension and contact angles using two test fluids.



SOURCE: Author.

Table 3.8 - Result by manufacture software

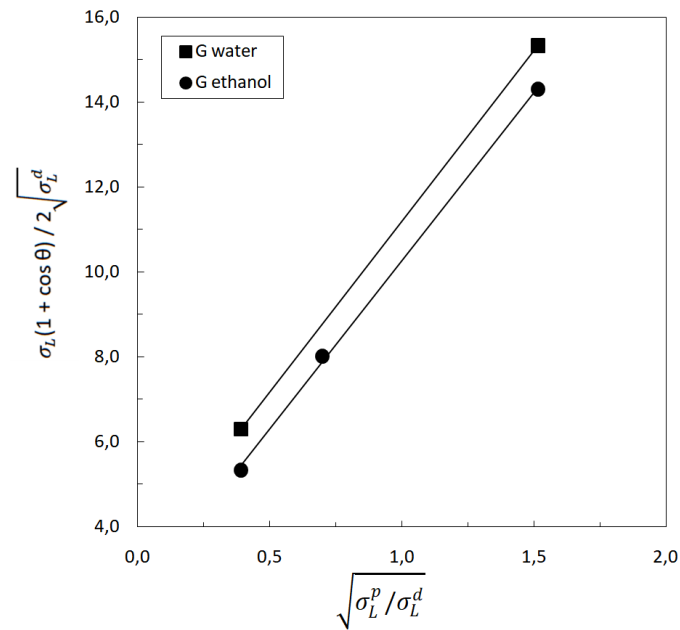
Gel	θ_c -water[°]	θ_c -diiodomethane[°]	σ_L^d [mN/m]	σ_L^p [mN/m]	σ [mN/m]
ethanol	31.91±0.32	66.59±0.63	27.27±0.30	37.27±0.24	64.54±0.20
water	11.11±0.31	49.51±0.17	35.54±0.08	40.37±0.07	76.01±0.07

SOURCE: Author.

Equation 3.5 represents a linear equation given by $y=ax+b$, where a and b are constants. Therefore, plots x versus y were built and the parameters a and b, corresponding, respectively, to the polar and dispersive parts of the gels surface's tensions were obtained (Figure 3.11). Ethylene glycol was used as a third fluid test for gelled ethanol.

Consequently, the linear equation obtained for gelled water was $y = 8.029x + 3.178$ and the linear equation obtained for gelled ethanol was $y = 7.921x + 2.354$. Table 3.9 shows data results from the OWRK method.

Figure 3.11 - Straight lines obtained using the OWRK model.



SOURCE: Author.

Table 3.9 - Result by OWRK method

Gel	θ_c -water[°]	θ_c -dii.[°]	θ_c -ethy. glycol[°]	σ_L^d [mN/m]	σ_L^p [mN/m]	σ [mN/m]
ethanol	31.91±0.32	66.59±0.63	28.02±1.35	5.54	62.74	68.28±5.01% ¹
water	11.11±0.31	49.51±0.17	-	10.10	64.46	74.56±2.81% ¹

¹uncertainty propagation

SOURCE: Author.

There is a significant difference of the dispersive parts of surface energy calculated by the OWRK method and manufacturer software, however, for the purpose of this work, the total (polar + dispersive) surface tension value was used.

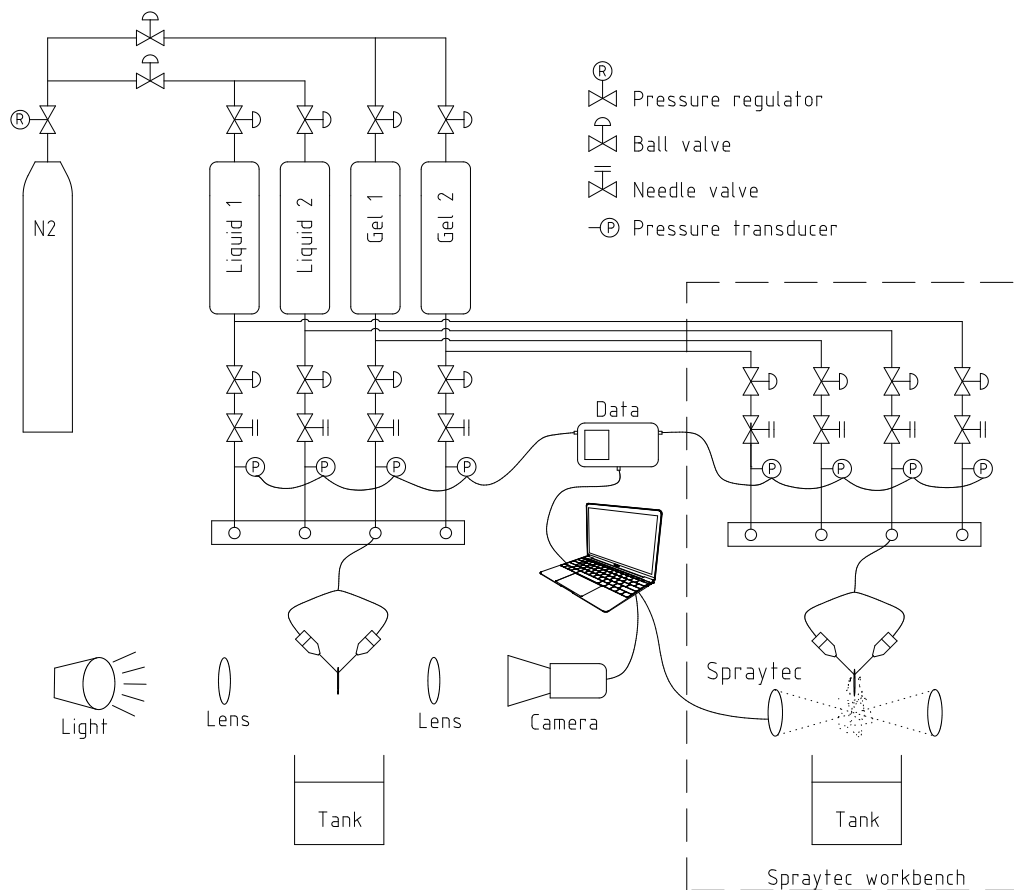
3.2 Workbench and injectors

The scheme of the workbench used in this work is presented in Figure 3.12. The workbench contains two modules with several transducers and devices.

The first workbench module is showed on the left side of Figure 3.12 and contains gelled and liquid propellant tanks, an inert gas cylinder, control valves, pressure data acquisition system, and a setup of light, lens and camera for image capture. Two cameras were used, a Nikon D3100 digital camera with shutter speed 1/3200 seconds and a FASTEC TS3100SC4 high speed camera.

The second module, on the right side of Figure 3.12, contains a Spraytec laser diffraction system, valves and pressure transducers. The second module is connected to the first one in order to have liquid and gas feed lines pressurized.

Figure 3.12 - Workbenches

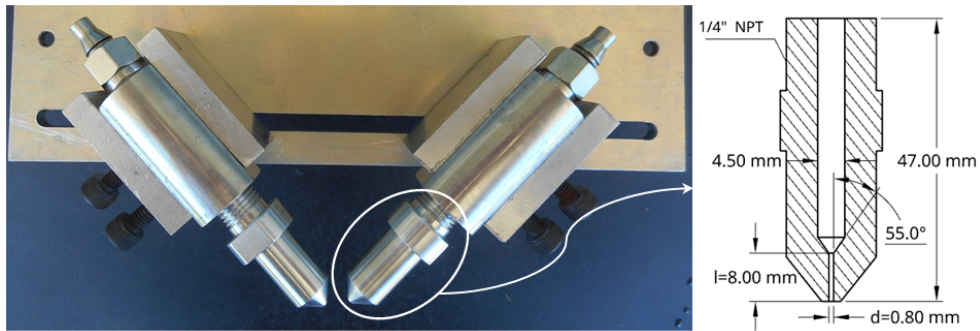


SOURCE: Author.

Since an inlet chamfer can increase the discharge coefficient of a jet injector, inlet-chamfered jet injectors were designed for atomization studies of impinging jets of

liquids and gels, as depicted in Figure 3.13 (DIAS et al., 2019a). Two injectors were manufactured of aluminum 6351 with orifice diameter (d) of 0.8 mm and orifice length (l) of 8.0 mm, resulting in a ratio $l/d=10$.

Figure 3.13 - Inlet-chamfered injectors used for tests.

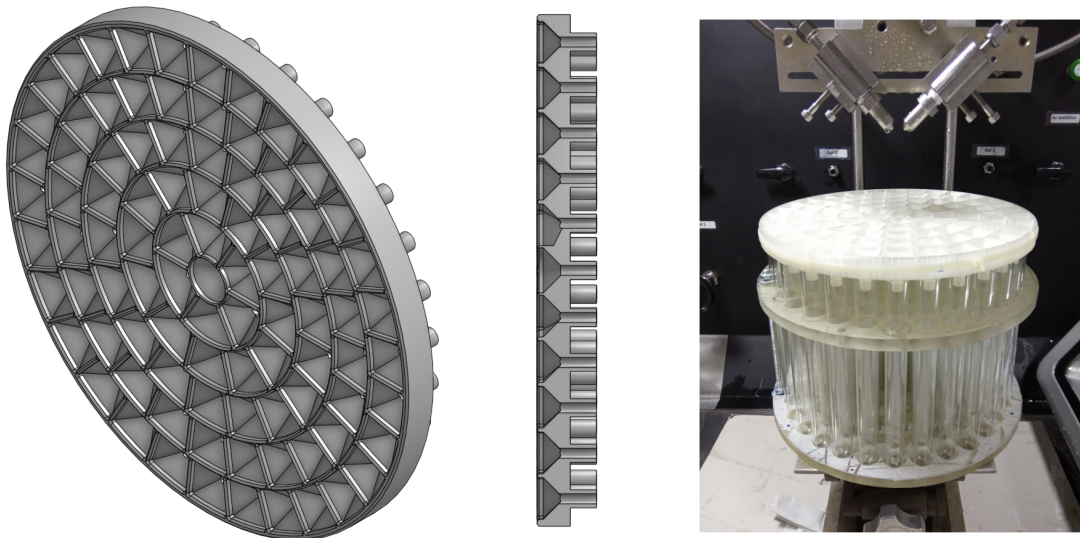


SOURCE: Author.

To estimate the spray distribution and mixing, a circular patternator with 91 orifices of approximately equal areas was designed, as shown in Figure 3.14.

The patternator was manufactured by a 3D-printer using Polylactic Acid (PLA), with collecting glass tubes fixed in a machined polycarbonate suport.

Figure 3.14 - Spray patternator.

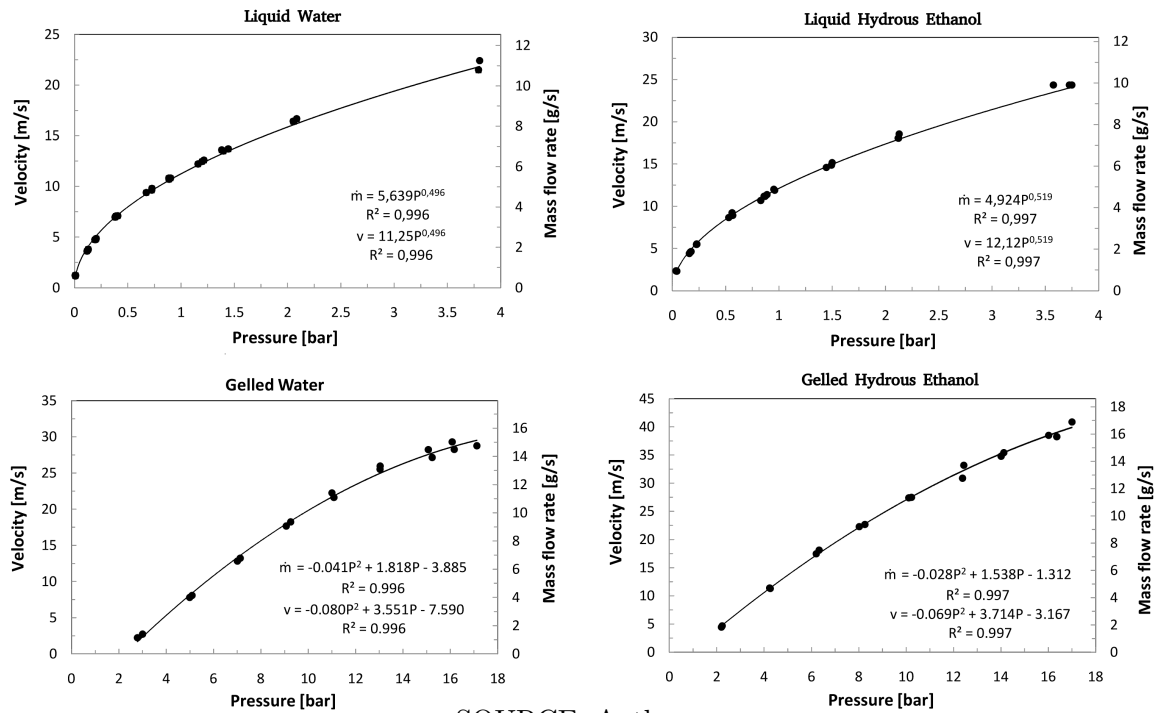


SOURCE: Author.

The working fluids were injected during 10 seconds under a range of pressures. The masses of fluid for each test were collected and measured using a Shimadzu AUX 220 analytical balance.

Figure 3.15 shows the calculated mass flow rates and exit velocities for different injection pressures.

Figure 3.15 - Velocity and mass flow rate versus pressure of working fluids



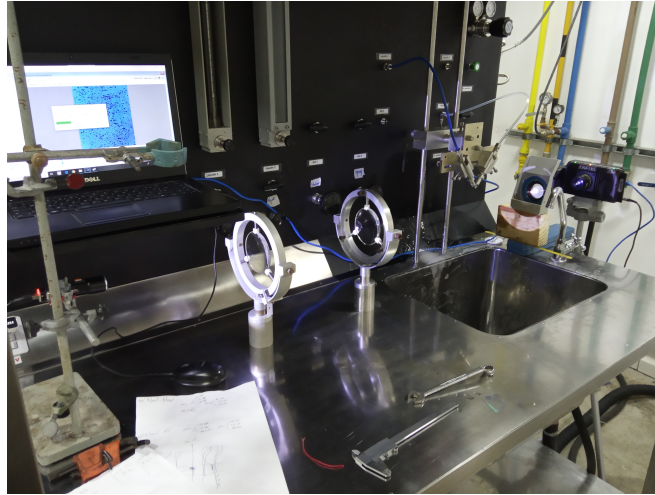
SOURCE: Author.

Fitting curves for mass flow rates and velocities were obtained. As seen in Figure 3.15, the curves for water and ethanol cross the origin, whereas the curves of non Newtonian fluids do not cross the origin, since they require a minimum pressure to flow.

3.2.1 Shadowgraph apparatus

A low cost apparatus for liquid and gel sheet disintegration and subsequent spray formation was configured with overhead projector lenses, LED flashlight and a high speed camera. The best adjustment found for the test window visualization is shown in Figure 3.16.

Figure 3.16 - Shadowgraph apparatus set-up with overhead projector lenses, LED flashlight and a high speed camera.



SOURCE: Author.

3.2.2 Spraytec laser diffraction system - particle size measurement

A Spraytec laser diffraction system was used to estimate droplet size distributions and representative diameters in liquid and gel sprays. Figure 3.17 shows the workbench second module, sketched in Fig 3.12, with the Spraytec diffraction system assembled, connected to the fluid tanks module.

The laser diffraction system allows real-time measurement of particles along a line of sight, with diameters between 0.10 and 2500.00 μm , with path length of 350 mm and lens focal distance of 750 mm. The measured spray region was fixed for all measurements as 50 mm down the center-line of impingement point. In impinging jet injectors, the center-line region presents the largest droplets comparing to the borders.

A polycarbonate device with an exhaust system was adapted to avoid spray fog. Values of laser transmission, representative diameters D_{v10} , D_{v50} , D_{v90} , D_{32} and particle size distributions were recorded continually during approximately 10 to 12 seconds per experimental configuration, adopting the multiple scattering mode. Pressure drops through injectors were recorded with synchronized clock time (Spraytec/laptop/data acquisition system) for further analysis.

Figure 3.17 - Spraytec workbench



SOURCE: Author.

3.2.2.1 Refractive index - qualitative measurement

An input parameter for laser diffraction systems is the refractive index n , a dimensionless number that describes how fast light travels through the material, defined as the ratio between the speed of light in vacuum divided by the phase velocity of light in a medium. In order to check the errors by adopting the gelled fluid refractive index the same as their liquid base, a simple test was done (SILVA; MURAMATSU, 2007).

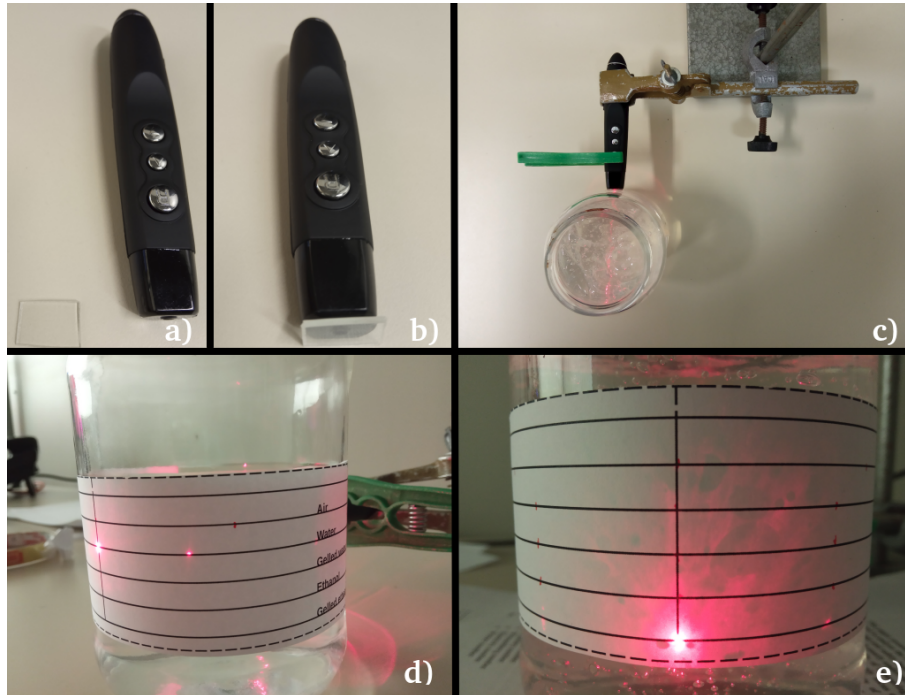
A laser pointer with a fixed rectangular piece of CD media (Figure 3.18 a and b) was placed perpendicularly to a cylindrical glass jar containing the fluid (Figure 3.18 c). A piece of paper with horizontal lines was fixed in the jar in order to mark with pen the points where the laser reaches the paper (Fig 3.18 d and e). The refractive index of the fluid can be obtained approximately by dividing the distance between the horizontal points marked in air by the horizontal distance marked in a liquid or gel.

Figure 3.19 shows the distances measured and Table 3.10 summarizes the refractive

index results. Tiny differences were observed between gels and corresponding liquids.

Since there are no significant differences between the refraction indices of gelled fluids and their base liquids, the fluid base values of literature were used.

Figure 3.18 - Refractive index qualitative test



SOURCE: Author.

Figure 3.19 - Horizontal distances between scattered laser points

	≈ 80.3 [mm]	Air
	≈ 58.0 [mm]	Water
	≈ 58.0 [mm]	Gelled water
	≈ 57.7 [mm]	Ethanol
	≈ 56.5 [mm]	Gelled ethanol

SOURCE: Author.

Table 3.10 - Refractive index, literature and measured

Fluid	n literature	n measured	difference [%]
Water	1.333	1.384	3.8
Gelled water	-	1.384	-
Hydrous ethanol	1.361 ¹	1.391	2.2
Gelled Hydrous ethanol	-	1.421	-

¹(SCOTT, 1946)

SOURCE: Author.

3.3 PIVlab set-up and results verification

The PIVlab v2.30 was used to determine droplet velocities. It features a *multipass window deformation ensemble correlation*, which is especially helpful in micron-resolution particle image velocimetry (micro-PIV), as it can deal with very low seeding densities. This method requires to record a large number of images to obtain a more precise result (PIVLAB, 2019).

Figure 3.20 shows a screenshot of an important set-up on PIVlab, the interrogation area. In Digital PIV, the particle movement is calculated for groups of particles by evaluating the cross-correlation of many small sub images, called interrogation areas. The correlation yields the most probable displacement for a group of particles travelling on a straight line between two images (STAMHUIS; THIELICKE, 2014). When the areas overlap one another by, for example, 50% (step, Figure 3.20), there is additional displacement information at the borders and corners of each interrogation area. This information is used to calculate displacement information at every pixel of the interrogation areas via bi-linear interpolation (STAMHUIS; THIELICKE, 2014).

In order to get more accurate results, more passes (2 to 4 passes) are allowed. Their values do not need to be power of two as in Figure 3.20 (64, 32).

The peak finding technique is, as the cross correlation technique, an important factor for the accuracy of Digital PIV. The integer displacement of two interrogation areas can be determined directly from the location of the intensity peak of the correlation matrix. The location can be refined with sub-pixel precision using different procedures (STAMHUIS; THIELICKE, 2014). The standard procedure is to fit a Gaussian function to the integer intensity distribution. It is sufficient to use only the directly adjacent vertical and horizontal pixels (two times a 3-point fit = 2x3-point fit) and to evaluate the x and y axis individually (PIVLAB, 2019).

Figure 3.20 - PIVlab ensemble correlation setup

The image shows a software interface for PIVlab ensemble correlation setup. It is organized into several sections:

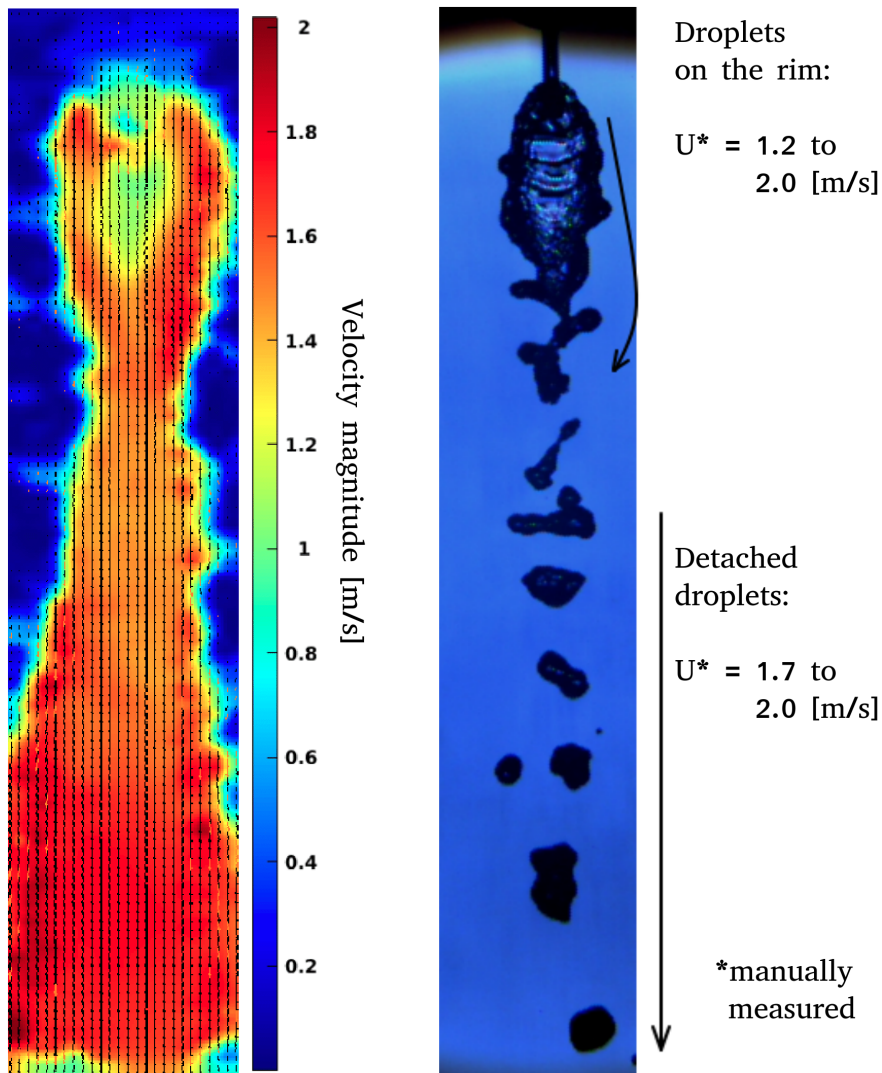
- PIV algorithm:** Three radio buttons are present: "FFT window deformation" (unselected), "Ensemble correlation" (selected), and "DCC (deprecated)" (unselected).
- Pass 1:** A table with two columns: "Interrogation area" and "Step". The value "64" is entered in the "Interrogation area" field, and "32" is entered in the "Step" field. Below the "Step" field, the text "= 50%" is displayed.
- Pass 2...4:** A table with two columns: "Interrogation area" and "Step". Each row represents a pass:
 - Pass 2: A checked checkbox is to the left of the "Interrogation area" field, which contains "32". The "Step" field contains "16".
 - Pass 3: An unchecked checkbox is to the left of the "Interrogation area" field, which contains "32". The "Step" field contains "16".
 - Pass 4: An unchecked checkbox is to the left of the "Interrogation area" field, which contains "32". The "Step" field contains "16".
- Sub-pixel estimator:** A dropdown menu is set to "Gauss 2x3-point".
- Disable auto-correlation:** An unchecked checkbox.
- Correlation quality:** A dropdown menu is set to "Normal (recommended)".

SOURCE: Author.

In this work, the shadowgraph images obtained with the high speed cameras with known time-steps were used to obtain the droplets velocities in specific cases. To calibrate the distance scale on PIVlab a picture of a caliper with 30 millimeters aperture was used.

In order to verify the method accuracy, velocities of six images in a row were calculated by hand from the changes in distances between recognizable droplets.

Figure 3.21 - Velocity comparison - measured by hand vs PIVlab.



100 frames: water, impingement angle 75° , jet velocity = 2.55 [m/s]

SOURCE: Author.

Figure 3.21 shows the manually calculated velocity magnitudes for 6 frames compared with the velocity field obtained by PIVlab for 100 frames. For manual calculations, detached particles were assumed to have only vertical movement while droplets on the rim had 2D movement. Droplets velocities on the rim were verified to have 1.5 m/s maximum values, such value were encountered by plotting velocities (magnitude) values over a line manually positioned in the rim. Detached droplets under the same procedure obtained a maximum value of 1.8 m/s. Taking the average value of manually measured velocities, the encountered error goes from 6.7% on the

rim to 2.8% the detached droplets. It is interesting to note that not only droplets can be tracked by the PIVlab software, but also the instabilities on the sheet.

3.4 Working fluids properties - overview

A summary of the working fluids properties is given in Table 3.11.

Table 3.11 - Working fluids properties - Overview

	Water	Ethanol	Gelled Water	Gelled Ethanol
$\rho[kg/m^3]$	998.19	816.48	1001.00	824.20
$\sigma[mN/m]$	72.86	23.00	74.56	68.28
$\mu[mPa.s]$	1.00	1.64	-	-
Refractive Index	1.33	1.36	1.33	1.36
K (Power Law)[$mPa.s^n$]	-	-	73.16	43.38
n (Power Law)[-]	-	-	0.22	0.19
Gelling Agent [%wt]	-	-	0.53	0.61

SOURCE: Author.

Observations:

- n of power law is related with wt% of the gelling agent, however other factors such curing procedure may affect n;
- The liquid phase of gelled ethanol is hydrous ethanol;
- The liquid phase of water ethanol is water-glycerin solution 5%wt (95% water);
- k of gelled water is greater than that of gelled ethanol due the usage of glycerin, which is a thickener, but not a gelling agent.

3.5 Experimental uncertainty

Experimental data are frequently used to support engineering analysis as a basis for design. Uncertainty analysis is the procedure used to quantify data validity and accuracy. The main objective of uncertainty analysis is to estimate the random error in experimental results, assuming that fixed error are not occurring (FOX et al., 2011).

Such uncertainty propagates during calculations and, at the final result, the reached uncertainty value may be unacceptable for certain application.

Relative uncertainty u_R for a given result R is given by (KLINE; MCCLINTOCK, 1953):

$$u_{R_i} = \frac{x_i}{R} \frac{\partial R}{\partial x_i} u_{x_i} \quad (3.6)$$

where u_{x_i} is a measurement of an independent variable i .

The relative uncertainty in u_R caused by the combined effects of the relative uncertainties in all x_i is given by (KLINE; MCCLINTOCK, 1953):

$$u_R = \pm \left[\left(\frac{x_1}{R} \frac{\partial R}{\partial x_1} u_{x_1} \right)^2 + \left(\frac{x_2}{R} \frac{\partial R}{\partial x_2} u_{x_2} \right)^2 + \dots + \left(\frac{x_n}{R} \frac{\partial R}{\partial x_n} u_{x_n} \right)^2 \right]^{1/2} \quad (3.7)$$

The maximum value for relative uncertainty u_{max} was calculated considering half of least count scale and the smaller measured value during experiments, $u_{max} = [(Least\ count/2)/Smaller\ value] \times 100$. Table 3.12 shows adopted values during calculations.

Table 3.12 - Adopted uncertainty

Quantity [unit]	Notation	Smaller value	Least count	u_{max} [%]
mass [g]	u_m	12.0	0.01	0.0417
mass ¹ [g]	u_m^1	1.0	0.0001	0.005
time [s]	u_t	10.0	0.5	2.5
volume [ml]	u_{vol}	50.0	1.0	1
diameter [mm]	u_d	0.8	0.01	0.625
surface tension [mN/m]	u_σ	-	-	5.01

¹Analytical balance, for mixing test

SOURCE: Author.

Uncertainties were calculated for exit injector area u_A , density u_ρ , mass flow rate $u_{\dot{m}}$, jet velocity u_{vel} , jet momentum u_{mv} , Reynolds number u_{Re} and Webber number u_{We} . Equation 3.7 yields:

$$u_A = \pm \left[(2u_d)^2 \right]^{1/2} \quad (3.8)$$

$$u_\rho = \pm \left[(u_m)^2 + (-u_d)^2 \right]^{1/2} \quad (3.9)$$

$$u_{\dot{m}} = \pm \left[(u_m)^2 + (-u_t)^2 \right]^{1/2} \quad (3.10)$$

$$u_{vel} = \pm \left[(u_{\dot{m}})^2 + (-u_\rho)^2 + (-u_A)^2 \right]^{1/2} \quad (3.11)$$

$$u_{mv} = \pm \left[(u_{\dot{m}})^2 + (u_{vel})^2 \right]^{1/2} \quad (3.12)$$

$$u_{Re} = \pm \left[(u_\rho)^2 + (u_{vel})^2 + (u_d)^2 + (-u_\mu)^2 \right]^{1/2} \quad (3.13)$$

$$u_{We} = \pm \left[(u_\rho)^2 + (2u_{vel})^2 + (u_d)^2 + (-u_\sigma)^2 \right]^{1/2} \quad (3.14)$$

The displayed pressure, according to the transducer manufacturer, presents uncertainty of $\pm 0.5\%$. The pressure range was from about 0.05 to 18 [bar]. Viscosity and surface tension for Newtonian fluids were not measured in this work, therefore their uncertainties were not considered. Non Newtonian surface tension was measured and the value was provided by the contact angle goniometer, however it did not affect substantially the generalized Webber number uncertainty. For impingement angle 2θ half of least count was adopted, 0.5° .

Table 3.13 shows the calculated uncertainties considering u_{max} on Table 3.12 applied on Equations 3.8 to 3.14.

Table 3.13 - Calculated experimental uncertainty.

Uncertainty	Result \pm
u_A	1.25 [%]
u_ρ	1.00 [%]
$u_{\dot{m}}$	2.50 [%]
u_{vel}	2.97 [%]
$u_{\dot{m}v}$	3.88 [%]
u_{Re}	3.19 [%]
u_{We}	6.05 [%]
$u_{We_{gel}}$	7.86 [%] ¹
$u_{2\theta}$	0.5°

¹considering surface tension measurement for gels

SOURCE: Author.

4 RESULTS

This chapter presents experimental and theoretical results about the atomization by impinging jets of liquid water, gelled water, liquid hydrous ethanol and gelled hydrous ethanol. Data about the following topics are presented:

- pre-impingement jet conditions;
- sheet shapes of collisions of liquids and gels;
- atomization with image visualization, representative diameters and particle size distribution, for like and unlike jet impingement;
- spray mass distribution and mixing for liquids;
- droplet velocities.

During the atomization tests, pre-impingement distances varied from 6 to 10 mm and injection pressures (pressure drops through the injectors) ranged from 1 to 3.5 bar for liquids and from about 7 to 17 bar for gelled fluids with like impingement.

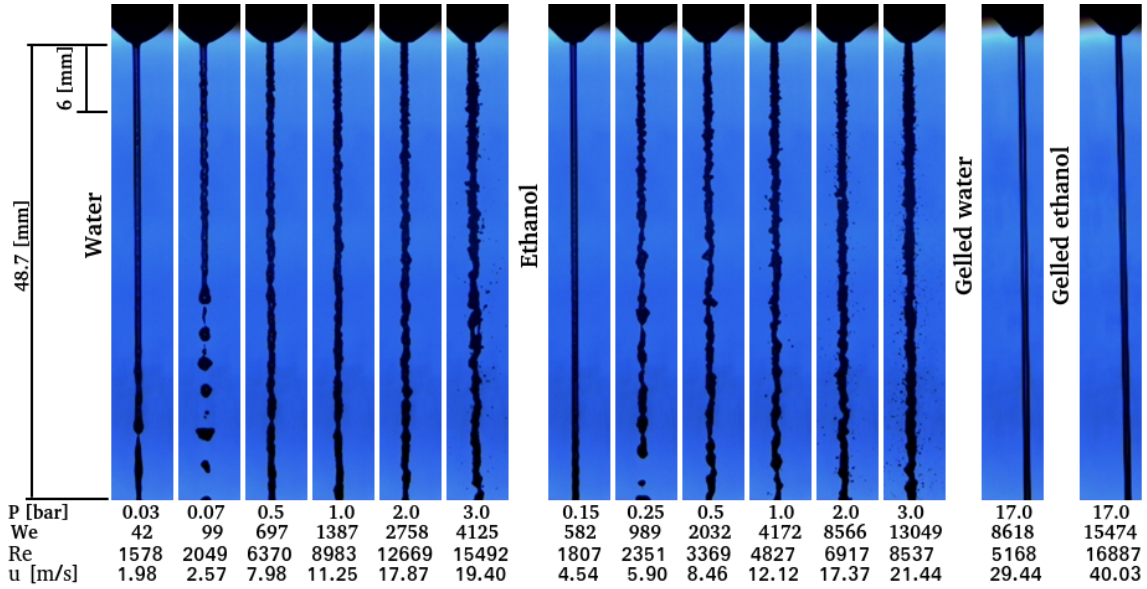
4.1 Pre-impingement jet conditions

The injector geometry significantly effect the exit flow, which may state as turbulent, traction or laminar regime before jet collision. In rocket engines during operation, impinging jets of liquid propellants are turbulent (ANDERSON et al., 2006). Pre-impingement jet behavior affects the formation of instabilities on the liquid/gel sheet and, consequently, influences the spray formation.

Figure 4.1 shows shadow images of single round jets for the test fluids with different injection pressures and We numbers.

Liquid jets of water and hydrous ethanol were in laminar regime only for small injection pressures and there is transition from laminar to turbulent regimes for most injection pressures. Plateau-Rayleigh instabilities are verified for water and liquid ethanol jets ($We=99$ and $We=989$, respectively). The jets of gelled hydrous ethanol stay in the laminar regime for a longer distance than liquid jets, even at a high injection pressure.

Figure 4.1 - Free jets in ambient air for increasing injection pressures.



SOURCE: Author.

4.2 Collision sheet shapes

Theoretical collision sheet geometries, obtained with Equations 2.13 to 2.17, and collision sheet images are depicted in Figure 4.2, for like collisions of jets of water, liquid hydrous ethanol and gelled hydrous ethanol, with impingement angles of $2\theta = 90^\circ$ and pre-impingement jet length of 10 mm. In the case of gelled hydrous ethanol, non-dimensional numbers were based on a power-law fluid model and the gel surface tension was assumed equal to the liquid phase surface tension.

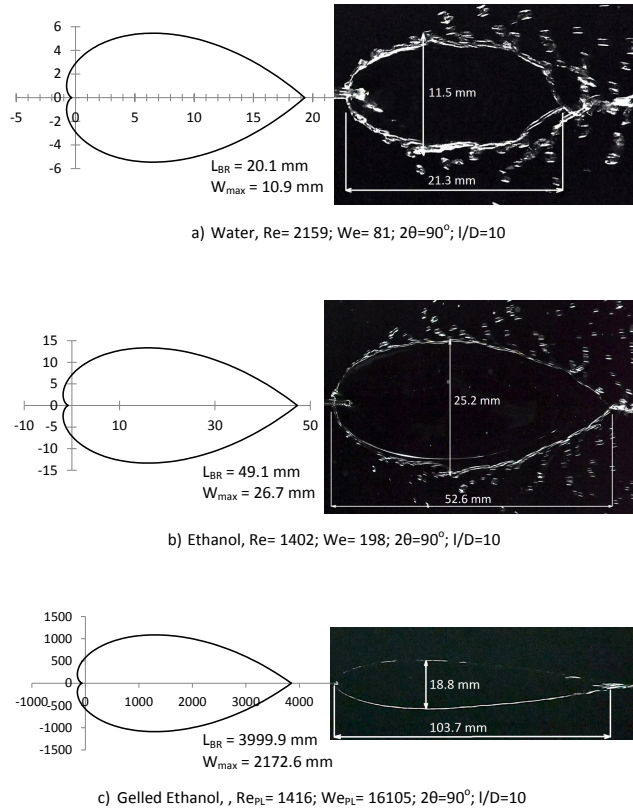
Water and liquid ethanol showed formation of droplets (beads) along the sheet edges, differently from gelled hydrous ethanol. Liquid ethanol formed a collision sheet with larger width and larger length than water, whereas as gelled hydrous ethanol formed a significantly longer collision sheet than both liquids.

The analytical solution of Ibrahim and Przekwas (1991) was effective to describe collision sheet sizes of the liquids tested, as shown in Figs. 4.2a and 4.2b. For gelled hydrous ethanol the analytical model predicts a much larger sheet shape than found experimentally. This is related to the high generalized Weber number calculated for Figure 4.2c, which affects proportionally the sheet shape.

Li and Ashgriz (2006) argued that there are two major types of instability that

can cause the sheet breakup: aerodynamic waves and impact waves. Mainly about the aerodynamic waves, they listed two regimes of instability: capillary (closed-rim sheet) and Kelvin-Helmholtz instabilities.

Figure 4.2 - Theoretical and experimental collision sheets.



SOURCE: Dias et al. (2019b).

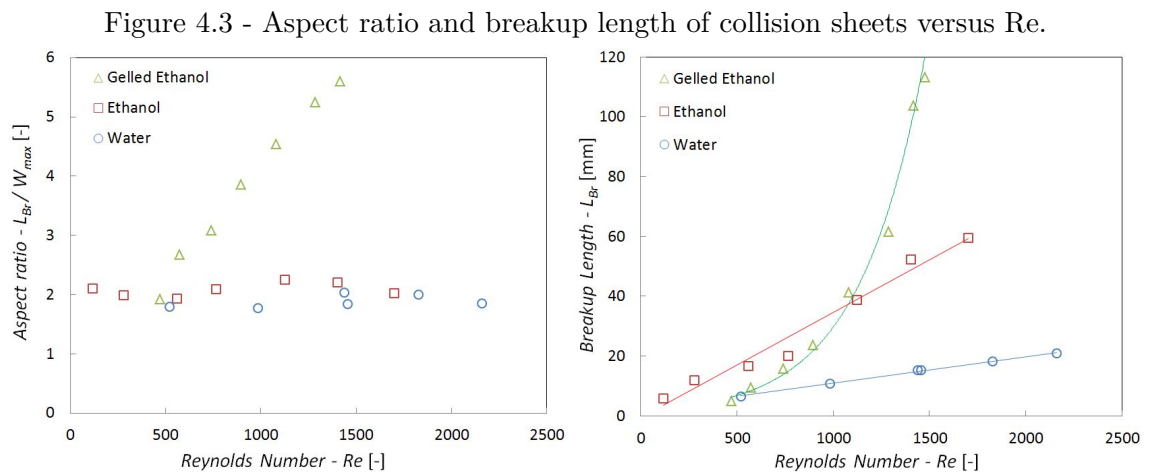
Figures 4.2a and 4.2b indicate the occurrence of a sub-regime of capillary instability classified as smooth sheet, where disturbances on the edges cause the local momentum force to be greater than the local surface tension force. These disturbances generate bead-like shapes, which keep growing while moving along the edge. After growing, the beads form drops attached to the sheet edges by ligaments. The ligaments then disintegrate into smaller droplets after separation from the sheet (LI; ASHGRIZ, 2006).

The lateral momentum of the gelled ethanol sheet (Figure 4.2c) is relatively low for

a given jet momentum, so the sheet converges to a point. The inertial force is lower than viscous force and surface tension at the point of the maximum sheet width, and consequently the sheet is restrained and begins to converge (DENG et al., 2018).

Figure 4.3 shows aspect ratio (L_{Br}/W_{max}) and breakup length versus Reynolds number, for the closed-rim sheet regime. Measurements were made with help of an image processing software developed by Vasquez (2011).

Figure 4.3a shows that sheet shapes of liquid water jets and liquid hydrous ethanol jets have aspect ratios nearly constant, around 2, in the range of Reynolds number considered. This value is close to 2.1, found by Baek (2011) using liquid water impinging jets, with $2\theta = 90^\circ$ and $D = 0.7$ mm. For gelled hydrous ethanol, Figure 4.3a shows that the aspect ratio increases approximately linearly with the Reynolds number, and the sheet tends to stretch until breakup.

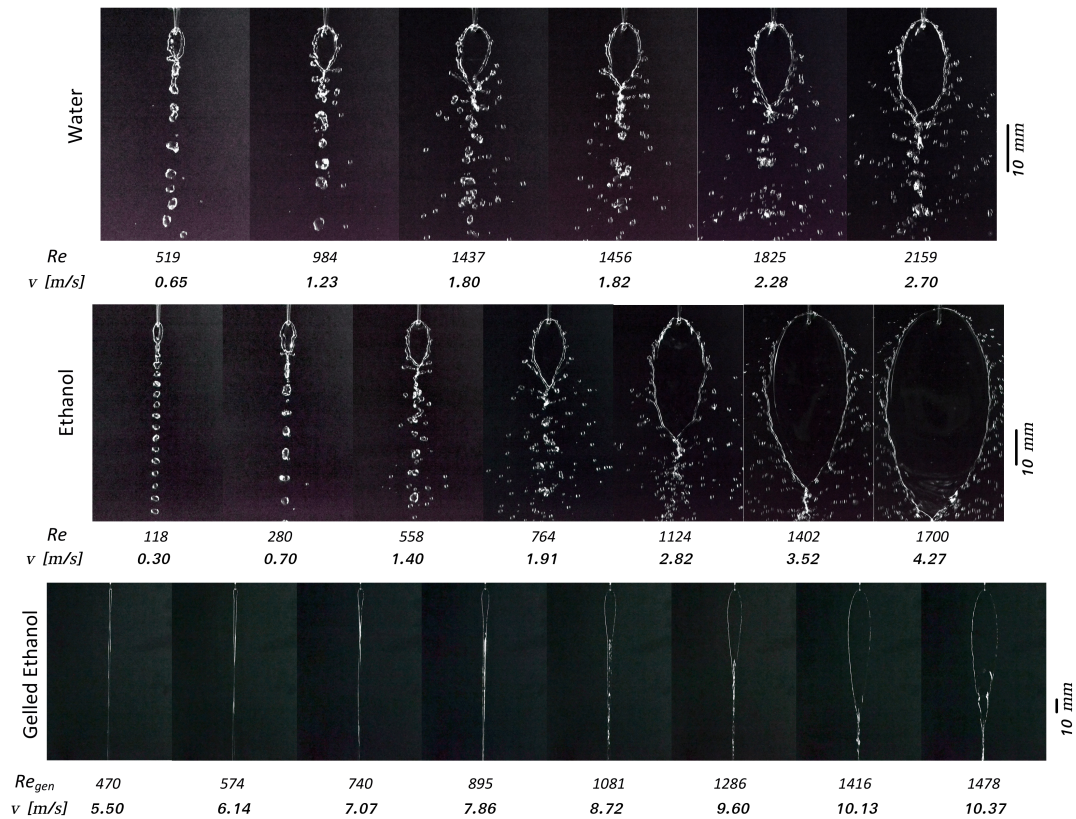


SOURCE: Dias et al. (2019b).

Figure 4.3b indicates a linear increase of the breakup length of water and liquid hydrated ethanol and an exponential increase of the breakup length of gelled ethanol for increasing Reynolds numbers. This exponential behavior of the non-Newtonian sheet is probably due to the damping effect of viscosity which varies with shear rate along the sheet.

Figure 4.4 shows the closed-rim sheet and their shape evolution with increasing jet Reynolds numbers and jet velocities.

Figure 4.4 - Sheet shapes increasing Reynolds



SOURCE: Author.

4.3 Atomization of liquid water and liquid hydrous ethanol, like and unlike impingement

This section presents data on water and liquid hydrous ethanol atomization for like and unlike jet collisions.

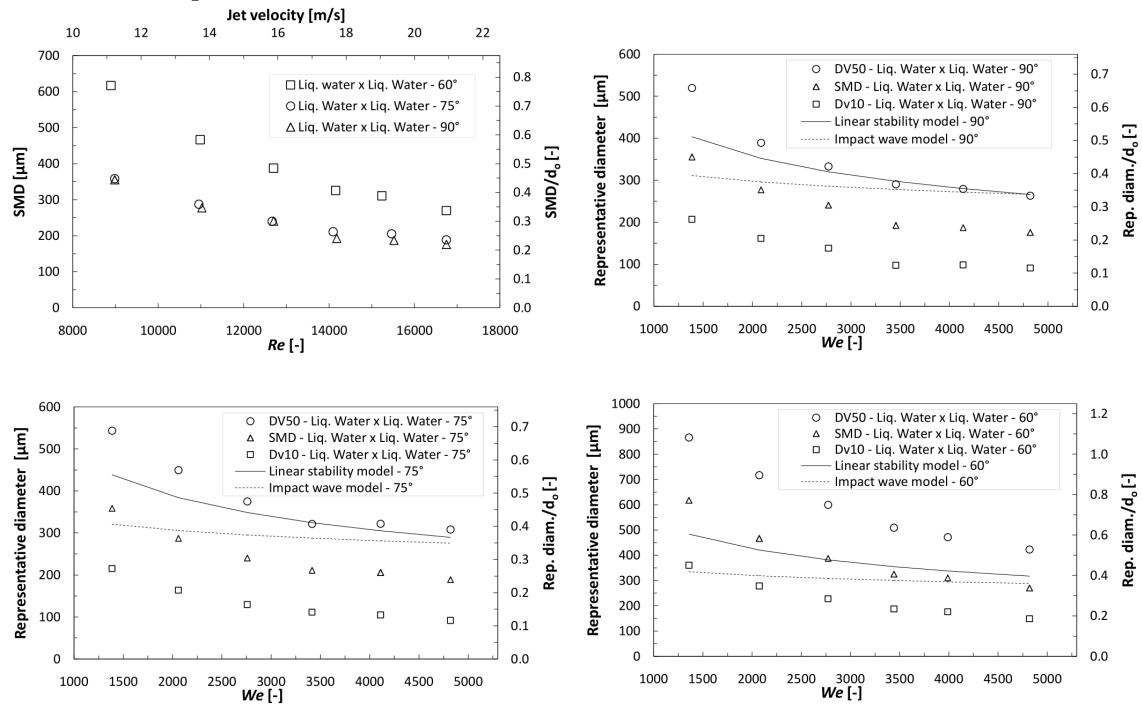
4.3.1 Liquid water - like impingement

Liquid water is probably the most studied working fluid in atomization processes, therefore experimental data of representative diameters of droplets obtained by impinging jets of liquid water are easily found in the literature. However most of the experimental data available correlate few variables, such as jet velocity and impingement angle (DOMBROWSKI; HOOPER, 1964), surface tension, jet velocity, fluid density and air ambient density (DOMBROWSKI; HOOPER, 1962), surface tension, jet velocity, fluid density, air ambient density and orifice diameter (TANASAWA et al., 1957).

Figure 4.5 shows representative droplet diameters for sprays formed by like impingement of liquid water jets in a range of jet Reynolds numbers and impingement angles θ . Experimental values were obtained by the Spraytec laser diffraction system, while theoretical diameter values were calculated using the linear stability model (Equation 2.32 with empirical breakup constant of 12) and the impact wave model (Equation 2.34).

As seen in Figure 4.5, the experimental and theoretical representative diameters of sprays generated by like impingement of liquid water jets decrease with increase in θ , Re and We , as expected.

Figure 4.5 - Liquid water x liquid water, like impingement – experimental and theoretical representative diameters.



SOURCE: Author.

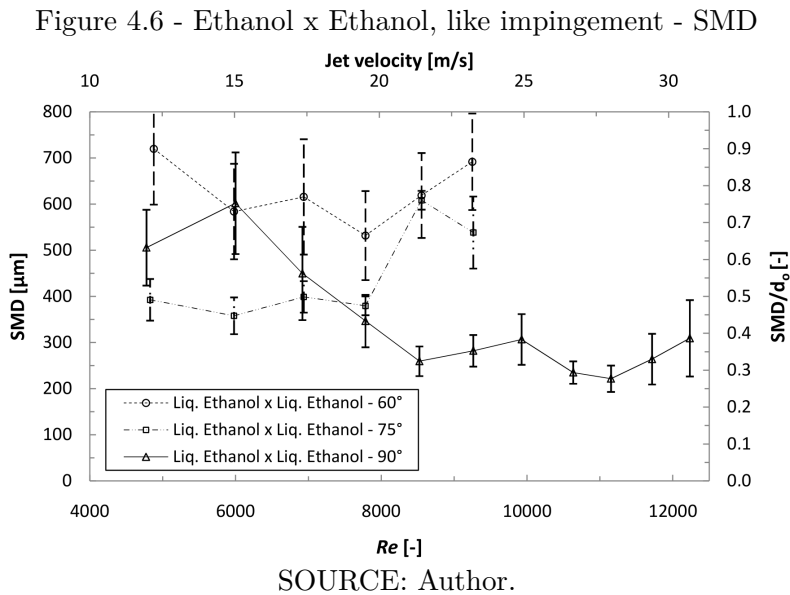
Both theoretical models failed to reproduce exactly the experimental data. The impact wave model should be compared to SMD while the stability-based model is probably related to the linear diameter D_{10} (not D_{v10}).

The standard deviations of water droplet diameters were relatively small, conse-

quently they were not plotted. The maximum standard deviation was 19.49 for the higher SMD at 60° and minimum standard deviation was 2.21 for the lower SMD at 90° .

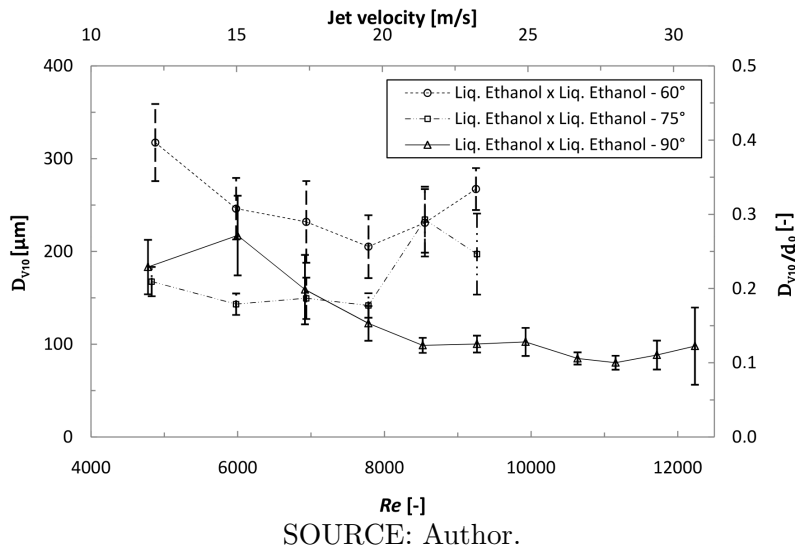
4.3.2 Liquid hydrous ethanol - like impingement

In the case of two impinging jets of liquid hydrous ethanol, a different scenario from that found for water is observed. Representative diameters of droplets of liquid ethanol are shown in Figs. 4.6 and 4.7 for different Re or jet velocities and collision angle. Plots indicate no regular trend of increase or decrease of representative diameters with Re and collision angle. A similar behavior is verified if data were plotted against We . The standard deviations of representative diameters of liquid ethanol are significantly larger than for water.



Large SMD and Dv_{10} standard deviation together with an unclear trend in decrease of representative diameters with increase in Re and 2θ were found.

Figure 4.7 - Ethanol x Ethanol, like impingement - D_{10}



For better understand about the differences between water and ethanol like impingement with respect to spray representative diameters, an investigation was done, as follow.

4.3.3 Droplet size distributions

Figure 4.8 shows the droplet size distributions of liquid water (upper plots) and liquid ethanol (bottom plots) sprays, obtained by the laser diffraction system, in terms of volume frequency and number frequency. Cumulative volumes and cumulative numbers are indicated by the red lines in the plots.

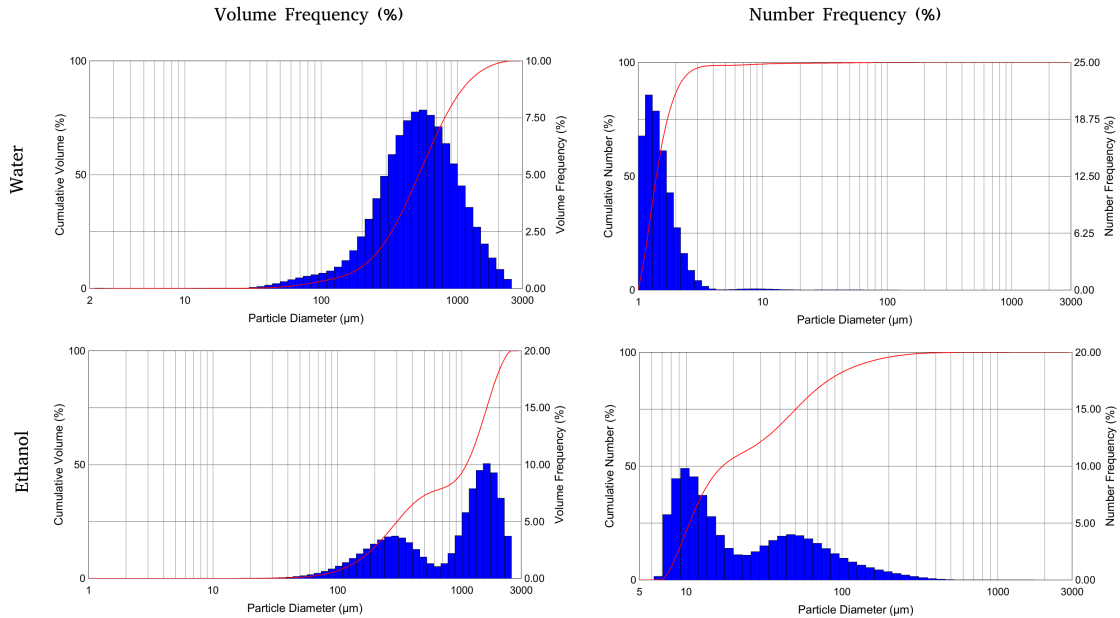
Figure 4.9 shows a table of volume frequency and cumulative volume data of water, which was used to generate the upper plots in Figure 4.8.

The volume frequency curve shows the percentage of the spray volume for a given range of droplet diameters. For example, in the case of liquid water, drops between 500 and 600 micrometers comprise the largest amount of the spray volume, just over 7.5% of the total spray volume.

On the other hand, the number frequency curve shows the percentage of the total number of droplets in the spray for a given range of droplet diameters. Water droplets with diameters between 1 and 4 μm comprise almost 88% of the total number of spray droplets, as seen in the number frequency plot. However these droplets

contribute with a very small portion of the spray volume, as seen in the cumulative volume curve, since the droplet volume varies with the cube of droplet diameter.

Figure 4.8 - Liquid water and liquid ethanol droplet size distribution by volume and number frequency, $2\theta = 75^\circ$ and Injection pressure = 1 bar



SOURCE: Author.

The recorded data for liquid ethanol were different from that of liquid water. It is important to report that the plots in Figure 4.8 represent data for one second measurements in continuous mode (continuous sprays, not pulsed ones). The distribution curves of liquid water droplets were stable for all measurements, with only small differences between recordings (each 1 second), differently for liquid ethanol. Although the liquid ethanol curves presented in Figure 4.8 had most commonly a bimodal shape, sometimes they presented a Gaussian shape similar to water sprays for number frequency, but maintained the same bimodal shape for volume frequency, indicating that the particle size distributions of liquid ethanol sprays were not stable from measurement to measurement, even when no operational parameter was changed. This also explains the large SMD standard deviation of liquid ethanol compared to water.

Bi-modal distributions were present in both liquid water and liquid ethanol plots of

number frequency distributions, but were much more common for liquid ethanol.

Figure 4.9 - Volume frequency and cumulative volume data for liquid water.

Size (μm)	% V <	% V	Size (μm)	% V <	% V	Size (μm)	% V <	% V
1.14	0.00	0.00	15.46	0.08	0.01	209.85	10.55	2.27
1.30	0.00	0.00	17.62	0.10	0.01	239.08	13.60	3.05
1.48	0.00	0.00	20.07	0.11	0.01	272.38	17.55	3.96
1.68	0.00	0.00	22.86	0.11	0.01	310.32	22.48	4.93
1.92	0.00	0.00	26.05	0.13	0.01	353.54	28.37	5.89
2.19	0.00	0.00	29.68	0.15	0.03	402.79	35.10	6.73
2.49	0.02	0.02	33.81	0.20	0.05	458.89	42.48	7.38
2.84	0.03	0.01	38.52	0.29	0.09	522.80	50.24	7.76
3.23	0.03	0.00	43.89	0.44	0.15	595.62	58.08	7.84
3.68	0.03	0.00	50.00	0.66	0.22	678.58	65.70	7.62
4.20	0.03	0.00	56.96	0.97	0.30	773.10	72.81	7.11
4.78	0.03	0.00	64.90	1.36	0.39	880.78	79.18	6.37
5.45	0.03	0.00	73.94	1.83	0.47	1003.46	84.66	5.48
6.21	0.03	0.00	84.23	2.37	0.54	1143.22	89.18	4.52
7.07	0.03	0.00	95.97	2.97	0.61	1302.46	92.74	3.57
8.06	0.04	0.00	109.33	3.65	0.67	1483.87	95.44	2.70
9.18	0.04	0.01	124.56	4.43	0.78	1690.55	97.40	1.96
10.46	0.05	0.01	141.91	5.37	0.95	1926.01	98.75	1.35
11.91	0.06	0.01	161.68	6.61	1.23	2194.28	99.59	0.84
13.57	0.07	0.01	184.20	8.27	1.67	2499.90	100.00	0.41

SOURCE: Author.

Sometimes the droplet size distributions can be multi-modal (PANÃO; MOREIRA, 2010)(SMYTH; HICKEY, 2003). Multi-modal distributions do not refer to any measurement errors, but come from the physical nature of the fragmentation process that have the simultaneous presences of primary, secondary and sometimes tertiary droplets (PANÃO; MOREIRA, 2010).

In fact, some attempts were made in this work to eliminate the multi-modality of sprays formed by collisions of liquid hydrous ethanol jets, such as: increase of distance of measurement from impingement point, in order to measure a most developed spray region; removal of the anti-fog apparatus to eliminate possible bouncing droplets on its walls; using a device to avoid droplets agglomerated by fog from falling into the spray area. In all cases the bi or multi modal curve was still present.

The technical note NASA D-872 reports that in all tested cases, the droplet size distributions from a spray of two round liquid impinging jets of water were bi-modal (HEIDMANN; FOSTER, 1961). Multi-modality of droplet size distributions is observed on Emekwuru and Watkins works (EMEKWURU, 2012)(EMEKWURU; WATKINS, 2010).

According to multi-modality and the unstable behavior of ethanol spray with respect to droplet size distribution, a brief investigation was done, as showed next.

4.3.3.1 Coalescence and secondary breakup - brief analysis

Coalescence and secondary breakup may occur under specific conditions, as mentioned in the methodology section.

The probability of binary collision was not calculated in this work. The diffraction laser system determined volume concentrations of 124 to 184 ppm for liquid hydrous ethanol and from 73 to 80 ppm for water, with injection pressure of 1 bar and $2\theta = 75^\circ$ (same setup of Figure 4.8). Since the liquid hydrous ethanol spray is denser than the water spray, binary collisions in the liquid ethanol spray are more probable.

Equations 2.36 to 2.41 were used to simulate a coalescence outcome of a possible binary collision in both water and liquid hydrous ethanol sprays.

Table 4.1 shows coalescence data of water droplets, for different relative jet velocities, diameters of large (dl) and small (ds) droplets and a fixed collision angle $2\theta = 30^\circ$.

For secondary breakup analysis the particle was assumed to be 80% of the jet velocity due deceleration after the impingement. The lowest We value for droplet breakup is 12, corresponding to the called "bag breakup". Table 4.2 shows jet velocities considering injection pressures used during atomization tests, particle velocities and particle diameters when $We = 12$, in other words, the minimum value of droplet diameter for bag breakup take place.

Table 4.1 - Coalescence analysis for liquid water and liquid hydrous ethanol.

V. relative [m/s]	Water dl=ds=100 μm	Ethanol	Water dl=100;ds=50 μm	Ethanol	Water dl=100;ds=25 μm	Ethanol	Water dl=100;ds=12,5 μm	Ethanol
11.25	-	-	-	-	coalesce	-	coalesce	coalesce
5.63	-	-	coalesce	-	coalesce	coalesce	coalesce	coalesce
3.75	coalesce	-	coalesce	coalesce	coalesce	coalesce	coalesce	coalesce
2.81	coalesce	-	coalesce	coalesce	coalesce	coalesce	coalesce	coalesce
2.25	coalesce	coalesce	coalesce	coalesce	coalesce	coalesce	coalesce	coalesce
1.87	coalesce	coalesce	coalesce	coalesce	coalesce	coalesce	coalesce	coalesce

SOURCE: Author.

Table 4.2 - Secondary atomization analysis for liquid water and liquid hydrous ethanol.

P [bar]	Water	Ethanol	Water	Ethanol	Water	Ethanol
	$V_{jet}[m/s]$		$V_{part} = 0.8V_{jet}[m/s]$		Diameter [μm] when $We=12$	
1,0	11.25	12.12	9,00	9.69	8811	2397
1.5	13.71	14.41	10.97	11.53	5933	1695
2,0	15.87	17.37	12.70	13.90	4428	1167
2.5	17.72	19.5	14.18	15.60	3552	926
3,0	19.4	21.44	15.52	17.15	2963	766
3.5	20.94	23.22	16.75	18.58	2543	653

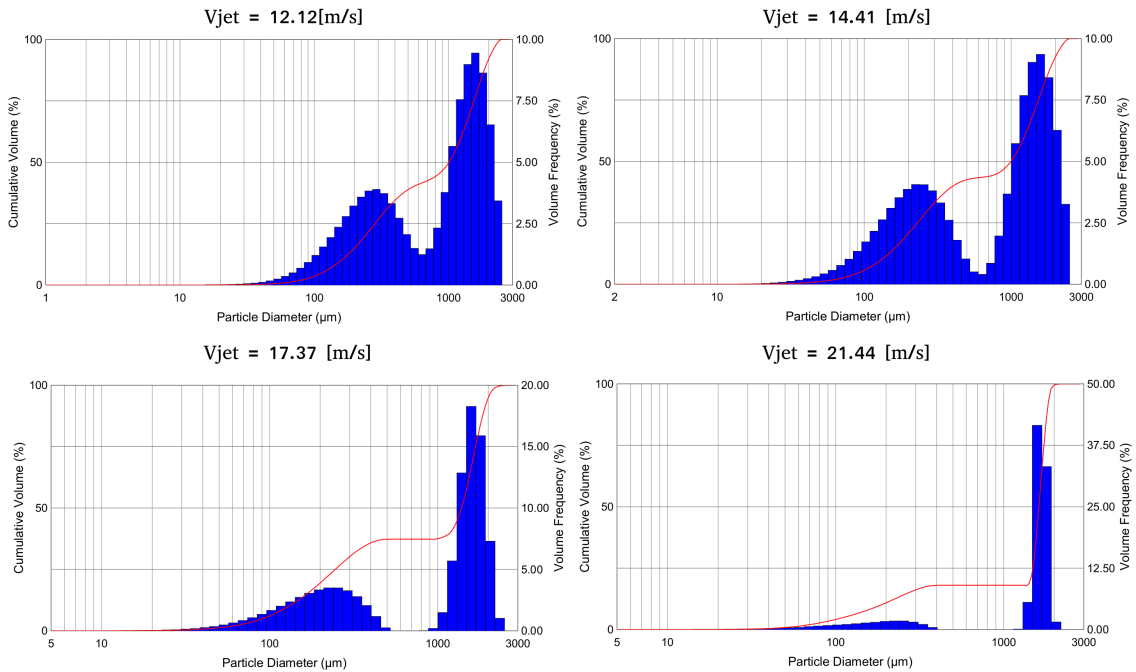
SOURCE: Author.

As liquid hydrous ethanol has lower surface tension and higher jet velocities than water for a certain injection pressure, the minimal required droplet diameter for bag breakup of ethanol is almost 4 times lower than for water droplets. Analyzing the case of Figure 4.8 (P=1 [bar] $2\theta = 75^\circ$) and comparing with data on Table 4.2 it is possible to estimate that secondary breakup is not taking place in the water spray, once it seems to have no particles with diameter of 8811 μm , and if it does, it is out of Spraytec range, 2500 μm maximum, and it would be a very rare event, taking into account the almost Gaussian and very stable curve during experiments. On the other hand, bag breakup for ethanol spray is likely since there are a few particles of 2397 μm .

Figure 4.10 shows a trend of detachment of droplet populations when jet velocity increased. This phenomenon may be an indication of secondary atomization, although the population of larger droplets tends to increase in volume frequency. Such complex droplet size distribution may occur as a result of both secondary atomization together with coalescence.

These mechanisms may produce large standard deviations on *SMD*. Droplet size measurements were also performed at larges distances downstream the impingement point and showed similar behavior.

Figure 4.10 - Droplet size volume distribution with increasing jet velocity - Ethanol



SOURCE: Author.

4.3.4 Liquid water x liquid hydrous ethanol - unlike impingement

After like impingement tests of liquid water and liquid ethanol jets, unlike impingement tests were performed. For unlike impingement, instead of Re the jet momentum mv was adopted, since both fluid jets should have the same jet momentum to generate a vertical collision sheet, perpendicular to the plane formed by the two jets, or resulting in $\xi = 0^\circ$ in Equation 2.18.

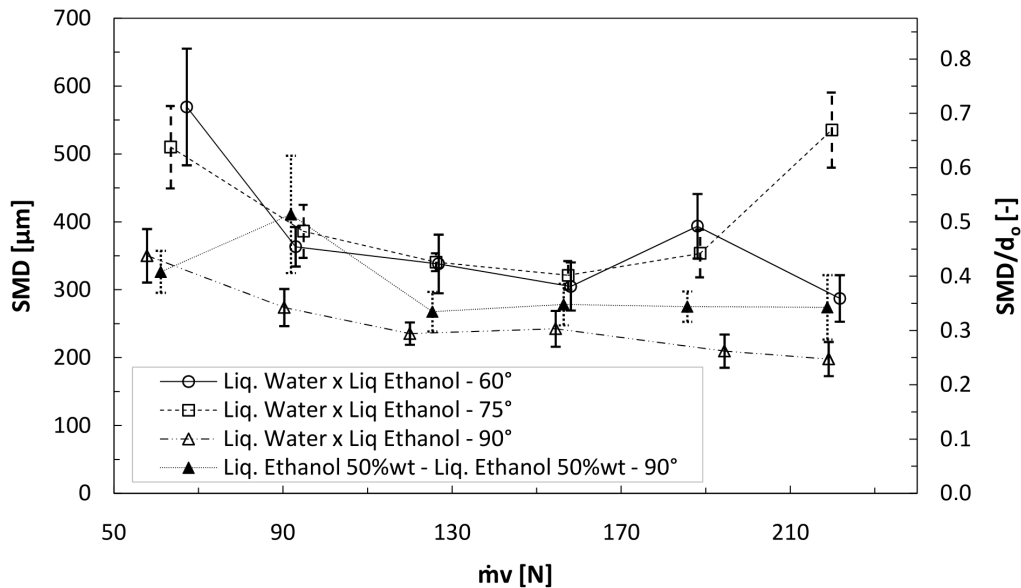
Figure 4.11 shows SMD values for liquid water x liquid ethanol unlike jets impingement and SMD values for a mixture of liquid hydrous ethanol and liquid water 50% w/w like jets impingement.

Figure 4.11 shows that SMD data of unlike colliding jets of liquid water and liquid ethanol for collision angles $2\theta = 60^\circ$ and $2\theta = 75^\circ$ do not follow a clear trend with increasing jet momenta, however for $2\theta = 90^\circ$ there is a continuous decrease of SMD for increasing jet momentum values. The SMD values for unlike jet impingement of liquid water and liquid ethanol at collision angle of 90° are, in most cases, lower than SMD values for like impingement of the 50% w/w ethanol/water mixture with the

same collision angle. Therefore unlike jets seem to promote better atomization, once it presents lower SMD values and a clear decreasing trend in SMD with increase of injection pressure.

The larger is the collision angle, larger is the quantity of mixed propellant flowing back toward the injector face, called backsplash (GILL; NURICK, 1976). When using like impinging, backsplash is not as serious a problem. To avoid backsplash the most common collision angle is 60° (GILL; NURICK, 1976).

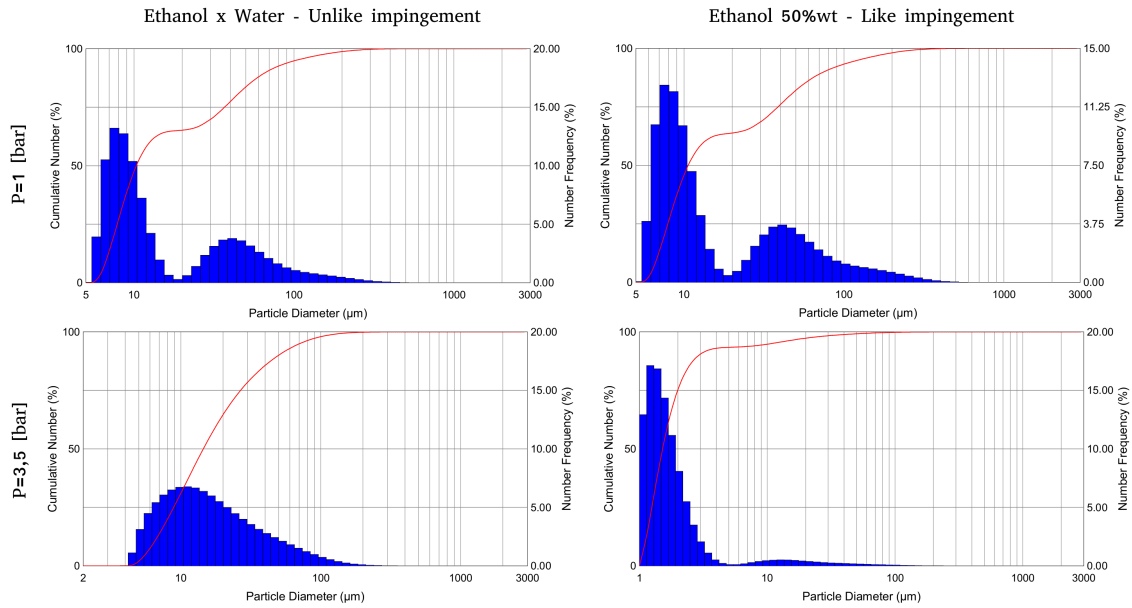
Figure 4.11 - Liquid water x liquid hydrous ethanol unlike jets impingement and liquid ethanol/liquid water 50% w/w like jets impingement – SMD



SOURCE: Author.

Figure 4.12 shows droplet size distributions based on unlike jets impingement of liquid ethanol and liquid water and droplet size distributions of like jets impingement of liquid hydrous ethanol/liquid water mixtures 50% w/w, based on number frequencies, for injection pressures of 1 and 3.5 bar. There are significant differences of droplet size distributions for like and unlike jets with injection pressure of 3.5 bar.

Figure 4.12 - Droplet size distributions of unlike colliding jets of liquid hydrous ethanol x liquid water and like colliding jets of liquid hydrous ethanol/liquid water mixtures 50% w/w, for a collision angle of $2\theta=90^\circ$

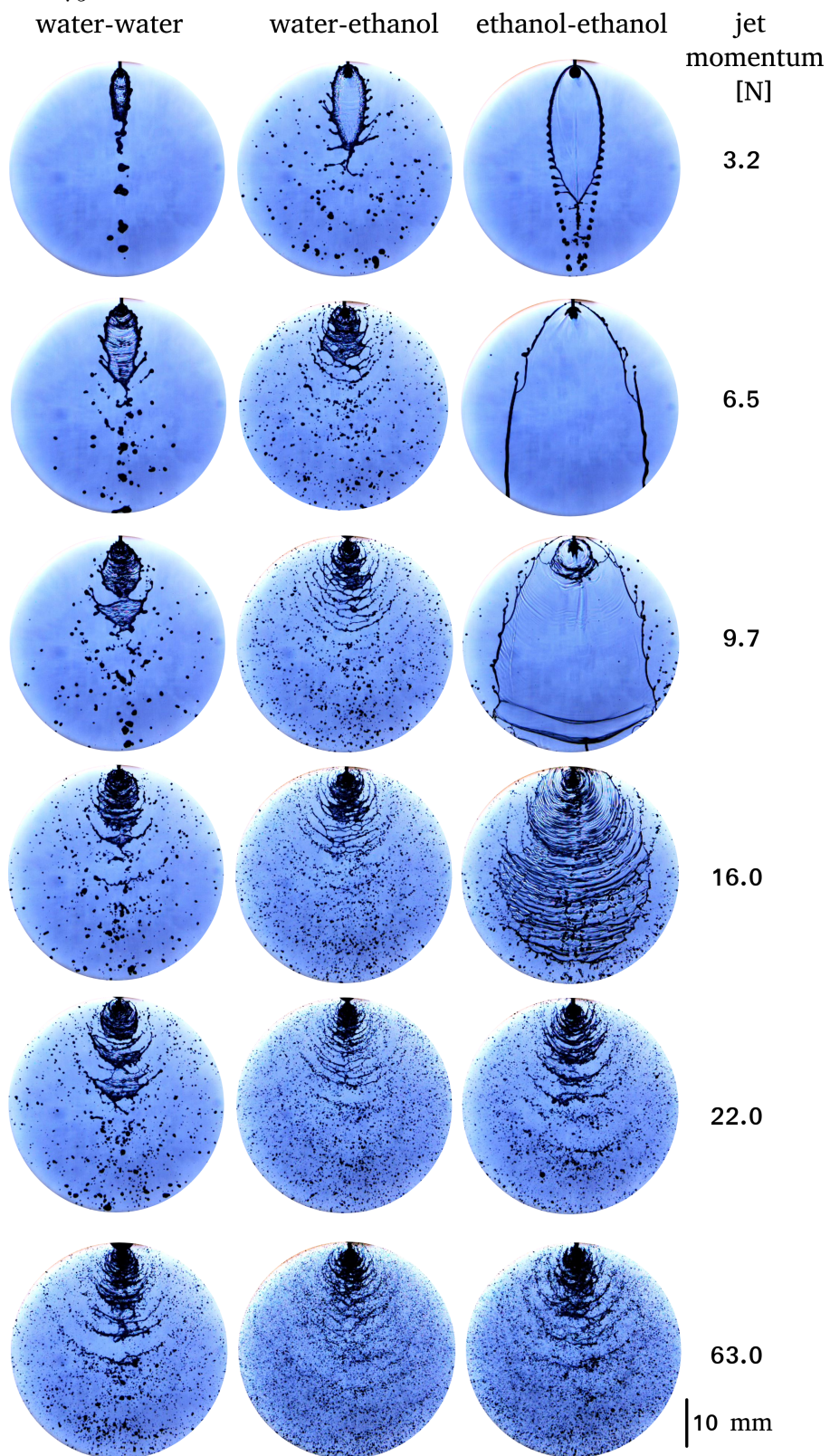


SOURCE: Author.

Figure 4.13 shows a comparison between liquid water/liquid hydrous ethanol like/unlike impingement, for a range of jet momentum. In this figure, the collision sheet of jets of the liquid hydrous ethanol/water mixture is not presented. The regimes goes from closed rim to fully developed regime. Viscosity and surface tension have great influence on flow patterns generated by like and unlike doublet impinging jets (LAI; WANG, 2002). It is remarkable that the presence of water decreases the breakup length of the liquid ethanol sheet, as seen for jet momentum of 3.2 N. This can be caused by formation of a mixture of ethanol and water in the collision sheet with corresponding changes in surface tension and viscosity, since they are soluble fluids, and/or by formation of a thin shear layer due to the presence of two different fluids with different velocities, despite equal jet momenta.

A fully developed regime is reached in unlike impingement with a lower jet momentum due to the shorter wavelength of the most unstable disturbance. This shorter wavelength can be clearly noted in the images for jet momentum of 22 N in Figure 4.13.

Figure 4.13 - Liquid hydrous ethanol and liquid water - like and unlike impingement, $2\theta = 75^\circ$



SOURCE: Author.

4.3.4.1 Spray pattern and mixing

In order to verify the spray mass flux distribution and the mixing characteristics for like and unlike impingement jets, a patternator with 91 cells was used, as described on Chapter 2. The mass flux distribution was determined by collecting the fluid mass passing through each patternator cell during 10 seconds. A Python routine was developed to read a file with experimentally collected mass data and plot contour graphics.

Figures 4.14 and 4.15 show estimates of the mass flux distributions for like-impingement of liquid water jets and liquid hydrous ethanol jets, with impingement angles of 90° and pre-impingement jet distances of 8 mm. Distance from impingement point to the patternator was 70 mm.

As seen in Figs. 4.14 and 4.15, the sprays showed a narrow and elongated distribution along the y-direction, in the plane of the collision sheet, with the largest mass fluxes in the central region. Water droplets reached farther distances from origin than ethanol droplets.

Injection pressures were 2.45 bar for water and 1.95 bar for liquid ethanol. Although these injection pressures were different, the velocities of both fluids were similar, 17.14 m/s for water and 17.55 m/s for ethanol. However water jets presented thrusts (momenta) and mass flow rates larger than ethanol jets. Total mass flow rates are the sum of the mass flow rates of each colliding jet.

Figure 4.14 - Mass flux distribution estimate for like jet impingement of liquid water. $\dot{m}_{tot}=17.58$ g/s, $F=154.31$ N, $u_j = 17.14$ m/s

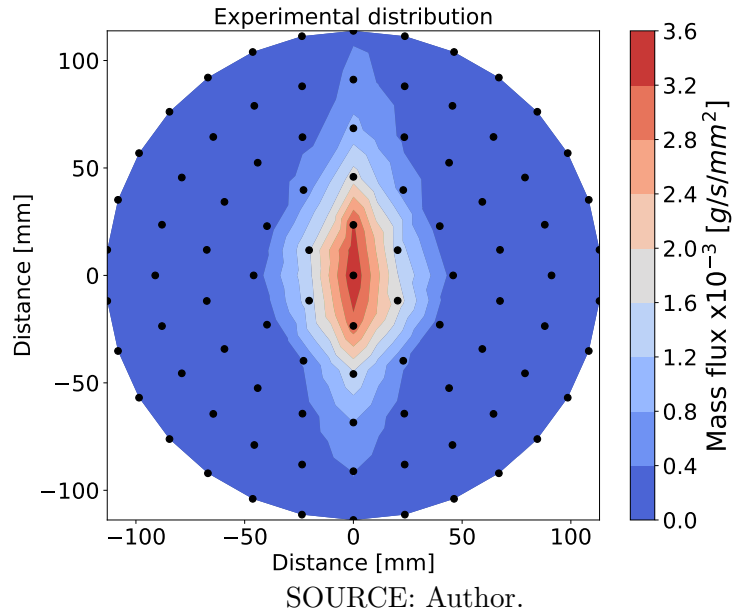
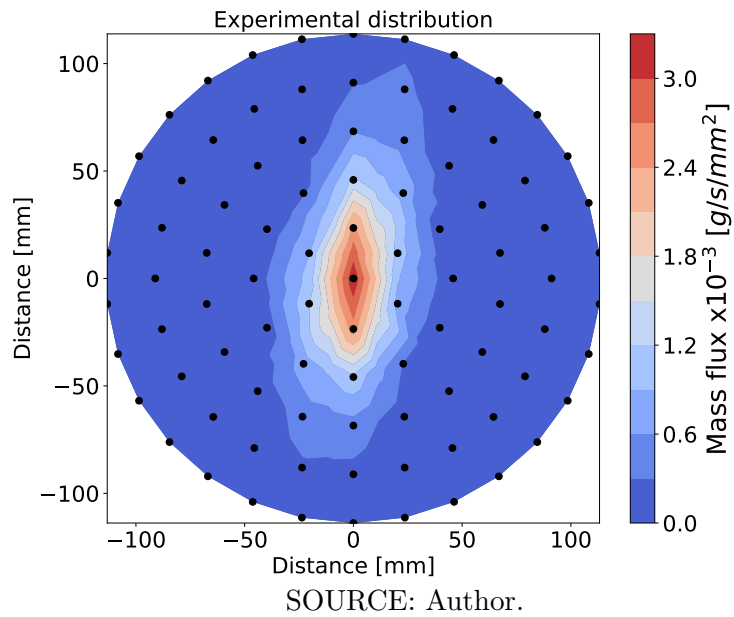


Figure 4.15 - Mass flux distribution estimate for like jet impingement of liquid hydrous ethanol. $\dot{m}_{tot}=13.92$ g/s, $F=119.36$ N, $u_j = 17.55$ m/s



Experimental results for unlike impingement of liquid water and liquid hydrous ethanol jets are shown in Figs. 4.16 to 4.19. The momenta of the two jets were kept approximately equal, such that the plan containing the collision sheet was vertical and bisected the angle formed by the jets. Impingement angle, pre-impingement distance and distance from the impingement point to patternator were the same as in the like impingement test. Ethanol was injected on the left side, considering the upper view of Figure 4.16.

Injection pressures were 1.12 bar for ethanol and 1.15 bar for water, leading to $u_j = 12.85$ m/s and thrust $F = 67.13$ N for ethanol and $u_j = 12.06$ m/s and thrust $F = 72.87$ N for water. The spray mass distribution is shown in Figure 4.16, showing a similar shape to like impingement of ethanol or water.

The mixing of ethanol and water was given in terms of volume percentage which depends on mixture density, water density and ethanol density. The volume fractions of water, f_{va} , and ethanol, f_{ve} , are obtained from

$$f_{va} = \frac{\rho - \rho_e}{\rho_a - \rho_e} \quad \text{and} \quad f_{ve} = 1 - f_{va} \quad (4.1)$$

where ρ is mixture density, ρ_e is density of liquid hydrous ethanol, and ρ_a is density of liquid water. The density of the mixture was determined by weighing samples from each patternator tube, collected by a milliliter pipette.

Equations (4.1) are derived from

$$\rho = \frac{m_a + m_e}{V} = \frac{V_a \rho_a + V_e \rho_e}{V} = f_{va} \rho_a + f_{ve} \rho_e \quad (4.2)$$

where m_a is mass of water, m_e is mass of ethanol, V is total volume, V_a is volume of water and V_e is volume of ethanol in the mixture. Consequently,

$$\rho = f_{va} \rho_a + (1 - f_{va}) \rho_e = f_{va} (\rho_a - \rho_e) + \rho_e \quad (4.3)$$

The volume percentages of water and ethanol are $\%V_{water} = 100f_{va}$ and $\%V_{ethanol} = 100f_{ve}$. Values of $\%V_{water}$ and $\%V_{ethanol}$ along the centerline of Figure 4.16 are shown in Figure 4.17 while Figs. 4.18 and 4.19 depict the mixing contourlines in terms of volume percentages.

Figure 4.16 - Mass flux distribution for unlike impingement of liquid hydrous ethanol and liquid water jets.

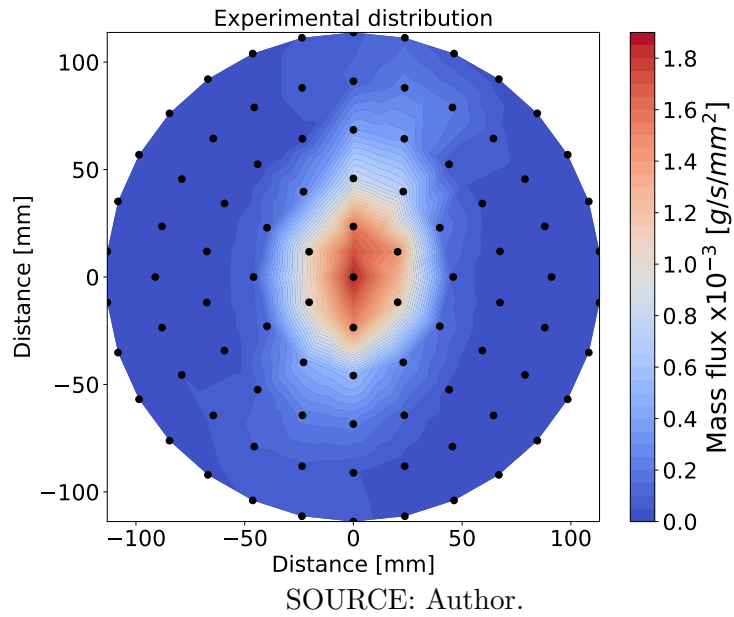


Figure 4.17 - Mixing along the vertical centerline of Figure 4.16 for unlike impingement of liquid hydrous ethanol and liquid water jets.

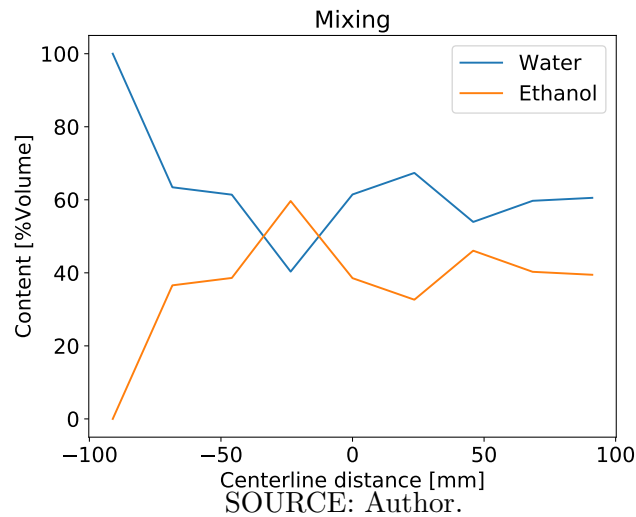


Figure 4.18 - Mixing - Ethanol

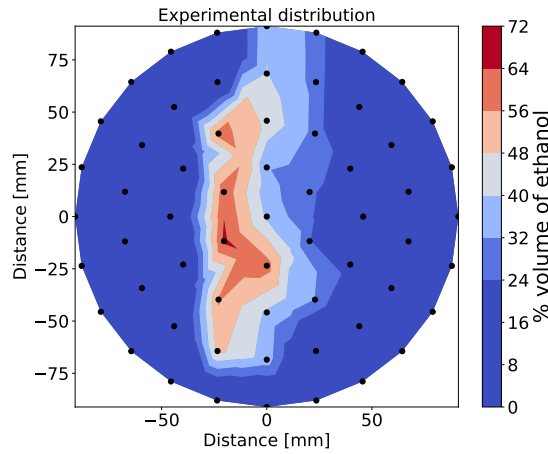
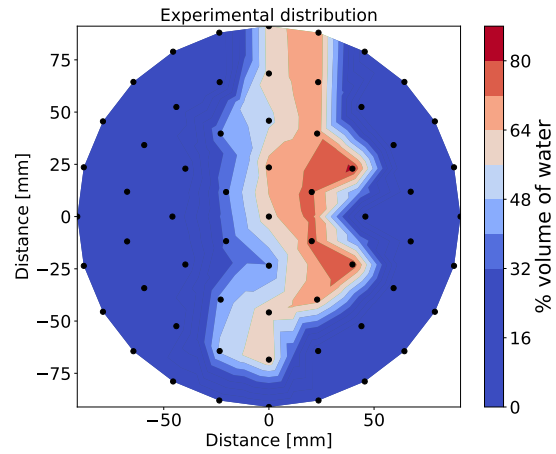


Figure 4.19 - Mixing - Water



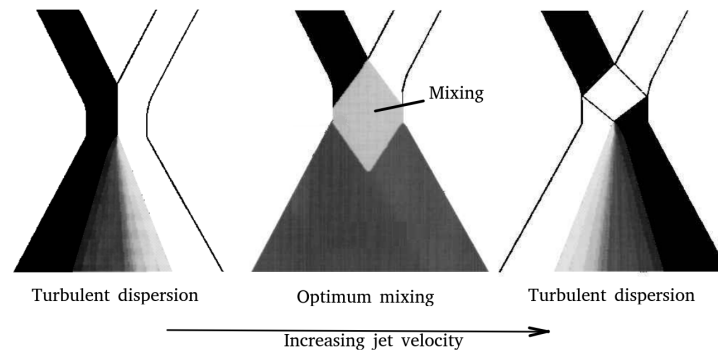
SOURCE: Author.

The momenta of the two jets are not exactly equal and there is a fluctuation of the plane containing the collision sheet due to several factors, such as misalignment of jets, turbulence and mixing, instability waves in the collision sheet which breaks up into drops, and non-symmetrical and non-regular detachment of droplets.

For low velocities, the liquid is redirected in the ξ direction and liquid from each jet remains in the same plane after atomization, this is called reflective atomization (Figure 4.20) (ASHGRIZ; BROCKLEHURST, 2001). Increasing jets velocities, the coalesced liquid jet or sheet breaks up into droplets after an even shorter time, and jets do not have time to be completely redirected. After atomization, the drops trajectories will be governed by the trajectory of the stream, which has contributed the most to the liquid in that drop. Therefore, shortly after atomization, the drops segregate, and it appears that the two jets cross through each other, called this the transmissive atomization (ASHGRIZ, 2011).

Figures 4.18 and 4.19 show a higher mass flux of ethanol on the left side (upper view) for ethanol injection in the same side. On the other hand there is also a small fraction of water on the left side and, therefore, the mixture is not completely reflective (Figure 4.20). A further increase on jet velocities may result in better atomization mixing. In between the reflective and transmissive atomization lies the optimum well mixed atomization.

Figure 4.20 - Mixing regimes



SOURCE: Adapted from Ashgriz e Brocklehurst (2001).

4.4 Atomization of gels with like and unlike impingement of jets

For gels, like and unlike impingement tests were done using gelled water and gelled hydrous ethanol. Due to their high viscosity, the injection pressures for gels reached high values, almost 18 bar, during the atomization experiments.

Figure 4.21 shows shadow front view images of the collision sheets formed by like and unlike impingement of gelled hydrous ethanol and gelled water jets with different momenta: 36, 46, 58, 63 and 126 N. Table 4.3 lists data for these tests, including $\dot{m}v$, P , v , Re , We and We_{gen} . All parameters were based on jet properties.

As seen in Figure 4.21, complex asymmetrical structures are formed inside the collision sheets of impinging jets of gelled fluids, containing ligaments and holes which increase in number with increasing jet momentum values. Impact waves in the form of approximately circular arcs are generated at the collision point and, for the largest momentum considered, 126 N, these impact waves propagate generating ligaments also of approximately circular form. A significant formation of droplets was observed only for jet momentum of 126 N.

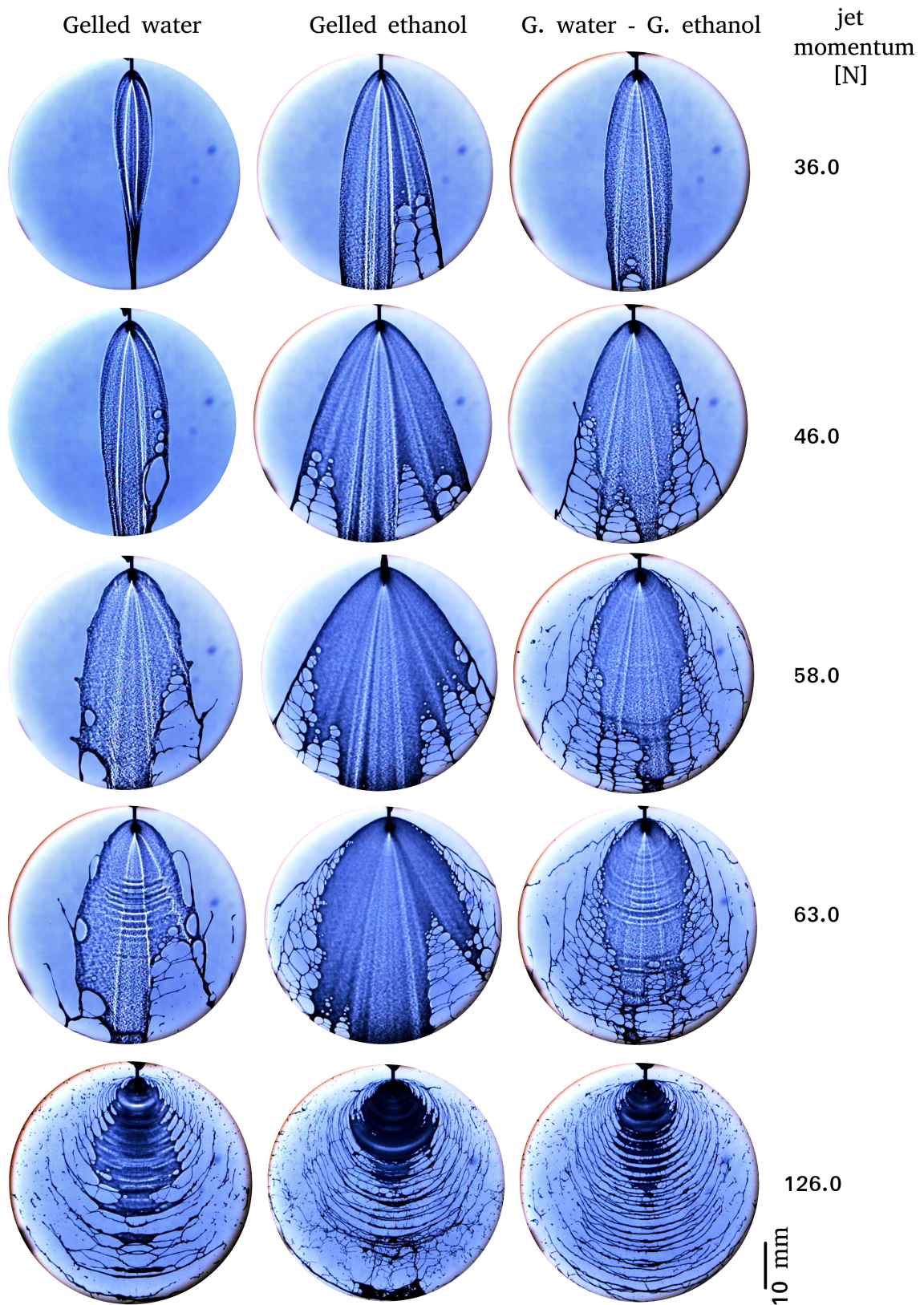
For low jet momentum values, 36 N and 46 N, like impingement of gelled water jets has formed significantly smaller sheets than like impingement of gelled hydrous ethanol and unlike impingement of gelled water and gelled hydrous ethanol.

Figure 4.22 shows front and side shadow views of the collision sheets formed by like impingement of gelled hydrous ethanol jets with collision angle 75° and different We values. Complex asymmetrical structures are formed inside the collision sheets from like impingement of gelled hydrous ethanol jets, containing ligaments and holes

which increased in number with increasing jet We values. Circular ligaments and significant formation of droplets were observed only with the largest We considered, $We = 2926$.

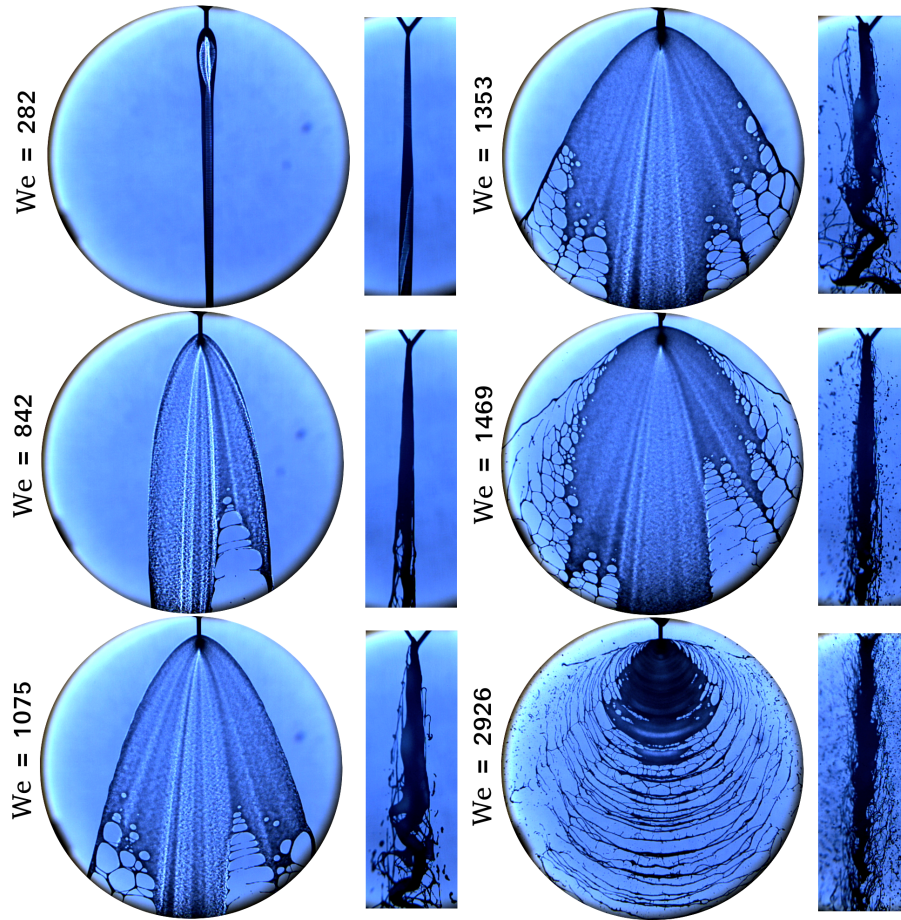
Figure 4.23 shows an impact wave starting at the impact point and spreading down to the collision sheet bottom in the like impingement of gelled hydrous ethanol jets, with jet momentum 63 N and $2\theta = 75^\circ$. As the sheet velocity increases, instabilities arise in the sheet surface as showed in Figure 4.23 for $We = 1075$ and $We = 1353$. When analyzing the pre-impact jets, no visible disturbances (section 4.1) were found for gel jets, differently from the gel collision sheet.

Figure 4.21 - Gelled water and gelled ethanol - like and unlike impingement, $2\theta = 75^\circ$



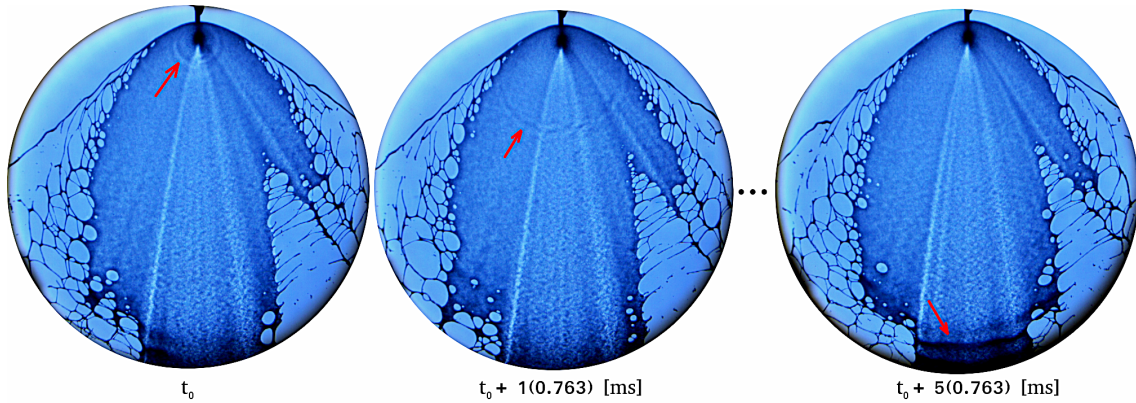
SOURCE: Author.

Figure 4.22 - Gelled Ethanol x Gelled Ethanol - Like impingement - $2\theta = 75^\circ$



SOURCE: Author.

Figure 4.23 - Impact wave starting from impingement point and propagation for like impingement of gelled hydrous ethanol jets, with jet momentum 63 N and $2\theta = 75^\circ$



SOURCE: Author.

Table 4.3 - Jet parameters for collision of jets shown in Figs. 4.13, 4.21, 4.22, 4.24, 4.27, 4.28, 4.32 and 4.33.

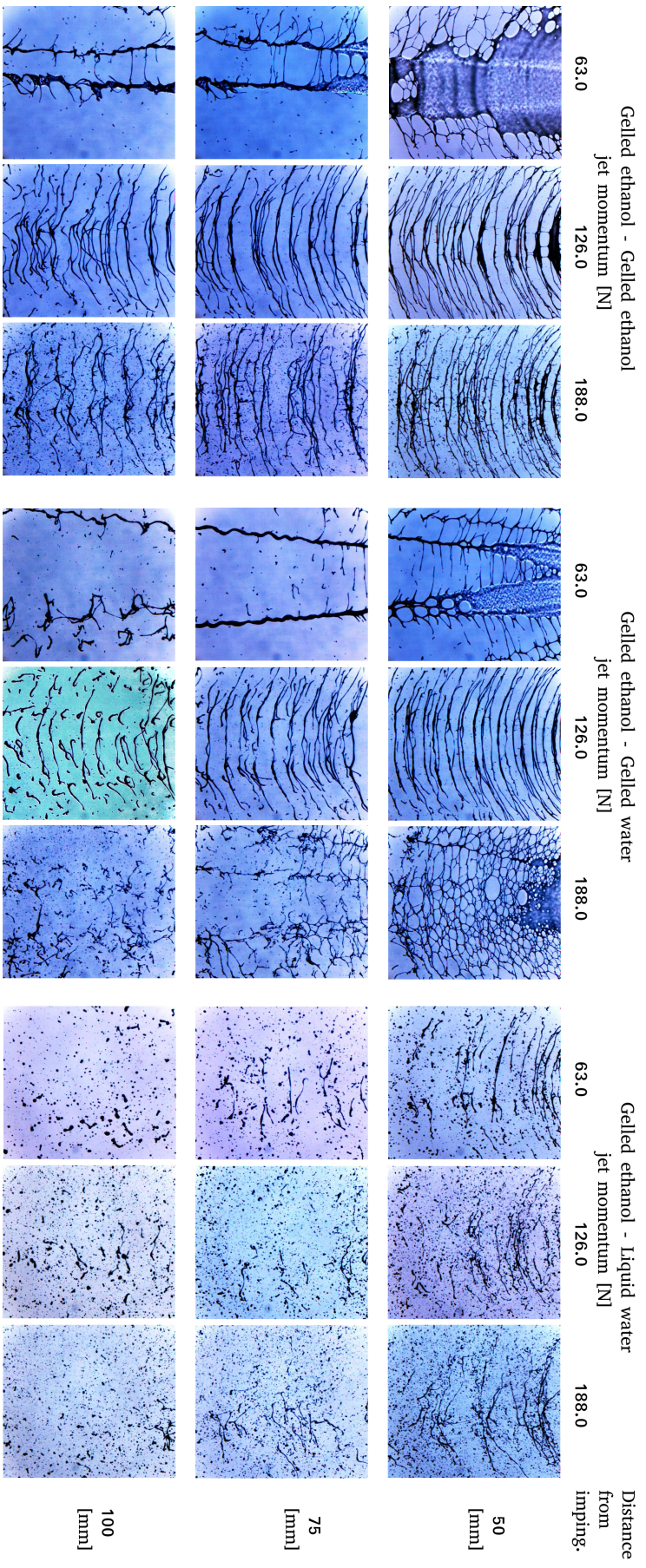
Ethanol					Gelled Ethanol				
$\dot{m}v$ [N]	P [bar]	v [m/s]	We [-]	Re [-]	P [bar]	v [m/s]	We [-]	We _{gen} [-]	Re _{gen} [-]
3.2	0.06	2.81	224.92	1120.87	1.67	2.84	78.05	428.96	143.10
6.5	0.12	4.03	461.85	1606.16	2.01	4.02	156.01	857.43	267.24
9.7	0.17	4.83	663.01	1924.41	2.26	4.87	229.42	1260.93	378.42
11.0	0.20	5.26	784.84	2093.77	2.36	5.21	262.50	1442.71	427.29
22.0	0.38	7.34	1528.02	2921.47	2.99	7.32	517.57	2844.59	788.28
31.0	0.53	8.72	2158.30	3472.11	3.40	8.66	724.71	3983.02	1067.84
36.0	0.61	9.38	2497.38	3734.91	3.61	9.34	842.65	4631.24	1223.40
46.0	0.78	10.65	3223.35	4243.18	3.99	10.55	1075.50	5911.02	1524.54
58.0	0.97	11.93	4041.87	4751.48	4.40	11.84	1353.45	7438.62	1875.77
63.0	1.05	12.43	4388.41	4950.98	4.56	12.33	1469.07	8074.09	2019.71
75.0	1.25	13.61	5259.03	5419.89	4.92	13.44	1743.19	9580.69	2356.70
126.0	2.05	17.59	8788.47	7006.39	6.27	17.41	2926.08	16081.90	3759.96
188.0	3.02	21.51	13138.93	8566.79	7.66	21.23	4353.89	23929.21	5380.80
Water					Gelled Water				
$\dot{m}v$ [N]	P [bar]	v [m/s]	We [-]	Re [-]	P [bar]	v [m/s]	We [-]	We _{gen} [-]	Re _{gen} [-]
3.2	0.05	2.55	71.04	2032.97	-	-	-	-	-
6.5	0.10	3.59	141.29	2867.10	3.49	3.82	156.87	829.64	136.47
9.7	0.15	4.39	211.25	3505.77	3.89	5.00	268.94	1422.31	220.50
11.0	0.17	4.67	239.18	3730.31	4.02	5.38	311.18	1645.72	251.07
22.0	0.34	6.59	475.71	5260.85	4.75	7.46	597.44	3159.62	448.65
31.0	0.49	7.90	683.59	6306.38	5.19	8.67	806.92	4267.45	586.25
36.0	0.56	8.44	780.41	6738.20	5.41	9.26	921.10	4871.33	659.54
46.0	0.72	9.56	1001.37	7632.72	5.80	10.29	1137.83	6017.52	796.00
58.0	0.91	10.74	1263.25	8572.89	6.21	11.35	1383.87	7318.91	947.51
63.0	0.99	11.19	1373.38	8938.77	6.38	11.78	1490.93	7884.91	1012.47
75.0	1.25	12.57	1730.83	10034.83	6.75	12.70	1733.31	9166.78	1157.73
126.0	2.00	15.87	2758.93	12669.33	8.13	15.95	2731.04	14443.35	1735.16
188.0	2.99	19.37	4111.35	15465.91	9.61	19.08	3910.60	20681.58	2388.38

SOURCE: Author.

Figure 4.24 shows shadow images of regions located 50, 75 and 100 mm below the impingement point (areas of $34 \times 38 \text{ mm}^2$) for jet impingement of gelled ethanol \times gelled ethanol, gelled ethanol \times gelled water and gelled ethanol \times liquid water with different jet momenta. Jet parameters are in Table 4.3. Comparing like to unlike impingement, as happened for liquids, gelled fluids also showed an improvement when performing unlike impingement, verified by the earlier fragmentation of ligaments.

Figure 4.25 shows SMD and Dv_{10} for like gelled ethanol jet impinging versus Re_{gen} . The presence of ligaments and droplets for like impingement of gelled ethanol was already noticed at the measurement distance of 50 mm (Figure 4.24). For $2\theta = 60^\circ$ there was spray formation only around $Re_{gen} = 9500$ with a continuous decrease of SMD and Dv_{10} for increasing Re_{gen} . For $2\theta = 75^\circ$ as a minimum SMD and Dv_{10} at, approximately, $Re_{gen} = 12300$, whereas for $2\theta = 90^\circ$ there was a maximum SMD at about $Re_{gen} = 9500$ and a continuous decrease of Dv_{10} with Re_{gen} .

Figure 4.24 - Atomization patterns for like and unlike impingement jets of gels and liquids at several distances down from impingement point, $2\theta = 75^\circ$.



SOURCE: Author.

Figure 4.25 - SMD and Dv_{10} – Gelledethanollikeimpingement

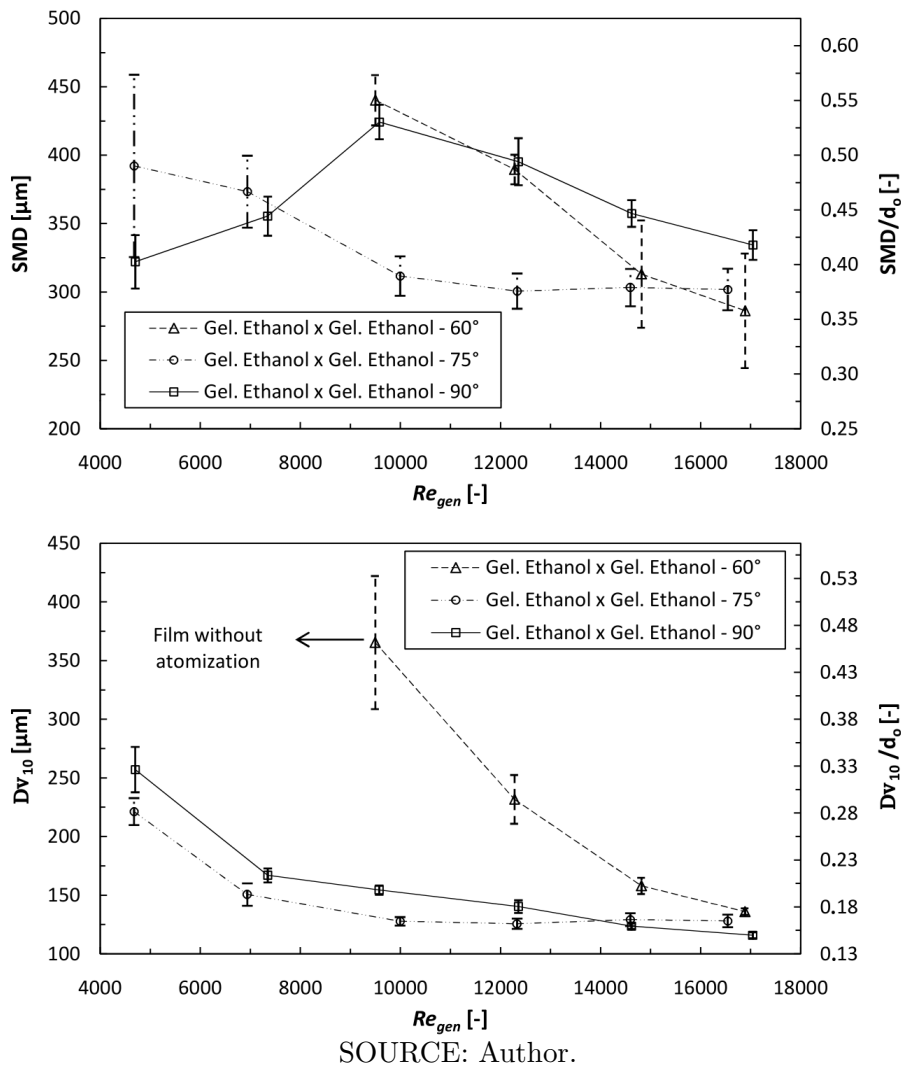
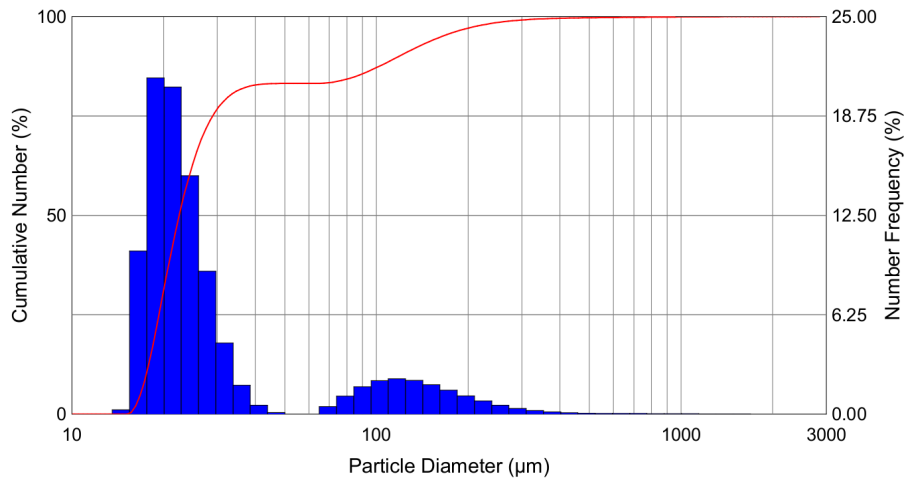


Figure 4.26 shows the drop size distribution of a spray formed by like impingement of gelled ethanol in terms of number frequency. As occurred for like impingement of liquid ethanol, the distribution for like impingement of gelled ethanol is clearly bi-modal. The Spraytec laser diffraction system determines the average diameter of an irregular particle considering a spherical particle with the same volume of the particle. The laser beam diameter is 10 mm and the maximum diameter measured is 2500 μm . Therefore ligaments and fragments with “diameters” larger than 2500 mm are not measured.

Figure 4.26 - Drop size distribution of a spray formed by like impingement of jets of gelled ethanol, $P_{inj} = 7 \text{ bar}$, $2\theta = 75^\circ$

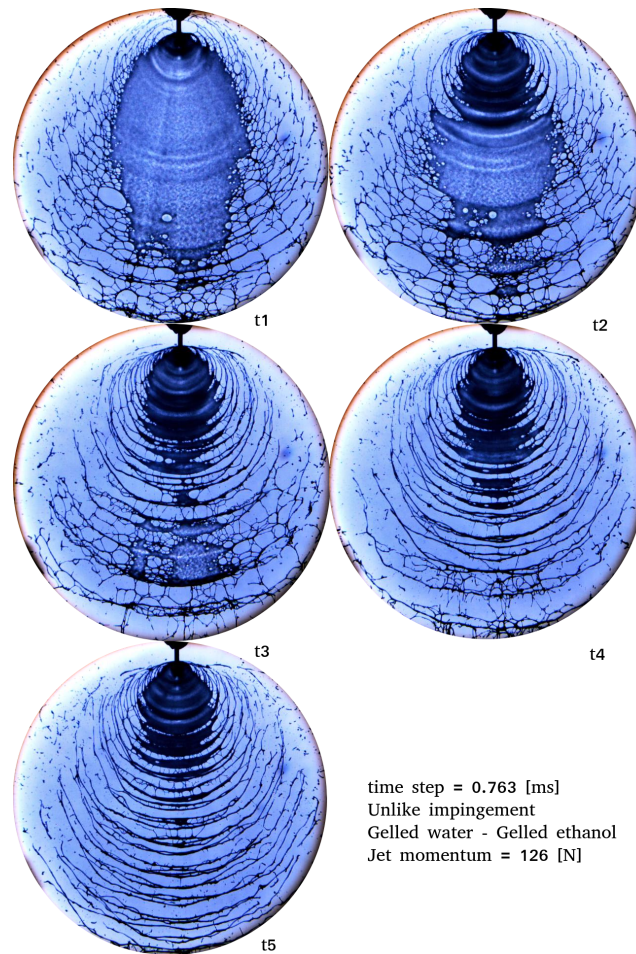


SOURCE: Author.

Drop size distribution measurements were not possible for like impingement of gelled water jets at 50 mm from the impingement point, since at this position the collision sheet was not completely disintegrated into ligaments and droplets.

Figure 4.27 depicts the transient behavior of the collision sheet for unlike impingement of gelled water/gelled ethanol jets. The sheet disintegrates at about 3 ms. In the case of like gelled ethanol such transient behavior was also frequent, whereas for like impingement of gelled water the sheet was relatively stable.

Figure 4.27 - Transient disintegration of the collision sheet for unlike impingement of gelled water/gelled ethanol jets with collision angle $2\theta = 75^\circ$



SOURCE: Author.

4.5 Atomization of Gels x Liquids, unlike impingement

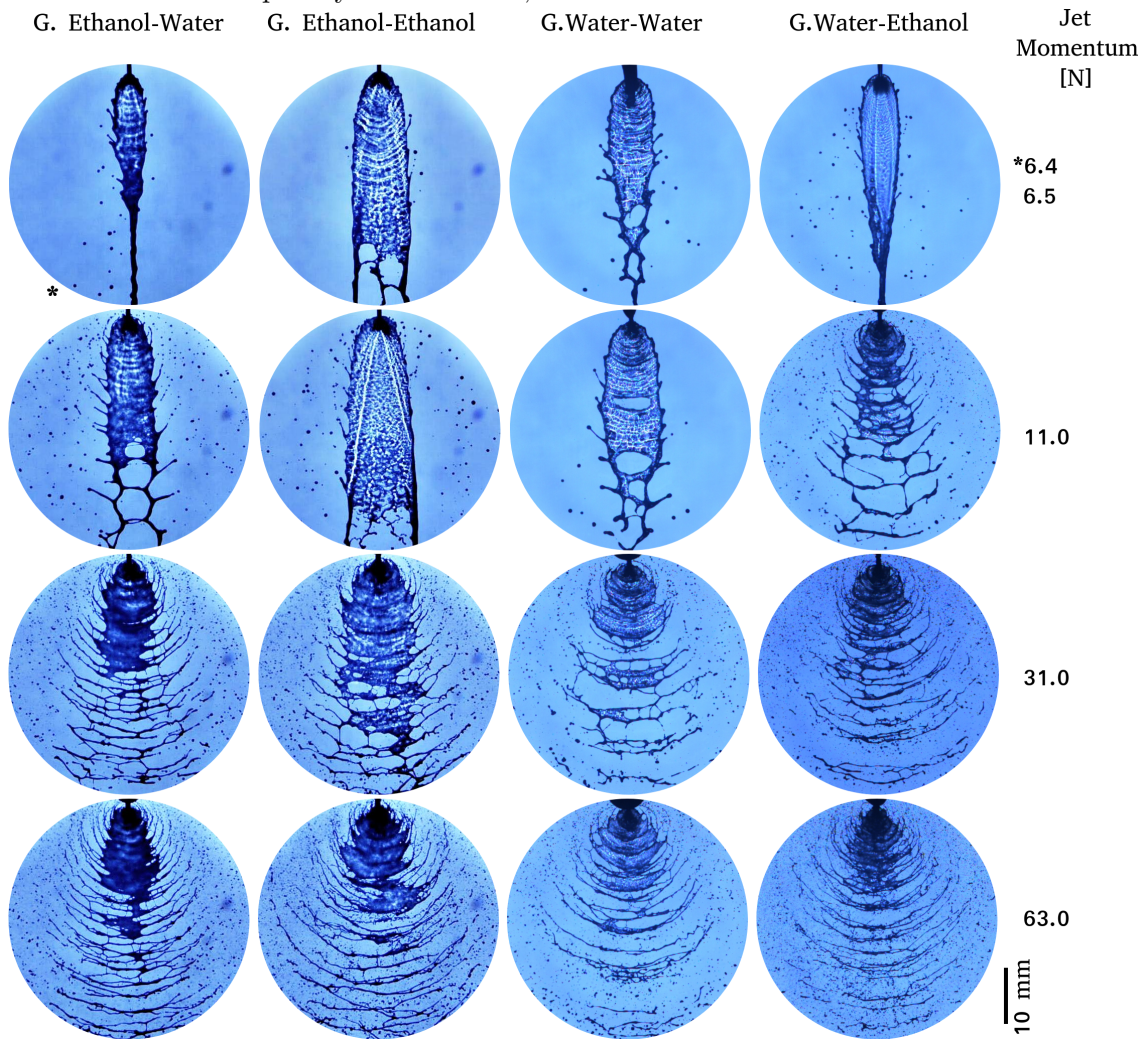
Unlike impingement of liquid jets against gel jets were also performed, perhaps for the first time, once results for this type of collision were not found in the literature.

Figure 4.28 presents shadow images of collision sheets from unlike impingement of gelled hydrous ethanol and gelled water jets with liquid water and liquid hydrous ethanol jets, for collision angle $2\theta = 75^\circ$ and several jet momentum values. Additional jet parameters are presented on Table 4.3.

Complex structures with ligaments are formed. Ligament breakup generates and releases droplets. Disturbances are clearly seen on gel/liquid sheets starting from

the impingement point even for low $\dot{m}v$, differently from gel unlike impingement shown in Figure 4.21. These collision sheet disturbances are probably induced by disturbances in the liquid jets, as seen in Figure 4.1.

Figure 4.28 - Gelled hydrous ethanol and gelled water unlike impinging with liquid water and liquid hydrous ethanol, $2\theta = 75^\circ$



SOURCE: Author.

Figure 4.24 has provided a comparison for unlike impingement of gelled hydrous ethanol x liquid water and hydrous ethanol x gelled water. At 50 mm down from the impingement point, there is still a remaining unbroken sheet for collision of jets of gelled hydrous ethanol and gelled water, while for gelled hydrous ethanol/liquid

water there is no collision sheet. It should be noted that images in Figure 4.24 show the most common sheet configuration in around 2000 pictures, but sometimes the collision sheet can break up suddenly, but it rapidly returns to its most common configuration.

Considering liquid sheet disintegration, or the atomization process, from image analysis (Figure 4.24 and others) it is possible to verify that, for the same jet momentum, unlike impingement shows better results than like impingement, and unlike impingement with one gel and one liquid is better than with two gels. In other words: atomization process goes better for gelled ethanol x liquid water than gelled ethanol x gelled water, both being better than like impingement gelled ethanol x gelled ethanol. "Better" in that case means less ligaments. The reasons for that improvement is that for like impingement of gels, the driven mechanisms is aerodynamic. By adding one jet of a different gel, becoming so an unlike impingement, the difference in jet velocity (considering equal jet momenta) forms a shear layer which favors ligament breakup and droplet formation. If the other jet is a liquid jet, and its pre-impingement conditions is disturbed, impact waves are introduced early at the liquid surface, that would be the third breakup mechanism. Summarizing these comments:

- Gel like impingement => aerodynamic instability + impact wave (when jet momentum is greater than 63 N);
- Gel/Gel unlike impingement => aerodynamic instability + shear layer due to difference in velocity + impact wave;
- Gel/Liquid unlike impingement => aerodynamic instability + shear layer due to difference in velocity + impact waves introduced early at the impingement point.

Figure 4.29 shows Sauter mean diameter (SMD) for unlike jet impingement of gelled hydrous ethanol with liquid water and liquid hydrous ethanol, varying collision angle and jet momentum. Table 4.4 shows minimum and maximum values of SMD and their respective jet momentum values, for unlike impingement of gelled hydrous ethanol with liquid water and liquid hydrous ethanol.

Table 4.4 - Maximum and minimum values of SMD for unlike impingement of gelled hydroous ethanol with liquid water and liquid hydrous ethanol, and their respective jet momentum values.

	impingement angle	max SMD [μm] / Jet Momentum [N]	min SMD [μm] / Jet Momentum [N]
Gelled Ethanol	60°	522.4 / 63	365.4 / 220
x	75°	407.4 / 63	287.0 / 220
Liquid Water	90°	383.9 / 63	282.0 / 188
Gelled Ethanol	60°	784.4 / 126	638.3 / 188
x	75°	767.6 / 126	535.1 / 188
Liquid Ethanol	90°	664.2 / 63	555.7 / 126

SOURCE: Author.

Figure 4.30 shows Sauter mean diameter (SMD) for unlike jet impingement of gelled water with liquid water and liquid hydrous ethanol, varying collision angle and jet momentum. Table 4.5 shows minimum and maximum values of SMD and their respective jet momentum values, for unlike impingement of gelled water with liquid water and liquid hydrous ethanol.

Table 4.5 - Maximum and minimum values of SMD for unlike impingement of gelled water with liquid water and liquid hydrous ethanol, and their respective jet momentum values.

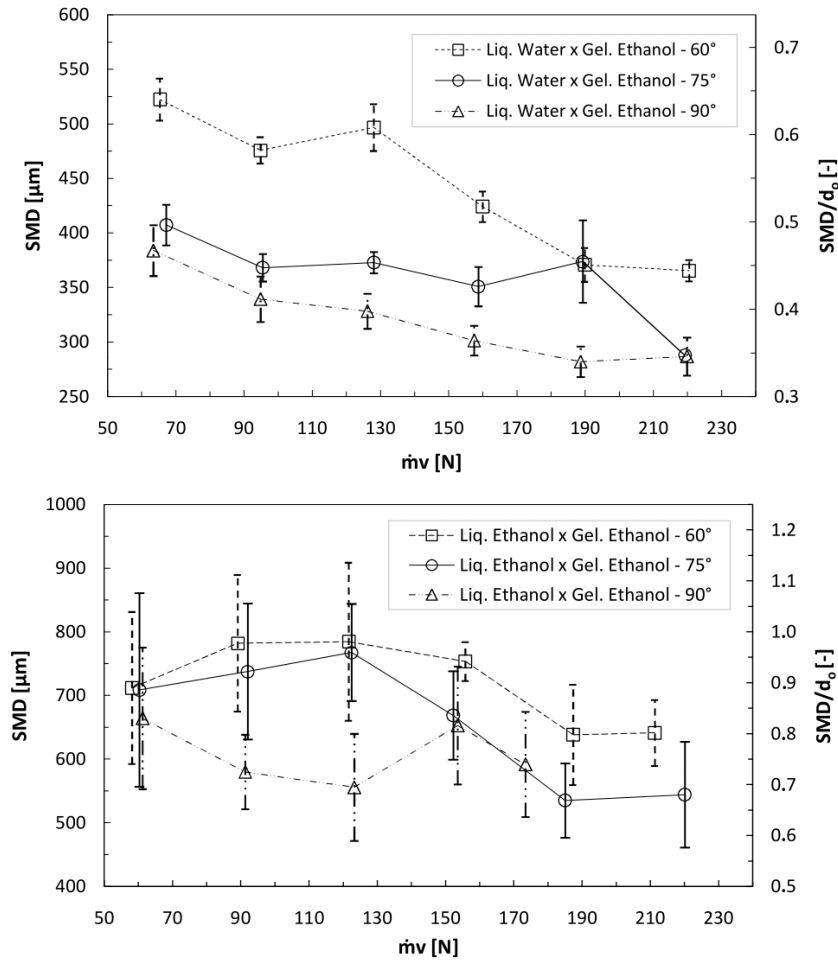
	impingement angle	max SMD [μm] / Jet Momentum [N]	min SMD [μm] / Jet Momentum [N]
Gelled Water	60°	702.4 / 63	324.8 / 220
x	75°	569.7 / 63	281.0 / 188
Liquid Water	90°	411.1 / 63	234.7 / 188
Gelled Water	60°	815.8 / 126	491.9 / 220
x	75°	594.9 / 63	349.6 / 220
Liquid Ethanol	90°	493.7 / 63	375.7 / 188

SOURCE: Author.

In the case of unlike impingement of gelled water / liquid water there is a continuous decrease of SMD with jet momentum. On the other hand, there is a non-monotonic variation of SMD for unlike impingement of liquid ethanol and gelled water. Large standard deviations and bi (or multi) modal particle size distributions were also verified, as in other experiments where ethanol was involved.

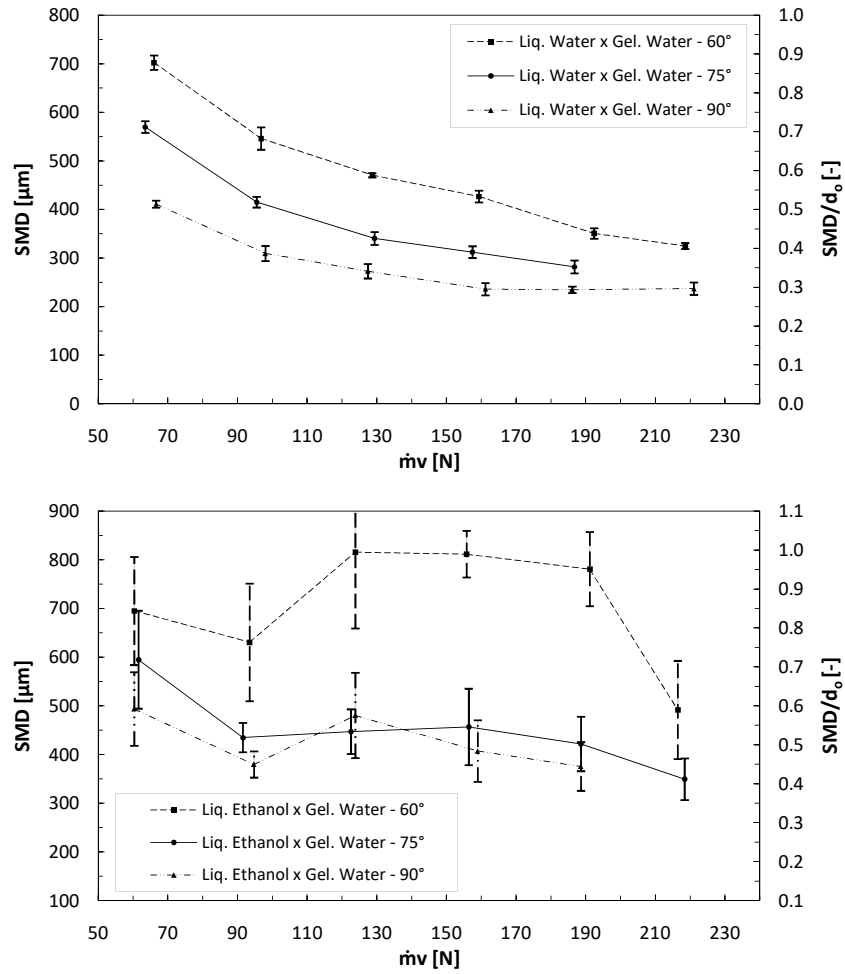
Figure 4.31 presents the droplet size distribution for unlike impingement of gelled water with liquid water and liquid ethanol. The distribution curve for impingement of gelled water/liquid water is similar to the liquid water like impingement.

Figure 4.29 - SMD for Gelled ethanol impinging with liquid water and liquid ethanol, unlike impingement



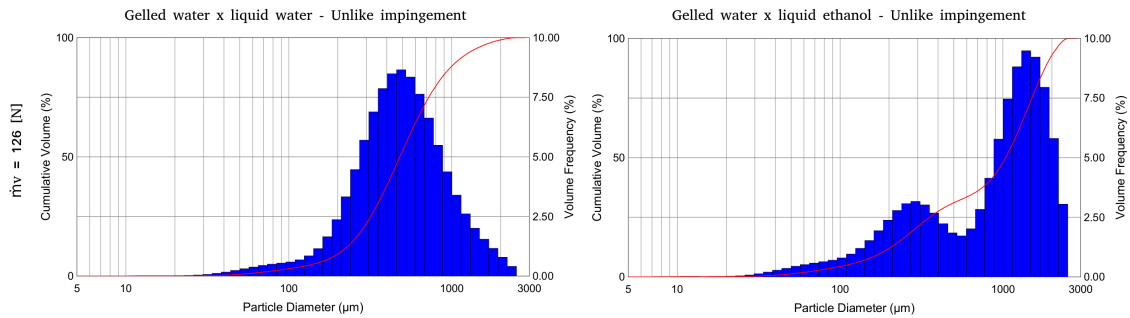
SOURCE: Author.

Figure 4.30 - SMD for gelled water impinging with liquid water and liquid hydrous ethanol - unlike impingement.



SOURCE: Author.

Figure 4.31 - Droplet size distribution by number volume for unlike impingement of gelled water with liquid water and liquid hydrous ethanol, $2\theta = 75^\circ$



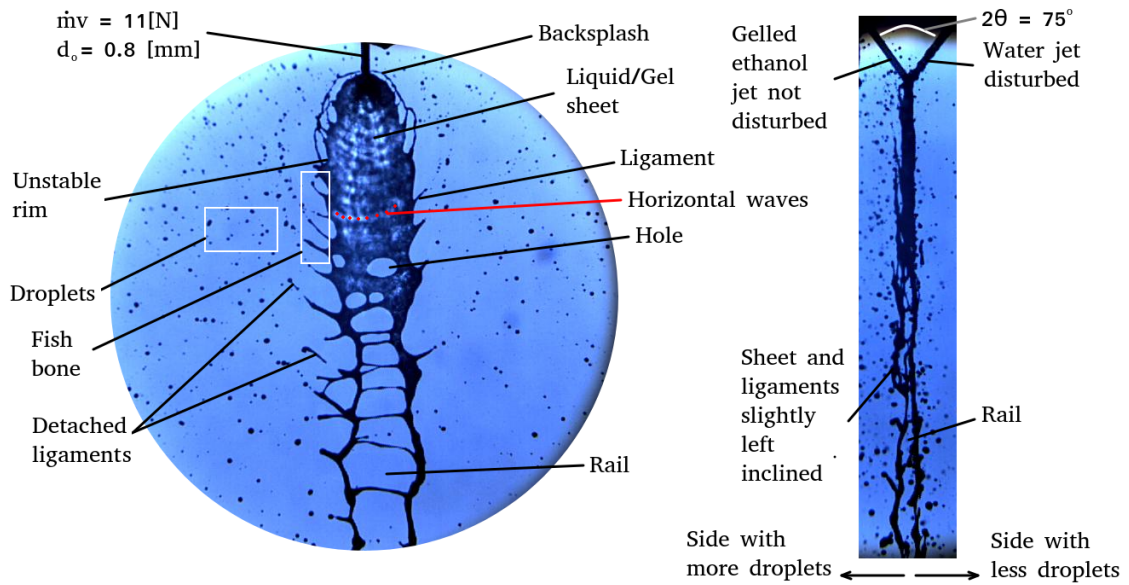
SOURCE: Author.

Figure 4.32 shows a shadowgraph of a liquid/gel sheet unlike impingement. The so-called "unstable open rim" regime presents fish bones and holes, as verified before by Jejurkar et al. (2018). A new pattern was introduced, the "rail". The rail pattern is similar to a network pattern (Figure 4.21) encountered in high viscosity sheets formed by impinging jets, but instead of fill all the sheet, it occurs frequently around the center-line even for longer distances from impingement point (Fig 4.24) and seems to be thicker.

The side view of Figure 4.32 reveals that the left side has more droplets than the right side. This may be explained by liquid water sliding over the gelled sheet and causing left inclined fish bones. In their work, Jejurkar et al. (2018) reported spherical and almost uniform sized droplets detaching from the unstable sheet made by like impingement of gels. Even in the more populated side, in the opposite side of the liquid water jet, it is not possible to ensure that the droplets are made only by liquid water and the rails only by gelled ethanol, as mentioned by Jejurkar et al. (2018).

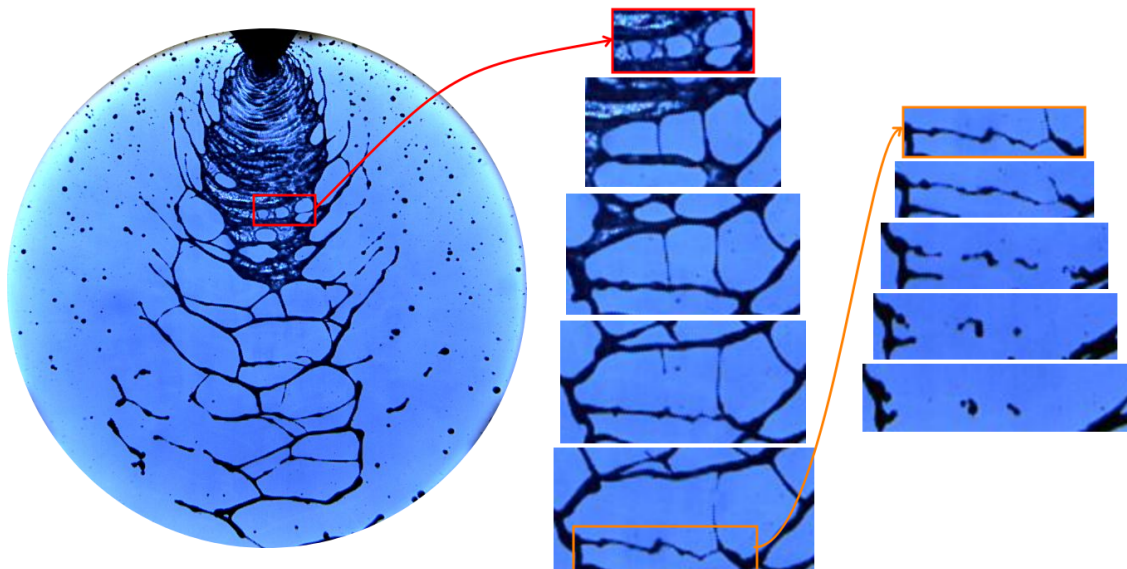
Figure 4.33 follows four about to merge holes, the subsequent formation of a network and disintegration of one ligament into droplets. The time-step between two images was 0.7092 ms. The two recent formed droplets seems to retract (or rotate). Such retracting phenomena is not an exclusivity of gelled fluids, however it can be enhanced by their elastic modulus. JEJURKAR et al. 2018

Figure 4.32 - Sheet breakup visualization - Gelled Ethanol x Liquid Water Unlike Impingement



SOURCE: Author.

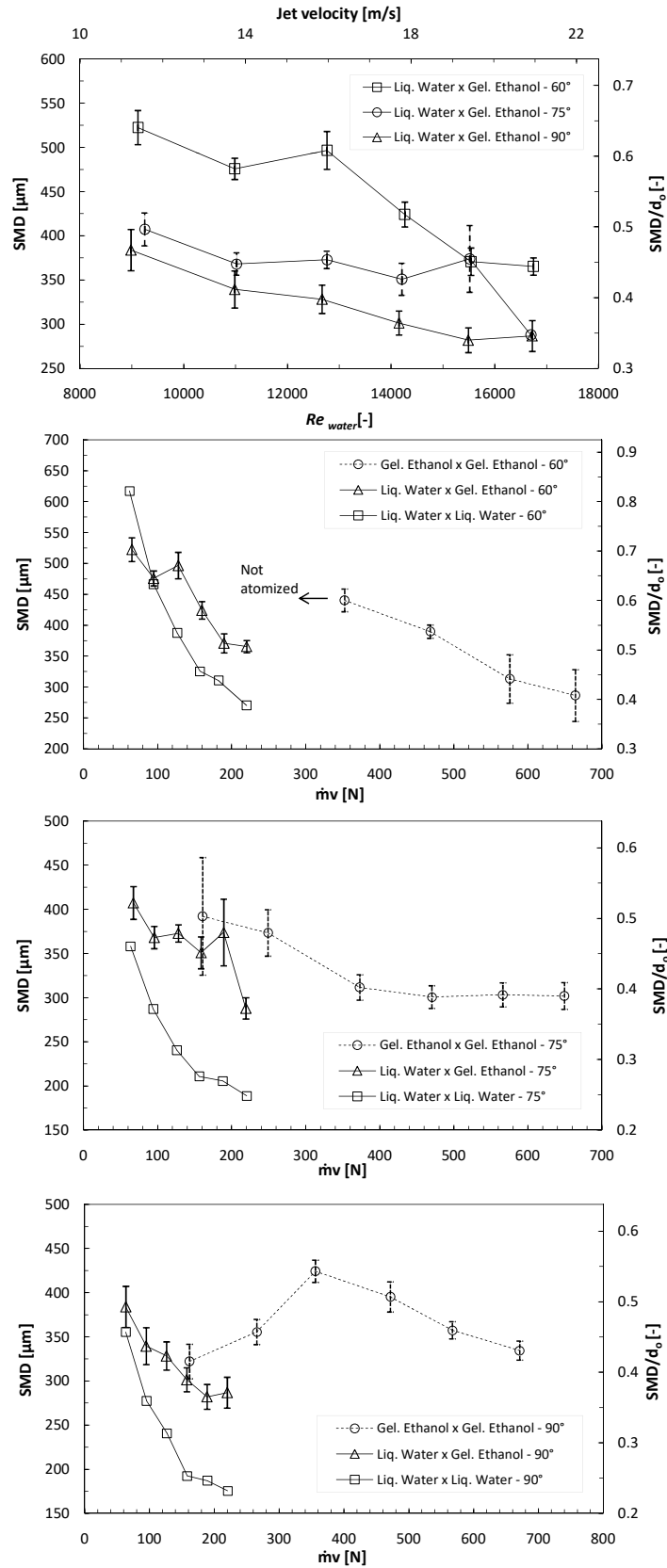
Figure 4.33 - Evolution of holes on sheet - Gelled Ethanol x Water Unlike Impingement - $2\theta=90^\circ$, $\dot{m}v=11$



SOURCE: Author.

Figure 4.34 compares SMD values of like impingement of liquid water and gelled hydrous ethanol to unlike impingement of liquid water and gelled ethanol. Unlike water/gelled ethanol have intermediate SMD values between the two like impingements, even gelled ethanol could not be atomized at the same jet momentum value.

Figure 4.34 - SMD for unlike impingement of Gelled Hydrus Ethanol x Liquid Water versus Re_{water} and jet momentum.



SOURCE: Author.

4.5.1 Weber or generalized Weber number

A common nondimensional number when analysing atomization phenomena is the Weber number, $We = \rho u_j^2 D / \sigma$. Most authors employ We number for Newtonian and non-newtonian fluids, stating that the properties are constant during the collision and atomization phenomena. The most accurate use of We should consider D , the characteristic length, as the droplet diameter or some extent of the ligament or sheet under study and the relative velocity between media and the fluid. In this work, for representative diameters results, the jet diameter was used as D and jet velocity as the relative velocity, considering the stationary air medium.

As mentioned in the literature review section, an equation for We_{gen} was given by Mallory (2012):

As mentioned in literature review section, an equation for We_{gen} was given by Mallory (2012)

$$We_{gen} = Oh_{gen}^{\frac{2}{2-n}} Re_{gen}^{\frac{2}{2-n}} \quad (4.4)$$

where

$$Oh_{gen} = \frac{k}{(\sigma^{(2-n)} \rho^n D^{(3n-2)})^{1/2}} \quad (4.5)$$

$$Re_{gen} = \frac{\rho u_{gel}^{2-n} D^n}{\mu [0.75 + (\frac{0.25}{n})]^n 8^{n-1}} \quad (4.6)$$

The Ostwald-de-Waele, or Power Law Reynolds number, employing a power law fitting curve, is largely used for atomization studies of non-Newtonian fluids.

A graph of inertia force ($\rho v^2 d_o$) versus We or We_{gen} was plotted, the result is in Figure 4.35. For a certain inertial force, considering the two non-Newtonian fluids in this work, We_{gen} is around 5.2 to 5.5 times greater than We .

Some gels have low surface tension values, but the two gelled fluids tested in this work present higher surface tensions compared to their liquid phases, as well as those gels in Mallory (2012).

In order to verify how We and We_{gen} works in linear stability model (with empirical breakup constant of 12 just as in Equation 2.32) and impact wave study, experimental data were plotted with model predictions for both Weber numbers, as showed in Figure 4.36.

For both We and We_{gen} , the impact wave model superestimates the atomization mechanism, predicting smaller SMD values than observed. The stability model with We predicts diameters between SMD and Dv_{10} , We_{gen} predicts droplets around Dv_{10} .

Figure 4.35 - Weber number - newtonian and non-Newtonian (generalized) comparison

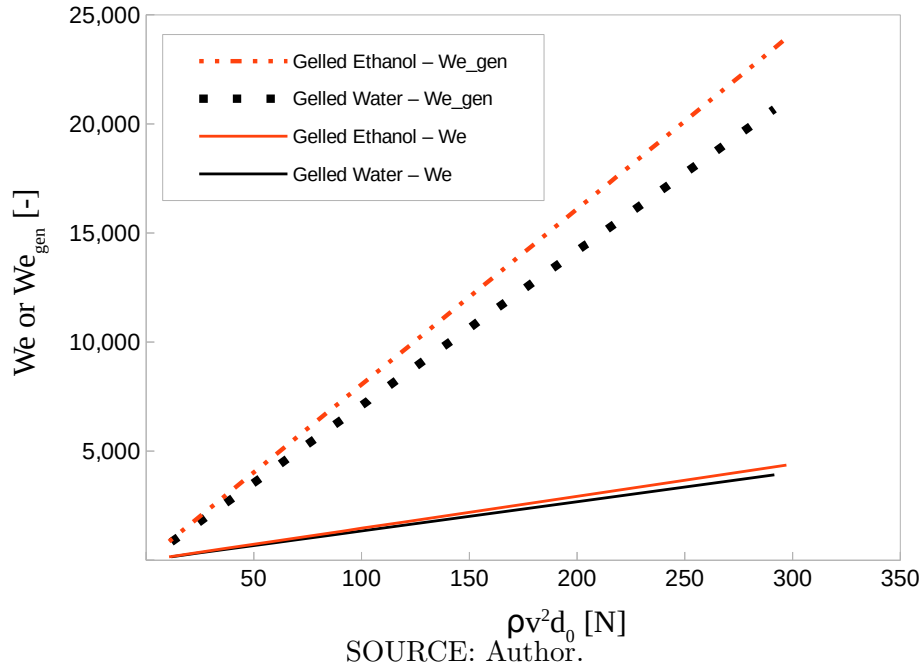
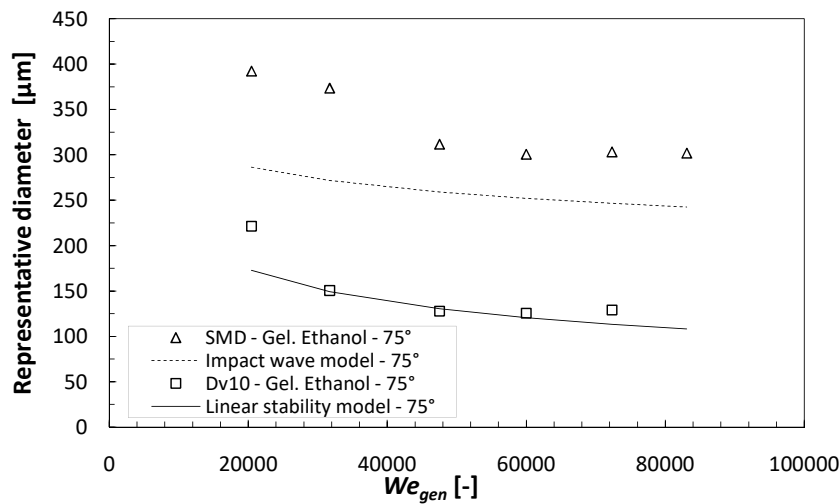
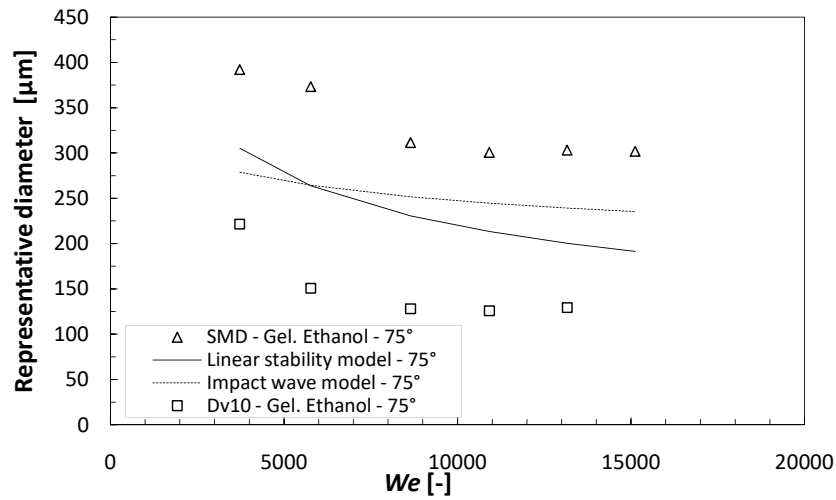


Figure 4.36 - Linear stability model predictions with We and We_{gen}



SOURCE: Author.

4.6 Droplet velocity in particular cases

Before formation of a fully developed spray, the collision sheet stays inside a plane. If this plane is vertical and droplets detached remain in this plane, the Z component of the droplet velocity can be neglected. Considering this case, droplet velocities were determined from batches of shadow images with known shutter speed. About 300 to 400 images of liquid water like impingement and liquid water/gelled hydrous ethanol unlike impingement were processed using PIVlab ensemble correlation (described in the Methodology Chapter).

Measured jet velocities for the test conditions are presented in Table 4.4.

Table 4.6 - Jet velocities.

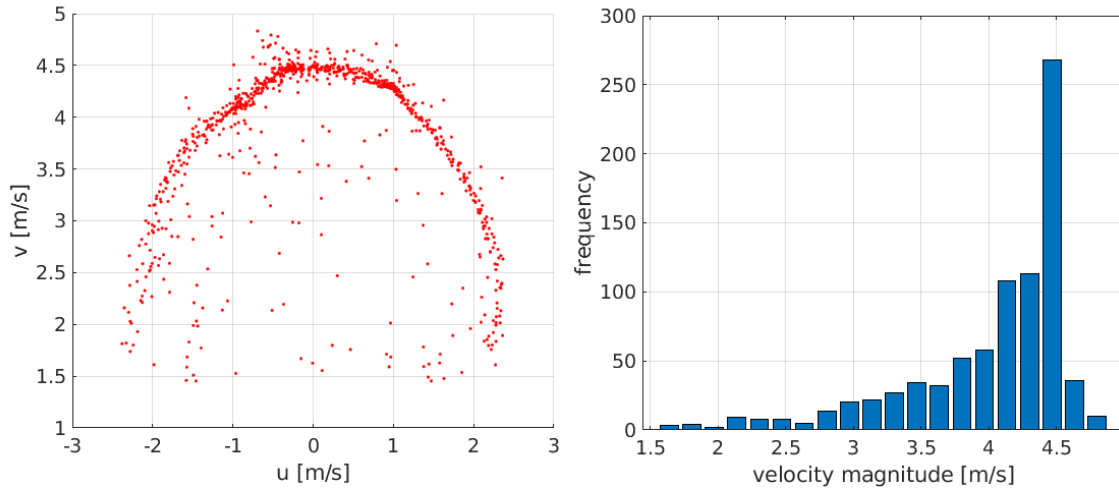
$\dot{m}v$ [N]	Water Jet velocity [m/s]	Gelled Ethanol jet velocity [m/s]
6.40	3.57	4.01
6.50	3.60	-
9.66	4.39	-
11.00	4.69	5.20
31.00	7.86	8.66

SOURCE: Author.

Figure 4.37 shows a scatter plot and histogram for particle velocities during unlike impingement of gelled hydrous ethanol x liquid water, with jet momentum of 11 N and collision angle of 90° .

As no mask were put to cover the sheet, the result represents ligaments and droplets. The u and v velocities represent horizontal and vertical velocities, respectively. Due to the impinging jet sheet and spray characteristics, the higher velocity is expected in the center-line. Although the scatter graph does not display distances, it is assumed that the region where $u = 0$ is the centerline. The denser red points region represents the most common velocity in the analysed area, including the disintegrating sheet and droplets. The histogram shows the frequency of finding particle velocities as function of velocity magnitude $(u^2 + v^2)^{1/2}$. The greater the distance from the center-line, the lowest the v and the highest the u , drawing a parabolic profile. Similar profiles are found in literature (CHOO; KANG, 2003), indicating that results with digital PIV with low cost lenses may be applied for particular cases.

Figure 4.37 - Particle velocities of ligaments and droplets for Unlike Impingement of Gelled Ethanol x Liquid Water, Jet momentum 11 N, $2\theta = 90^\circ$



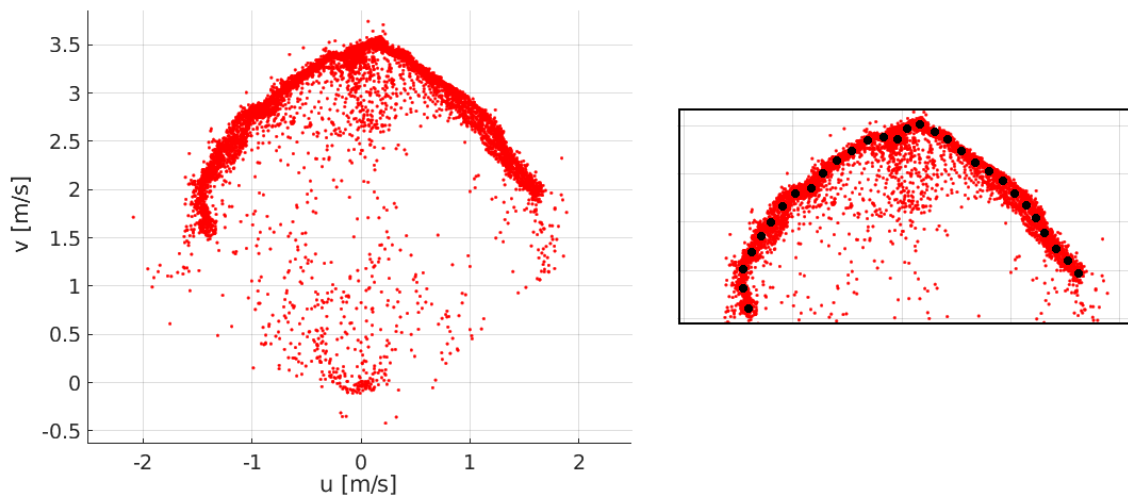
SOURCE: Author.

In order to compare results for different collision angles in a single graph, the densest area of scattering was filled manually with points, as seen in Figure 4.38, and their coordinates were then plotted.

Figure 4.39 shows particle velocities for water like impingement with two different jet velocities and three different collision angles. The lower the collision angle, the highest the velocity on center-line, due to the vertical component momentum. The highest 2θ , the more spread the droplets become, so the approximately parabolic profile becomes elongated. Such intuitive results match the findings in Figure 4.39.

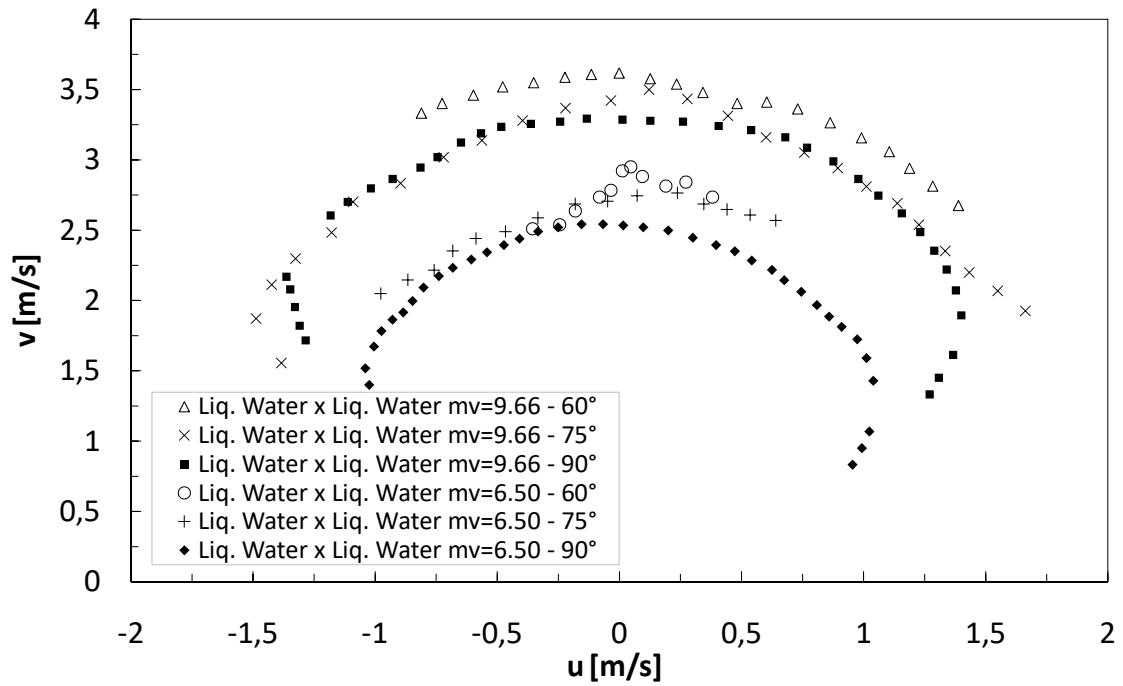
Choo and Kang (2003) reported similar results, as in Figure 4.39, where σ is the azimuthal angle, V_L the ligament velocity and V_j is the jet velocity. In their work, they found values V_L/V_j from 0.88 to 0.89, as seen in Fig 4.40, with large standard deviation, for $2\theta = 80^\circ$. The same ratio for the present work goes from 0.76 to 0.80 for $2\theta = 75^\circ$. Several factors may affect the ligament and droplet velocities, such as the jet pre-impingement velocity profile, that affects directly the sheet disintegration and subsequently the droplet and ligament velocities.

Figure 4.38 - Particle velocities of ligaments and droplets for Unlike Impingement of Gelled Hydrous Ethanol impinging with Liquid Water and Liquid Hydrous Ethanol.



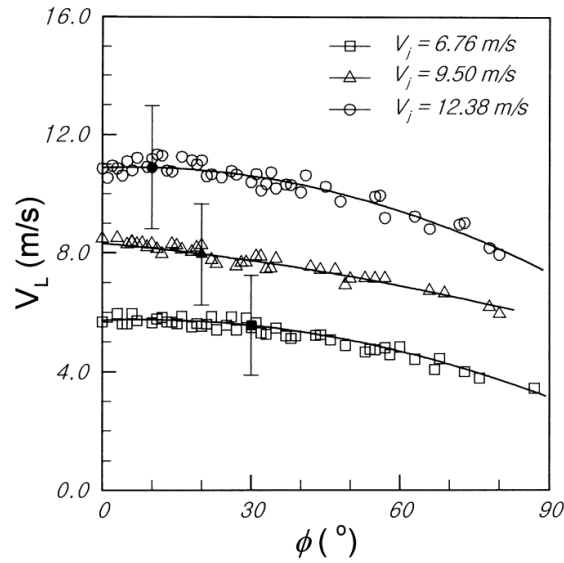
SOURCE: Author.

Figure 4.39 - Particle size distribution by number frequency, Gelled ethanol impinging with liquid water and ethanol, unlike impingement



SOURCE: Author.

Figure 4.40 - Ligament velocities varying jet velocity, for $2\theta = 80^\circ$

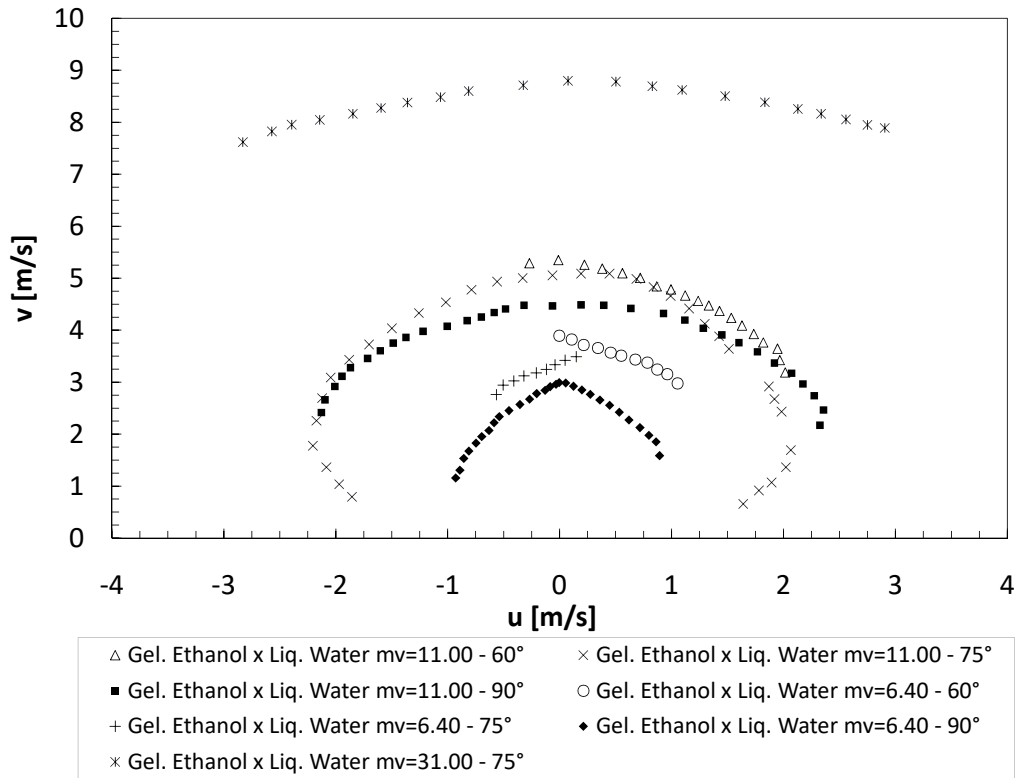


SOURCE: Choo e Kang (2003).

Figure 4.41 shows particle velocities for unlike impingement of gelled hydrous ethanol with liquid water and liquid ethanol. Similarly to previous results, approximately parabolic profiles in the scatter plot were found in most cases, with same trends with respect to 2θ and jet velocity. Droplet velocity/jet velocity ratio now increased due to the higher velocity of the gelled ethanol (Table 4.4), 0.87 to 0.98 and 1.00 for $2\theta = 75^\circ$, $\dot{m}v = 6.4, 11$ and 31 N, comparing to gel velocity jet. Although for jet momentum of 11 N there is a fully developed spray, with more droplets moving in the Z direction, it was helpful to notice the increase in 2D Droplet velocity/jet velocity ratio.

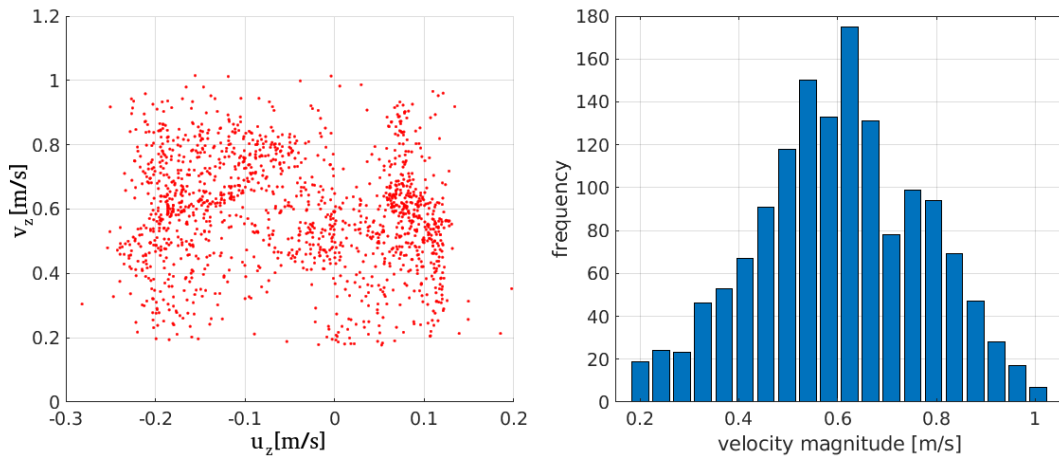
Figure 4.42 depicts a side view analysis of Figure 4.32. In that case a mask was put on the centerline, so the particles with velocity v_z are not the same as those ones with velocity v in Figure 4.41. Velocity v_z represents the particles right after the dense rail area (Figure 4.32), so they are a little apart center-line. The scatter graph reveals that the side with more droplets (left) also reaches highest velocities. The u_z velocity reaches maximum values of 0.05 of jet velocity.

Figure 4.41 - Particle velocities of ligaments and droplets for unlike impingement of gelled hydrous ethanol with liquid water and liquid hydrous ethanol.



SOURCE: Author.

Figure 4.42 - Droplet velocities for Unlike Impingement of Gelled Ethanol x Liquid Water, Jet momentum 11 N, $2\theta = 75^\circ$ - Scatter and histogram of particles in Z direction (side view of Figure 4.32)



SOURCE: Author.

4.7 Impinging jets simulation, preliminary results

Without going too much into details and equations, a preliminary CFD investigation about impinging jets started during this work. A Volume of Fluid (VoF) two-phase solver was chosen to simulate an impingement of two ethanol jets at $2\theta = 90^\circ$.

VOF method relies on the definition of an indicator function, in this case named α , that allows us to know whether the cell is occupied by one fluid or another, or a mixture of both.

The InterFoam solver implemented in OpenFOAM, solves Navier-Stokes equations for two incompressible, isothermal immiscible fluids. That means that the material properties are constant in the region filled by one of the two fluids except at the interphase.

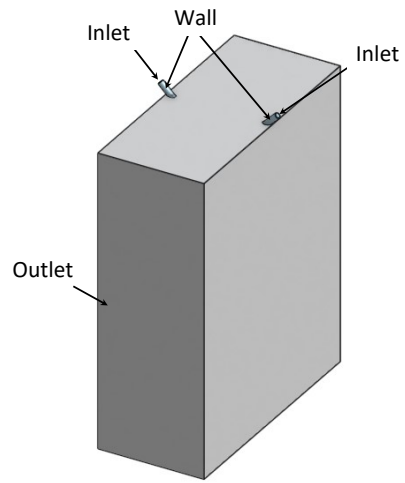
Figure 4.43 shows the .stl file representing the studied problem of two impinging jets, with two inlets of the same fluid (liquid ethanol), tubes with 0.8 mm internal diameter wall assuming the no slip condition which feed the fluid to the outlet initially with air. As soon as the two jets impinge, the atomization process begins.

The snappyHexMesh mesh generator was used in order to create a coarse mesh around the .stl file. During simulation, an adaptive mesh method with velocity field correction was used. The time step was adjusted by maximum Courant number of 1.

Figure 4.44 shows the output for $\alpha=0.5$, that means it reveals cells that have 50% of water content, something like the interface water/air. The writing time interval was 0.0004 seconds.

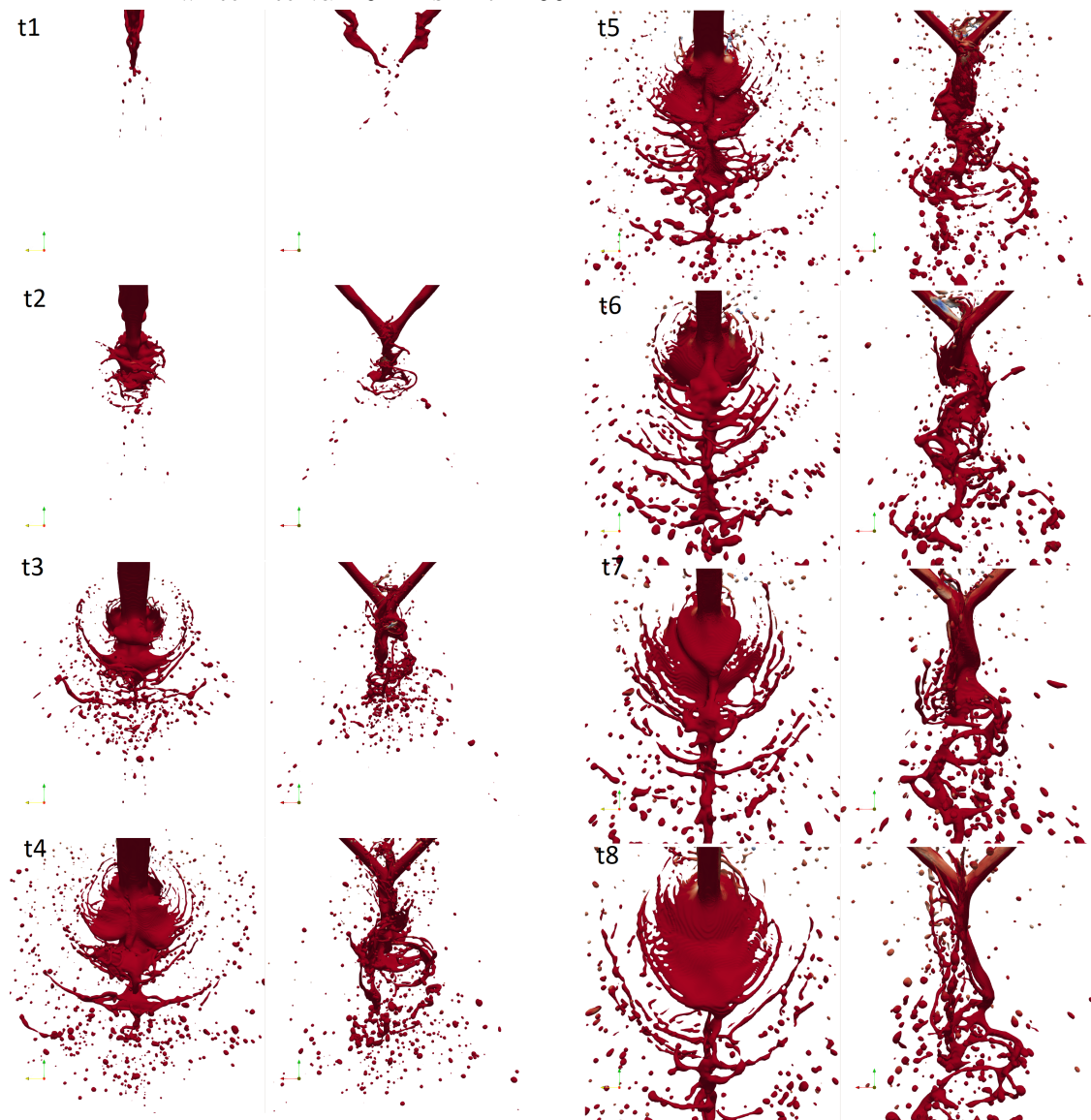
The preliminary numerical simulations have shown similarities with experiments. Further analysis of the parameters for this problem is required to improve results.

Figure 4.43 - .stl file for numerical simulation of like impingement - $2\theta = 90^\circ$



SOURCE: Author.

Figure 4.44 - Preliminary numerical results for Like impingement of liquid ethanol, $\alpha=0.5$,
write interval=0.4 ms - $2\theta = 90^\circ$



SOURCE: Author.

5 CONCLUSIONS

The atomization process by jet impingement of liquid and gelled simulant propellants was experimentally investigated. Tests were performed with like and unlike jets of liquid water, gelled water, liquid hydrous ethanol and gelled hydrous ethanol for different injection pressures, collision distances and collision angles.

Experimental data were obtained in terms of jet momenta and conventional or generalized non-dimensional numbers, Re , Re_{gen} , We and We_{gen} , for liquids and gels. It should be noted that the results and conclusions, especially the ones based on jet momentum, concern only the injectors tested in this work, since the internal geometry of other injectors may differ. A power law model was adopted to represent the gelled fluids and to define the generalized parameters.

Shadowgraph images of the collision sheets were obtained with help of a high speed camera. An open PIV software was used to calculate droplet velocities and showed a good capability to process a large number of batch images.

A patternator was used to estimate mass flux distributions of the sprays formed. Experimental spray mass flux distributions presented a good agreement with literature data. Despite gels could not flow easily into the patternator cells, a good estimate of the mass flux distribution was provided.

Droplet size distributions and representative droplet diameters (SMD and Dv_{10}) were determined by a Spraytec laser diffraction system. When using hydrous ethanol or gelled ethanol, no matter if on like or unlike impingement, large standard deviations for SMD and bi or multi-modal droplet size distributions were found, differently from most cases using water and gelled water. This was probably caused by secondary droplet breakup, due to the lower surface tension of ethanol compared to water.

Analytical solutions for sheet shapes presented good agreement for liquid fluids, but not for gelled ones, due to their high viscosity. Shadow images from a high speed camera showed that gel sprays formed by jet collision can generate complex structures with presence of holes, rails and/or fishbone geometries. Disturbances and impact waves in the collision sheet produce ligaments from which droplets are detached. Transient behavior has been observed in some cases with presence of different geometrical configurations.

Long ligaments require larger distances to fragment into drops and even with high

injection pressures some ligaments do not break up. This behavior of the gel film probably occurs as consequence of the absence or low intensity of impact waves introduced by the colliding jets.

The atomization of gelled fluids was improved by a colliding liquid jet, which acts as an atomization assistant generating disturbances to the gel/liquid film. Unlike jet impingement of gels, even with same jet momentum, creates a shear layer in the collision sheet due to the different jet velocities, improving the atomization process.

5.1 Future work suggestions

- Make gels in house to better control composition;
- Use proper characterization to analyse the effect of elastic modulus in gel atomization;
- Use image processing software together with enhanced optical apparatus to determine drop size distribution and representative diameters of sprays;
- Use advanced microscope technique, such as cryogenic field emission scanning electron microscopy to quantitative co-relate polymer network to the network gelled sheet pattern;
- Develop a new patternator to improve gel inflow;
- Study jet impingement of gels under higher pressures, for cold and combustion tests;
- Improve workbench with a PID controller and proper valves to, for example, simulate rocket launches conditions;
- Study effects of gel temperature on atomization;
- Study effects of suspended metallic particles;
- Study atomization and combustion of hypergolic gelled propellants.

REFERENCES

- AGGARWAL, R.; PATEL, I.; SHARMA, P.; THIRUMALVALAVAN. A comprehensive study on gelled propellants. **International Journal of Research in Engineering and Technology**, v. 4, p. 286–290, 2015. 2, 19
- ALMDAL, K.; DYRE, J.; HVIDT, S.; KRAMER, O. Towards a phenomenological definition of the term ‘gel’. **Polymer Gels and Networks**, v. 1, n. 1, p. 5 – 17, 1993. 7
- ANDERSON, W.; III, H. R.; SANTORO, R. Impact wave-based model of impinging jet atomization. **Atomization and Sprays**, v. 16, p. 791–805, 2006. 29, 30, 65
- ANDRADE, J.; MA, M.; KING, R.; GREGONIS, D. Contact angles at the solid-water interface. **Journal of Colloid and Interface Science**, v. 72, n. 3, p. 488–494, 1979. 12
- ASHGRIZ, N. **Handbook of Atomization and Sprays**. New York: Springer, 2011. 14, 18, 28, 34, 85
- ASHGRIZ, N.; BROCKLEHURST, W. Mixing mechanisms in a pair of impinging jets. **Journal of Propulsion and Power**, v. 17, n. 3, p. 736–749, 2001. 85, 86
- BAEK, G.; KIM, C. Rheological properties of carbopol containing nanoparticles. **Journal of Rheology**, v. 55, n. 2, p. 313–330, 2011. 10
- BAEK, G.; KIM, S.; HAN, J.; KIM, C. Atomization characteristics of impinging jets of gel material containing nanoparticles. **Journal of Non-Newtonian Fluid Mechanics**, v. 166, p. 1272–1285, 2011. 19
- BAILARDI, G. **On the atomization behavior of newtonian fluids with an impinging jet injector**. 138 p. Corso di Laurea Specialistica in Ingegneria Aeronautica — Politecnico di Milano, Milano, Italy, 2010. 16
- BARNES, H. **A handbook of elementary rheology**. Aberystwyth, U.K.: Institute of Non-Newtonian Fluid Mechanics, 2000. 10
- BENNEWITZ, J.; FREDERICK, R. Overview of combustion instabilities in liquid rocket engines - coupling mechanisms control techniques. In: AIAA/ASME/SAE/ASEE JOINT PROPULSION CONFERENCE, 49., 2013. **Proceedings...** San Jose, CA, 2013. 1

BERTOLA, V. Preface: non-newtonian drops and sprays. **Atomization and Sprays**, v. 27, p. 5–6, 2017. 2

BIO-RAD LABORATORIES, INC. SPECTRABASE. **Spectrabase**. 2019.
Disponível em: <<https://spectrabase.com/>>. Acesso em: 20 Dec. 2019. 44

BOTCHU, V.; BAEK, S. Rheological characterization of ethanolamine gel propellants. **Journal of Energetic Materials**, v. 34, p. 260–278, 01 2016. 43

BRETAS, R.; D'ÁVILA, M. **Reologia de polímeros fundidos**. São Carlos: EdUFSCar, 2005. 2, 9, 13

CARREAU, P. Rheological equations from molecular network theories. **Transactions of the Society of Rheology**, v. 16, n. 1, p. 99–127, 1972. 5

CHEN, X.; YANG, V. Recent advances in physical understanding and quantitative prediction of impinging-jet dynamics and atomization. **Chinese Journal of Aeronautics**, v. 32, n. 1, p. 45–57, 2019. 14, 15, 17, 31, 32

CHHABRA, R.; RICHARDSON, J. Chapter 1 - non-newtonian fluid behaviour. In: CHHABRA, R.; RICHARDSON, J. (Ed.). **Non-Newtonian Flow and Applied Rheology**. Oxford: Butterworth-Heinemann, 2008. p. 1 – 55. 5

CHOO, Y.; KANG, B. A study on the velocity characteristics of the liquid elements produced by two impinging jets. **Experiments in Fluids**, v. 34, p. 655–661, 2003. 108, 111

CIEZKI, H.; HÜRTTLEN, J.; NAUMANN, K.; NEGRI, M.; RAMSEL, J.; WEISER, V. Overview of the german gel propulsion technology program. In: AIAA/ASME/SAE/ASEE JOINT PROPULSION CONFERENCE, 50., 2014. **Proceedings...** Cleveland, OH, 2014. 3

CIEZKI, H.; NE. Atomization of viscoelastic fluids with an impinging jet injector: morphology and physical mechanism of thread formation. **Atomization and Sprays**, v. 27, p. 319–336, 2017. 2, 14, 18

CIEZKI, H.; NEGRI, M. Atomization of non-newtonian fluids with an impinging jet injector: influence of viscoelasticity on hindering droplets formation. In: AIAA/ASME/SAE/ASEE JOINT PROPULSION CONFERENCE, 46., 2010. **Proceedings...** Nashville, TN, 2010. 18

CIEZKI, H.; NEGRI, M.; GERNOETH, A. Advanced liquid and gelled propellants for rocket and ramjet propulsion. **International Journal of Energetic Materials and Chemical Propulsion**, v. 2, n. 14, p. 85–123, 2015. 2

CIEZKI, H.; PINTO, P.; HÜRTTLEN, J.; KIRCHBERGER, C.; STIEFEL, A.; KRÖGER, P.; RAMSEL, J.; NAUMANN, W.; SCHALLER, U.; IMIOLEK, A.; WEISER, V. Overview on the german gel propulsion technology activities: Status 2017 and outlook. In: EUROPEAN CONFERENCE FOR AEROSPACE SCIENCES, 7., 2017. **Proceedings...** Milan, Italy, 2017. 2

CONNELL, T.; RISHA, G.; YETTER, R.; NATAN, B. Hypergolic ignition of hydrogen peroxide/gel fuel impinging jets. **Journal of Propulsion and Power**, v. 34, n. 1, p. 182–188, 2018. 19

DASGUPTA, D.; NATH, S.; MUKHOPADHYAY, A. Linear and non-linear analysis of breakup of liquid sheets: a review. **Journal of the Indian Institute of Science**, v. 99, 10 2018. 30, 31

DENG, H.; FENG, F.; ZHUO, C. A simplified linear model and breakup characteristics of power-law sheet formed by a doublet impinging injector. **Proceedings of IMechE Part G: Journal Aerospace Engineering**, v. 232, p. 1035–1046, 2018. 14, 18, 68

DIAS, G. S.; ANDRADE, J. C.; FISCHER, G. A. A.; COSTA, F. S. Coeficientes de descarga de injetores de jato. In: WORKSHOP EM ENGENHARIA E TECNOLOGIA ESPACIAIS, 10., 2019. **Anais...** São José dos Campos, SP, 2019. 52

_____. Experimental study of atomization by impinging jets of liquid and gelled green propellants. In: INTERNATIONAL CONGRESS OF MECHANICAL ENGINEERING, 25., 2019. **Proceedings...** Uberlândia, MG, 2019. 67, 68

DOMBROWSKI, N.; HOOPER, P. The performance characteristics of an impinging jet atomizer in atmospheres of high ambient density. **Fuel**, v. 41, p. 323–334, 1962. 69

_____. A study of the sprays formed by impinging jets in laminar and turbulent flow. **Journal of Fluid Mechanics**, v. 18, n. 3, p. 392–400, 1964. 69

DOMBROWSKI, N.; JOHNS, W. The aerodynamic instability and disintegration of viscous liquid sheets. **Chemical Engineering Science**, v. 18, p. 203–214, 1963. 15, 31

- EMEKWURU, N. Using the general gamma distribution to represent the droplet size distribution in a spray model. In: ZHENG, J. H. (Ed.). **Hydrodynamics – theory and model**. United Kingdom: IntechOpen, 2012. p. 79–94. 74
- EMEKWURU, N.; WATKINS, A. Analysis of a two-fluid sprayer and its use to develop the number size distribution moments spray model, part i: experimental analysis. **Atomization and Sprays**, v. 20, n. 6, p. 467–484, 2010. 74
- FAETH, G. M.; HSIANG, L.; WU, P. Structure and breakup properties of sprays. **International Journal of Multiphase Flow**, v. 21, p. 99–127, 1995. 33
- FAJGENBAUM, R.; SANTOS, R. G. Influence of ethanol temperature on atomization parameters from a multi-hole port fuel injector. In: INTERNATIONAL CONGRESS OF MECHANICAL ENGINEERING, 22., 2013. **Proceedings...** Ribeirão Preto, SP, 2013. 38
- FAKHRI, S.; LEE, J.; YETTER, R. Effect of nozzle geometry on the atomization and spray characteristics of gelled-propellant simultants formed by two impinging jets. **Atomization and Sprays**, v. 20, n. 12, p. 1033–1046, 2010. 3, 15
- FISCHER, G. A. A. **Atomização de géis por injetores centrífugos e jato-centrífugos para aplicações em propulsão de foguetes**. 2019. 506 p. Tese (Doutorado em Combustão e Propulsão) — Instituto Nacional de Pesquisas Espaciais, São José dos Campos. 2
- FOX, R.; MCDONALD, A.; PRITCHARD, P. **Introduction to fluid mechanics**. Hoboken, NJ: Wiley, 2011. 61
- FU, Q.; DUAN, R.; CUI, K.; YANG, L. Spray of gelled propellants from an impinging-jet injector under different temperatures. **Aerospace Science and Technology**, v. 39, p. 552–528, 2014. 18
- GILL, G. S.; NURICK, W. H. **Liquid rocket engine injectors**. Glenn Research Center, 1976. Technical note SP-8089. 78
- HAN, Y. **Twin-jet sprays for fuel direct injection**. 2016. 183 p. Tese (Doutorado em Engenharia) — Technischen Fakultät der Friedrich-Alexander, Erlangen, Germany, 2016. 27
- HEIDMANN, M.; FOSTER, H. **Effect of impingement angle on drop-size distribution and spray pattern of two impinging water jets**. Washington: [s.n.], 1961. Technical note D-872. 74

HUANG, Z.; HANLIANG, B. Numerical prediction of the outcomes of binary-droplet collision in steam-water separator. In: INTERNATIONAL CONFERENCE ON NUCLEAR ENGINEERING, 21., 2013. **Proceedings...** Chengdu, China, 2013. 36

IBRAHIM, E. A.; PRZEKOWAS, A. J. Impinging jets atomization. **Physics of Fluids A**, v. 3, n. 12, p. 2981–2987, 1991. 26, 27

INTERNATIONAL ORGANIZATION FOR STANDARDIZATION. ISO 13320-1.: **particle size analysis – laser diffraction methods – Part 1: General principles**. Geneva, Switzerland, 1999. 22

JEJURKAR, S.; YADAV, G.; MISHRA, D. Visualizations of sheet breakup of non-newtonian gels loaded with nanoparticles. **International Journal of Multiphase Flow**, v. 100, p. 57–76, 2018. 101

JOHNSON, B.; PRUD'HOMME, R. Chemical processing and micromixing in confined impinging jets. **AIChE Journal**, v. 49, n. 9, p. 2264–2282, 2004. 14

Definitions of terms relating to the structure and processing of sols, gels, networks and inorganic-organic hybrid materials. In: JONES, R.; KAHOVEC, J.; STEPTO, R.; WILKS, E.; HESS, M.; KITAYAMA, T.; METANOMSKI, W. (Ed.). **Compendium of polymer terminology and nomenclature: IUPAC recommendations**. [S.l.]: The Royal Society of Chemistry, 2007. v. 11, p. 211–236. 7

KAEUBLE, D. H. Dispersion-polar surface tension properties of organic solids. **The Journal of Adhesion**, v. 2, p. 66–81, 1970. 48

KAMPEN, J.; CIEZKI, H.; TIEDT, T.; MADLENER, K. Some aspects of the atomization behavior of newtonian and of shear-thinning gelled non-newtonian fluids with an impinging jet injector. In: AIAA/ASME/SAE/ASEE JOINT PROPULSION CONFERENCE, 42., 2006. **Proceedings...** Sacramento, California, 2006. 18

KHATTAB, I.; BANDARKAR, F.; FAKHREE, M. A. A.; JOUYBAN, A. Density, viscosity, and surface tension of water+ ethanol mixtures from 293 to 323k. **Korean Journal of Chemical Engineering**, v. 29, p. 812–817, 06 2012. 38

KHAVKIN, Y. **Theory and practice swirl atomizers**. New York: Taylor Francis, 2004. 3

- KLINE, S. J.; MCCLINTOCK, F. A. Describing uncertainties in single-sample experiments. **Mechanical Engineering**, v. 75, n. 1, p. 3–9, 1953. 62
- KOTHE, D.; MJOLSNESS, R. Ripple – a new model for incompressible flows with free surfaces. **AIAA Journal**, v. 30, n. 11, p. 2694–2700, 1992. 33
- LAI, W.-H.; WANG, H. C. Flow patterns generated by like- and unlike-doublet impinging jets. In: AIAA/ASME/SAE/ASEE JOINT PROPULSION CONFERENCE, 38., 2002. **Proceedings...** Indianapolis, Indiana, 2002. 79
- LAM, C.; MARTIN, P.; JEFFERIS, S. Rheological properties of phpa polymer support fluids. **Journal of Material in Civil Engineering**, v. 27, n. 11, p. 1–9, 2015. 10
- LEFEBVRE, A. **Atomization and sprays**. West Lafayette, Indiana: Taylor Francis, 1988. 18, 20
- LI, R.; ASHGRIZ, N. Characteristics of liquid sheets formed by two impinging jets. **Physics of Fluids**, v. 18, p. 1–13, 2006. 67
- MACOSKO, C. W. **Rheology**. New York, US: Willey, 1994. 8
- MALLORY, J. **Jet impingement and primary atomization of non-Newtonian liquids**. 202 p. Tese (Doutorado em Engenharia Mecânica) — Purdue University Graduate School, West Lafayette, Indiana, 2012. 19, 20
- MEWIS, J.; WAGNER, N. J. Thixotropy. **Advances in Colloid and Interface Science**, v. 147-148, p. 214 – 227, 2009. ISSN 0001-8686. Disponível em: <<http://www.sciencedirect.com/science/article/pii/S0001868608001735>>. 13, 14
- MEYER, R. X. **Elements of space technology**. San Diego: Academic Press, 1999. Pp. 97-98. 1
- MOLDEX3D. **Viscosity model**. 2020. Disponível em: <http://support.moldex3d.com/r16/en/standardinjectionmolding_material_materialmodels_viscositymodelforthermoplastic.html>. Acesso em: 16 Feb. 2020. 9
- MOREIRA-JÚNIOR, P. W. P. **Diagnósticos de plasmas de dietilenoglicol dimetil-eter (DIGLIME), 2-metil-2-oxazolona (OXAZOLINA) e da mistura de etilendiamina com acetileno (EDA eC₂H₂):deposição polimérica**. 219 p. Tese (Doutorado em Engenharia Mecânica) — Faculdade de

Engenharia do Campus de Guaratinguetá, UNESP, Guaratinguetá, São Paulo, 2019. 11, 12

NAKAMURA, T.; HATTORI, M.; KAWASAKI, H.; MIYAMOTO, K.; TOKITA, M.; KOMAI, T. Surface tension of the polymer network of a gel. **Physical Review E**, v. 54, n. 2, p. 1663–1668, 1996. 12

NANOSCIENCE. **Contact angle goniometry**. 2020. Disponível em: <<https://www.nanoscience.com/techniques/tensiometry>>. Acesso em: 17 Feb. 2020. 11

NAUMANN, K.; CIEZKI, H.; STIERLE, R.; SCHMID, K.; RAMSEL, J. Rocket propulsion with gelled propellants for sounding rockets. In: SYMPOSIUM ON EUROPEAN ROCKET AND BALLOON PROGRAMMES AND RELATED RESEARCH, 20., 2011. **Proceedings...** Hyère, France, 2011. 3

NGUYEN, Q.; NGUYEN, N. **Continuum mechanics: progress in fundamentals and engineering applications**. Rijeka, Croatia: InTech, 2012. 5, 7

OSS, C. **Interfacial forces in aqueous media**. Boca Raton, Florida: Taylor Francis Group, 2006. 48

OWENS, D.; WENDT, R. Estimation of the surface free energy of polymers. **Journal of Applied Polymer Science**, v. 13, p. 1741–1747, 1969. 48

PANÃO, M.; MOREIRA, A. Physical analysis of multimodality in atomization processes. In: **23rd Annual Conference on Liquid Atomization and Spray Systems**. [S.l.: s.n.], 2010. p. 1–11. 74

PECK, D. H. R. E. Thickness distribution in a sheet formed by impinging jets. **AIChE Journal**, American Institute of Chemical Engineers, v. 10, p. 752–754, 1964. 27

PENNER, M. H. Basic principles of spectroscopy. In: NIELSEN, S. E. (Ed.). **Food analysis**. Cham: Springer International Publishing, 2007. p. 79–88. 25

PETROBRAS. **Ficha de Informações de Segurança de Produto Químico -FISPQ**. 2019. Disponível em: <<http://www.br.com.br/wcm/connect/6fad4419-69ca-47f1-aabb-b507d1980d19/fispq-comb-etanol-etanol-hidratado-combustivel-ehc-rev02.pdf?MOD=AJPERES&CVID=1LpYx9u>>. 38

PIVLAB. **The benefit of ensemble correlation in PIVlab v2.30**. 2019. Disponível em: <<https://pivlab.blogspot.com/2019/09/the-benefit-of-ensemble-correlation-in.html>>. Acesso em: 02 Apr. 2019. 58

PREZIOSO, D.; DANTE DI DOMENICO, D.; PANE, M.; CICCARELLI, D.; D'ERRICO, G. Ion specificity in determining physico-chemical properties of drinking water. **Food Science and Technology**, 04 2018. 37

RABE, C.; MALET, J.; FEUILLEBOIS, F. Experimental investigation of water droplet binary collisions and description of outcomes with a symmetric weber number. **Physics of Fluids**, v. 22, n. 4, p. 047101, 2010. 35

RABEL, W. Einige aspekte der benetzungstheorie und ihre anwendung auf die untersuchung und veränderung der oberflächeneigenschaften von polymeren. **Farbe und Lack**, v. 77, p. 997–1005, 1969. 48

RAFFEL, M.; WILLERT, C.; SCARANO, F.; KÄHLER, C.; WERELEY, S.; KOMPENHANSSETTLES, J. **Particle image velocimetry: a practical guide**. Cham, Switzerland: Springer, 2018. 23, 24

RAMASUBRAMANIAN, C.; NOTARO, V.; LEE, J. G. Characterization of near-field spray of nongelled- and gelled-impinging doublets at high pressure. **Journal of Propulsion and Power**, p. 1–11, 2015. 18

RAPP, B. E. Surface tension. In: RAPP, B. E. (Ed.). **Microfluidics: modelling, mechanics and mathematics**. Oxford: Elsevier, 2077. p. 421–444. 11

RR AUCTION. **Apollo LMAE Injector Plate**. 2017. Disponível em: <https://issuu.com/rrauction/docs/rr_auction_march_2017_space_aviatio>. Acesso em: 20 Feb. 2020. 16, 17

RUHR-UNIVERSITÄT BOCHUM. **FTIR-Spectroscopy**. 2020. Disponível em: <<https://www.ruhr-uni-bochum.de/pc1/methoden/ftir-spectroscopy.html.en>>. Acesso em: 10 Apr. 2019. 26

RYAN, H. M.; ANDERSON, W. E.; PAL, S.; SANTORO, R. J. Atomization characteristics of impinging liquid jets. **Journal of Propulsion and Power**, v. 11, n. 1, p. 135–145, 1995. 31, 32

SCOPUS. **Scopus analyze search results**. 2020. Disponível em: <<https://www.scopus.com/>>. 16

SCOTT, T. A. Refractive index of ethanol–water mixtures and density and refractive index of ethanol–water–ethyl ether mixtures. **The Journal of Physical Chemistry**, v. 50, n. 5, p. 406–412, 1946. 58

SETTLES, G. **Schlieren and shadowgraph techniques**. New York: Springer, 2001. 22, 23

SILVA, F.; MURAMATSU, M. Medindo o índice de refração de líquidos usando o conceito de difração da luz. **Física na Escola**, v. 8, n. 1, p. 46–47, 2007. 56

SMYTH, H.; HICKEY, A. Multimodal particle size distributions emitted from hfa-134a solution pressurized metered-dose inhalers. **AAPS PharmSciTech**, v. 4, n. 3, p. 1–11, 2003. 74

SQUIRE, H. Investigation of the instability of a moving liquid film. **British Journal of Applied Physics**, v. 4, n. 6, p. 167–169, 1953. 31

STAMHUIS, E.; THIELICKE, W. Pivlab – towards user-friendly, affordable and accurate digital particle image velocimetry in matlab. **Journal of Open Research Software**, v. 2, n. 1, 10 2014. 25, 58

SUTTON, G. P.; BIBLARZ, O. **Rocket propulsion elements**. New Jersey: Wiley, 2017. Pp. 04-06. 1

TANASAWA, Y.; SASAKI, S.; NAGAI, N. The atomization of liquid by means of flat impingement. **The Technology Reports of the Tohoku University**, v. 22, n. 1, p. 73, 1957. 69

TODICA, M.; CORNEL, P.; UDRESCU, L.; POP, M. Rheological behavior of some aqueous gels of carbopol with pharmaceutical applications. **Chinese Physics Letters**, v. 27, 01 2010. 40

UBAID, M.; ILYAS, S.; MIR, S.; KHAN, A.; RASHID, R.; KHAN, M.; KANWAL, Z.; NAWAZ, A.; SHAH, A.; MURTAZA, G. Formulation and in vitro evaluation of carbopol 934-based modified clotrimazole gel for topical application. **Anais da Academia Brasileira de Ciência**, v. 88, p. 2303 – 2317, 2016. 43

VASQUEZ, R. **Desenvolvimento de um injetor centrífugo dual para biocombustíveis líquidos**. 219 p. Dissertação (Mestrado em Engenharia e Tecnologias Espaciais) — Instituto Nacional de Pesquisas Espaciais, São José dos Campos, 2011. 21

WEI, Q.; G., L. Coupled lagrangian impingement spray model for doublet impinging injectors under liquid rocket engine operating conditions. **Chinese Journal of Aeronautics**, v. 30, n. 4, p. 1391 – 1406, 2017. ISSN 1000-9361.

Disponível em: <[http:](http://www.sciencedirect.com/science/article/pii/S1000936117301504)

[//www.sciencedirect.com/science/article/pii/S1000936117301504](http://www.sciencedirect.com/science/article/pii/S1000936117301504)>. 26

WU, S. **Polymer interface and adhesion**. New York: Marcel Dekker, 1982. 48

YANG, L.; FU, Q.; ZHANG, W.; DU, M.; TONG, M. Spray characteristics of gelled propellants in novel impinging jet injector. **Journal of Propulsion and Power**, v. 29, p. 104–114, 2013. 18

ZHAO, F.; YANG, L.-j.; MO, C.-j.; QIN, L.-z. Spray characteristics of unlike impinging jets. **Journal of Propulsion and Power**, v. 33, n. 5, p. 1260–1271, 2017. 27